Università
degli Studi
di Pavia

Dipartimento
di Fisica
"A. Volta"

DOTTORATO DI RICERCA IN FISICA – XXIII CICLO

Low-energy excitations in rare-earth Single Molecule Magnets

dissertation submitted by

Francesca Branzoli

to obtain the degree of

DOTTORE DI RICERCA IN FISICA

Supervisor: Prof. P. Carretta

Referee: Prof. A. Keren

Cover: Pictorial sketch of the Pc_2Tb molecular magnet with the diamagnetic matrix arrangements of tetrabutylammonium surrounding the molecule and the corresponding crystal field levels structure.

Low-energy excitations in rare-earth Single Molecule Magnets
Francesca Branzoli
PhD thesis – University of Pavia
Printed in Pavia, Italy, November 2010
ISBN 978-88-95767-37-6

Ai miei genitori

Contents

Chapter 1

Introduction

1.1 Single Molecule Magnets: an Overview

Single Molecule Magnets (SMMs) have been fascinating chemists and physicists over the last two decades, thanks to the extremely rich variety of phenomena that such materials exhibit, providing inspiration for their potential application in materials science [1]. The contemporary evolution of the two novel disciplines of *spintronics* and *molecular electronics* paves the way for a new electronics, which allows for the simultaneously exploitation of electronic and spin degrees of freedom [2] and brings the trend towards ever-smaller electronic devices to its ultimate molecular-scale limit [3]. By far, the most important class of magnetic compounds for practical applications belongs to the group of ferromagnets [4][5]. In these materials the unpaired spins spontaneously align parallel to each other in macroscopic domains and permanent net-magnetization can be obtained under appropriate conditions. About two decades ago, the discovery that some polynuclear metallo-organic complexes possessing high-spin multiplicity (S_T) combined with large zero-field splitting can behave as classical superparamagnets promoted formidable research synergy among materials chemists and physicists [6]. In these systems the size of the magnetic domains is scaled down to the single-molecule level and provides ground to correlate phenomena that span from the nanoscopic to the microscopic world. Molecules exhibiting superparamagnetic properties show, in addition, staircase-like magnetization hysteretic loops, where the step substructure arises from the presence of quantum-tunneling paths in the magnetization between levels on the double-well potential which characterizes the ground state. [7][8][9]. Combination of these fingerprints together with the presence of phenomena such as quantum phase interference [10] has been used to classify these systems as single-molecule magnets [11]. The research efforts in the field are directed towards a better understanding of the quantum nature of SMM compounds which should trigger their synthetic design [12]. Several metallo-organic complexes behaving like SMMs have been discovered

in recent years and include, for example, the well-known family of Mn_{12} cluster complexes and derivatives [13][14][15][16], polynuclear iron complexes [17] and distorted cubane synthons [18][19][20]. In SMMs the slow relaxation of magnetization arises from the uniaxial anisotropy (D) of the molecule, which brings at low temperature the direction of the molecular magnetization vector **M** to be fixed and leads to suppression of spin reversal. In this scenario, the relaxation time (τ) of **M** obeys the thermally activated Arrhenius law, which is expressed as [8][21]

$$\tau(T) = \tau_0 exp(\Delta/k_B T) \quad , \tag{1.1}$$

where Δ is the energy barrier for the magnetization reversal.
Since the properties of SMMs are defined mainly by the intrinsic nature of the individual molecule parameters S_T and D [22][23], the resulting large, bistable spin anisotropy can deliver, in principle, the smallest practical unit for assembling molecular spintronic elements [24] such as dynamic random access memory devices and to the achievement of quantum computing [25][26]. However, limits on practical application can be easily foreseen, since their operational working temperatures are dictated by the so-called blocking temperature T_b of the SMM molecule. The blocking temperature is defined as the temperature below which the relaxation of the magnetization becomes slow compared to the time scale of a particular investigation technique [27]. The preparation of SMM metal complexes represents yet a synthetic challenge [28]; the arrangement of the Jahn-Teller axes of metal ions by bridging ligands must be engineered in a fashion that brings both high-spin ground-state and large zero-field splitting. To date, the record magnetization reported in multimetal clusters SMMs belongs to manganese compound $[Mn_6^{III}O_2(Etsao)_6\{O_2CPh(Me)_2\}(EtOH)_6]$, where $Etsao^{2-}$ derives from $Etsao H_2$ which indicates 2-hydroxyphenylpropanone oxime and $(Me)_2PhCO_2^-$ stands for 3,5-dimethylbenzoate [29]. The complex showed high-spin ground state, $S = 12$, quite large axial anisotropy, $D = -0.43$ cm^{-1}, thermal barrier Δ for spin reversal of 86.4 K, $\tau_0 = 2 \cdot 10^{-10} s$ and blocking temperature T_b of around 4.3 K. These properties slightly improved those found earlier in the $[Mn_{12}O_{12}(O_2CR)_{16}(H_2O)_4]$ (R = various groups) family, with S = 10 ground state, $T_b \simeq 3.5K$ and $\Delta \leq 74K$ [30].

1.2 Rare-Earth Single Ion Molecular Magnets

Recently, a different class of SMMs emerged [31], where slow relaxation of the magnetic moment arises from a single *f*-metal ion coordinated by the isoindoline nitrogens of two phthalocyaninato (Pc) rings. These compounds are formulated in literature as Pc_2M [32] [33]. Although the syntesis of Pc_2M synthons is dated from the 1960s [34] and those studies were complemented years later by the investigation of the magnetic properties [35][36][37], the discovery of slow magnetization relaxation, hysteretic behaviour and also resonant

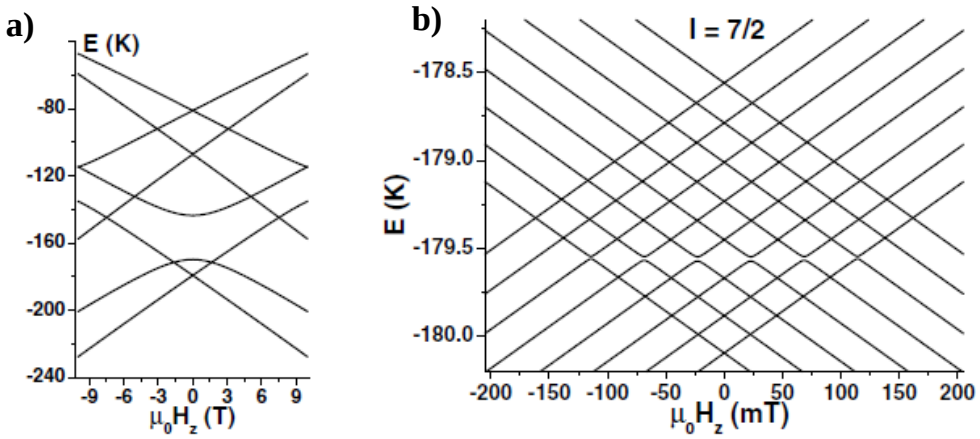

Figure 1.1: a) Low-energy part of the Zeeman diagram. The first excited state ($\approx$ 25 K below the next excited singlet) defines an energy barrier of $\approx$9.5 K hindering the magnetic moment reversal [38]. b) Splitting of the electronic ground state doublet by the hyperfine interaction A_J. The level crossings occur for resonant values of the longitudinal field H_n ($-7 \leq n \leq 7$). Some are avoided level crossings. Hyperfine levels repulsion is induced by the electronic level repulsion in the excited states shown in (a).

quantum tunneling between hyperfine levels were discussed in literature just a few years ago through experimental and theoretical analyses of the magnetic behaviour of $LiY_{1-x}Ho_xF_4$, a prototype of a diluted single-ion magnet [38][39], which has proven to be very important in the studies of magnetism. The magnetic properties of this system significantly change by increasing the dilution of holmium ion with non-magnetic yttrium. $LiY_{1-x}Ho_xF_4$ is essentially isostructural over the entire range of x, allowing for a systematic study of dilution of magnetic moments and of the evolution from correlated ferromagnet towards single-ion behaviour. In fact, pure $LiHoF_4$ (x=1) exhibits dipolar coupling between the magnetic Ho^{3+} ions and becomes ferromagnet below a Curie temperature of $T_C = 1.5$ K [40][41]. Dilution of Ho with Y lowers T_C and for $0.1 < x < 0.5$ the low temperature ground state is a spin glass [41]. On the other hand, for somewhat lower concentrations ($x \approx 0.05$) the ground state appears to be an unusual quantum "antiglass" [42][43]. For very dilute Ho concentrations ($x \approx 0.002$) and at low temperatures, a single Ho^{3+} ion behaves as a single ion magnet with a frozen magnetic moment, due to the large axial crystal field anisotropy along the tetragonal c axis, which is the quantization z axis. The energy barrier for reorientation is $E_b \approx 10$ K and separates a Ising-like doublet from the singlet first excited state [44]. The quantum dynamics of single ion rare-earth magnets is made particularly interesting by the coupling of the electronic moment with the nuclear moment. The hyperfine coupling to the Ho nuclear spin (I =7/2) further splits the ground state Ising doublet into eight twofold degenerate levels equally spaced (Fig. 1.1). Application of

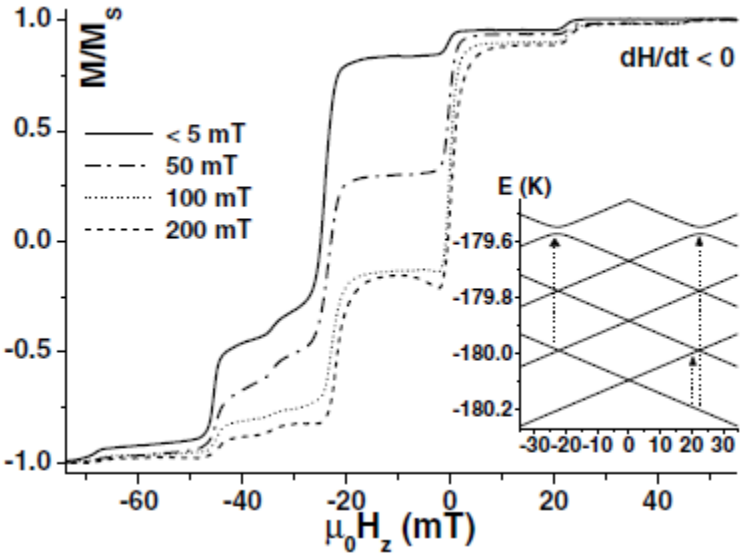

Figure 1.2: Hysteresis loops in a constant transverse field at T = 50 mK and for the rate v = 0.55 mT/s. A transverse field enhances the quantum fluctuations in zero longitudinal applied field leading to a larger magnetization step. Inset: details of the Zeeman diagram around zero field. Thermally activated tunneling shows two possible channels over the first and the third, more efficient, excited avoided level crossings.

a small magnetic field along the crystalline c axis introduces Zeeman splitting of these degenerate levels. Calculations predict that level (and anti-level) crossings occur at longitudinal fields given by $H_n = nA_J/2g_J\mu_B \approx n23$ mT, where A_J is the hyperfine constant and n is an integer with $-7 < n < 7$. This was confirmed by the observation of quantum tunneling of the magnetization (QTM), as evidenced by steps in the magnetization at the resonant field values [38] (Fig. 1.2), in analogy with the phenomenon observed in high-spin molecular magnets Mn_{12} [7] and Fe_8 [17].

Not long after, Ishikawa and coworkers first, followed later on by joint works with Wernsdorfer, demonstrated that the anionic complexes $[Pc_2\text{Tb}]^-[\text{TBA}]^+$ (TBA = tetrabutylammonium), $[Pc_2\text{Dy}]^-[\text{TBA}]^+$ and $[Pc_2\text{Ho}]^-[\text{TBA}]^+$ possess signatures of single-ion molecular magnets (SIMM) [31][32][45][46]. In these systems, the relaxation processes of the lanthanide ions arise from the energy exchange between the f-metals, with a total angular moment J, and phonon-assisted radiation. The effective energy barrier Δ for the magnetic moment reversal is in fact determined by the crystal field potential (CF) around the f-metal, which partially relieves the degeneracy in J_z for the ground state. Especially, in Tb- and Dy-based compounds the anisotropy barrier reaches several hundreds of kelvin ($\Delta \simeq 620K$ and $\Delta > 260K$ [47]), thus yielding unprecedent large correlation times τ_c at cryogenic temperatures. Moreover, it is to notice that the magnetic properties of these lanthanide complexes are

strongly influenced by the chemical and structural modification of the ligands through which the CF potential can be varied [48]. In fact, the CF configuration can be modified from the very diluted limit in $[Pc_2\mathrm{Ln}]^-[\mathrm{TBA}]^+n[\mathrm{TBA}]\mathrm{Br}$, with $n+1 >> 1$ the number of tetrabutylammonia units, to the concentrated limit consisting solely of neutral double-decker molecules in $[Pc_2\mathrm{Ln}]^0$. It has been recently shown that one or two-electron oxidation of $[Pc_2\mathrm{Ln}]^-$ yields a compression of the cage around Ln^{3+} ion and an increase of the CF splitting [49][50][51]. Understanding how small differences in molecular surrounding can trigger substantial modifications of the SIMM properties is of utmost importance for ongoing research on surface-deposited bis-phthalocianinato lanthanide (III) molecules, targeting the realization of single molecular data storage [52][53][54].

1.3 Future Applications of SMMs

1.3.1 Molecular Spintronics

Rare-earth-based double-decker molecules seem to be very promising candidates to be used in the field of molecular spintronics, thanks to the extremely large axial anisotropy and tunable magnetic features. In the following, a few examples of innovative devices which exploit SMMs magnetic properties will be presented. There are three basic configurations allowing for the exploitation of molecules in the field of molecular spintronics [24]. The first scheme consists of a magnetic molecule attached between two non-magnetic electrodes. A scanning tunneling microscope (STM) tip can be used as the first electrode and a conductive substrate as the second one. Theoretical works predicted that quantum tunneling of the magnetization is detectable via the electric current flowing through the molecule [55], thus enabling the readout of the quantum dynamics of a single molecule. Nevertheless, the rather drastic experimental requirements for studying SMMs by STM, e.g. very low temperature and high fields, have not yet been achieved so far and only few atoms on surfaces have been probed in this way [56]. Alternatively, in the so called *molecular spin-transistor* [57], the current passes through the magnetic molecule placed between non-magnetic source and drain electrodes, and the electronic transport properties are tuned using a gate voltage V_g. Theoretical investigations predict the connection of structural and magnetic parameters to the transport features, suggesting a rational design of SMMs for spintronics.

The second scheme consist of a *spin-valve* [58], which is similar to a spin transistor but contains at least two magnetic elements. Here, the electrical resistance depends on the mutual alignments of the magnetizations of the electrodes and of the molecule. One of the few example of molecular SVs consists of a diamagnetic molecule, such as a C_{60} fullerene or a carbon nanotube, in between two magnetic leads, which can be metallic or semiconducting, transforming spin information into large electrical signals [59][60]. When using

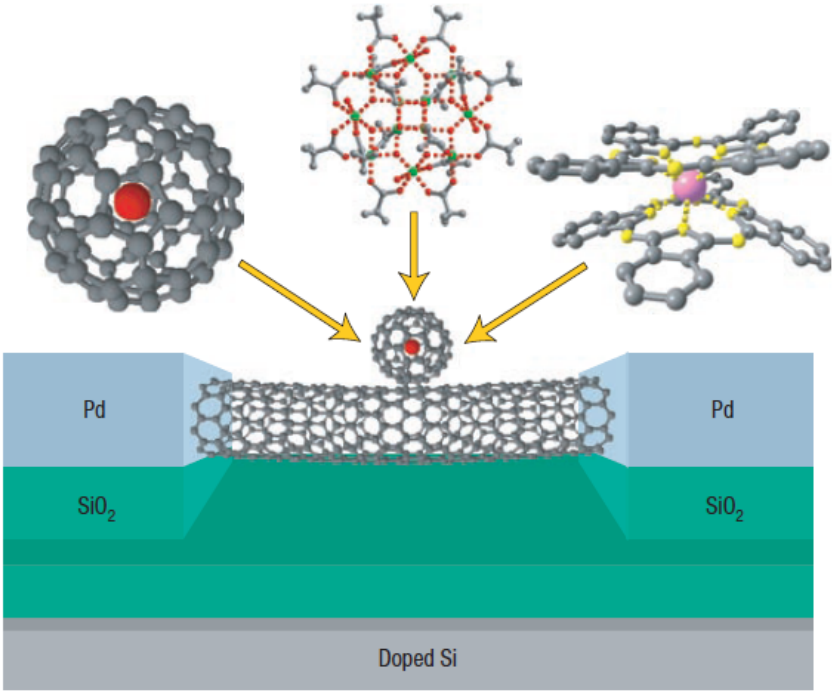

Figure 1.3: Magnetic molecules proposed for grafting on suspended carbon nanotubes connected to Pd electrodes (form left to right): a C_{60} fullerene including a rare-earth atom, the $[Mn_{12}O_{12}(C(CH_3)_3COO)_{16}(H_2O)_4]$ SMM and the rare-earth-based double-decker [Tb(phtalocyanine)$_2$] SMM. The gate voltage of the double-dot device is obtained by a doped Si substrate covered by a SiO_2 insulating layer. Figure taken from Ref. [24].

SMMs only spins parallel to the molecular magnetization should flow through the molecule and the current should display a very high spin polarization for a time equivalent to the relaxation time. This phenomena, called *giant spin amplification* [61], offers a convenient way to read the magnetic state of the molecule.

The third configuration consists of a double-dot with three terminals, where the SMM acts as a magnetic quantum-dot (QD) and the current passes through a non-magnetic quantum conductor. The magnetic molecule is only weakly coupled to the non-magnetic conductor, but its spin can influence the transport properties, allowing readout of the spin state with minimal perturbation of the molecule itself. Very recently, Pc_2Tb-based complexes were successfully attached to single-walled carbon nanotubes connected to metallic electrodes [62].

1.3.2 Hybrid Molecular Conductors

SMMs look very attractive also for the design of hybrid molecular conductors, combining in a single compound organic cationic radicals, able to give rise to

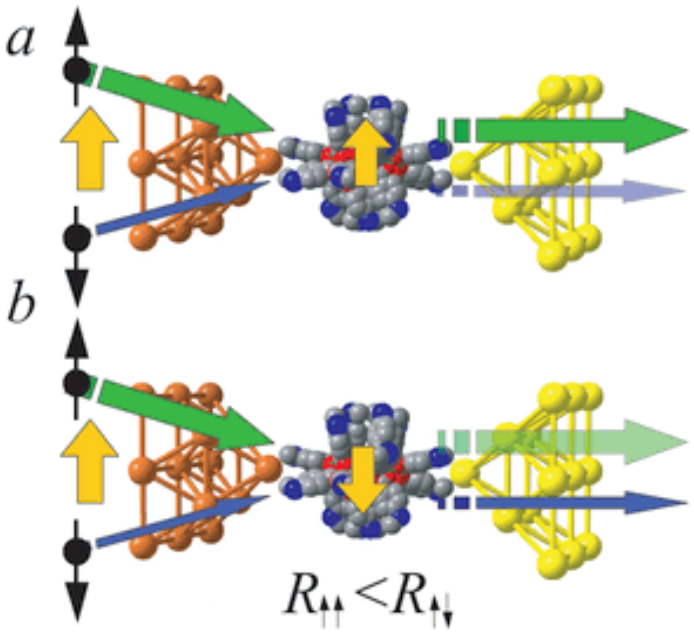

Figure 1.4: Spin valves based on molecular magnets. (a) Parallel configuration of the magnetic source electrode (orange) and molecular magnetizations (yellow arrows), with a diamagnetic drain electrode (yellow). Spin-up majority carriers (thick green arrow) are not affected by the molecular magnetization, whereas the spin-down minority carriers (thin blue arrow) are partially reflected back. (b) Antiparallel configuration: majority spin-up electrons are only partially transmitted by the differently polarized molecule, whereas the minority spin-down electrons pass unaffected. Assuming that the spin-up contribution to the current is larger in the magnetic contact, this configuration has higher resistance than that of the previous case. Figure taken from Ref. [24].

conducting architectures, with functional molecular anions bringing a second physical property of interest [63]. During the 1980s organic radicals, such as the electron donor tetrathiafulvalene (TTF) and its derivatives, were used to prepare conducting radical salts with different stable counter-ions only playing a charge compensating and structural role [64]. The two network hybrid structure of these salts suggested the possibility of designing dual-function materials using as counter-ions functional anions. Coupling between properties is of course desired in many cases as it may bring about synergetic effects between them; on the other hand, the independence of the two properties due to the lack of electronic interaction between the two networks can be even very interesting since it may lead to combination of properties that are difficult or impossible to coexist in naturally occurring materials, like, for example, ferromagnetism and superconductivity. The molecular approach offers unparalleled opportunities in this area since it enables chemical design of the molecular building blocks in order to make them suitable for self-assembly to form supramolecular struc-

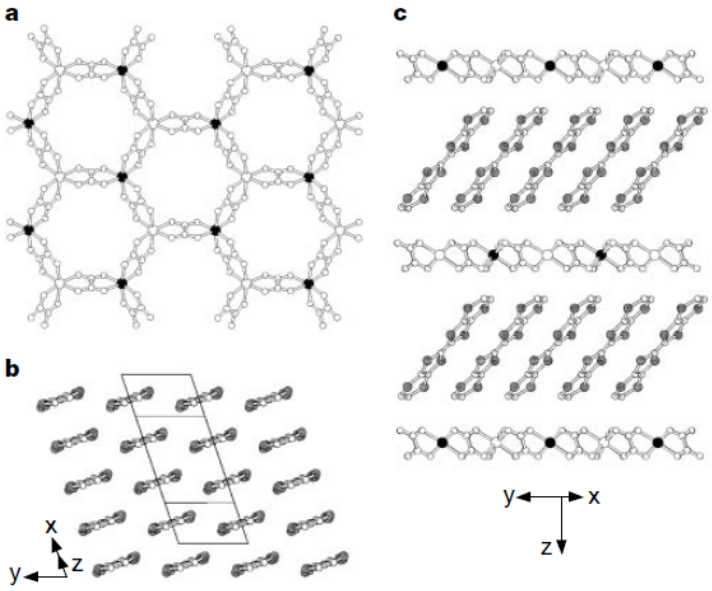

Figure 1.5: Example of hybrid material. (a) View of the $[M^{II}M^{III}(C_2O_4)_3]^-$ bimetallic layers. Filled and open circles in the vertices of the hexagons represent the two types of metals. (b) Structure of the organic layer, showing the β packing of the BEDT-TTF molecules. (c) Representation of the hybrid structure along the c axis, showing the alternating organic/inorganic layers.

tures with the desired interactions and properties. Most of the research has been focused in the search for materials combining conducting and magnetic properties. So far, the general strategy towards molecular magnetic conductors consisted of the preparation of radical salts of TTF derivatives using anionic paramagnetic complexes of transition metals as counter-ions, such as MX_4^{n-}. Thus, paramagnetic organic metals [65] and even superconductors have been obtained [66]. The most striking result has been the appearance of superconductivity induced by high external magnetic fields. While a high enough applied magnetic field usually destroys the superconducting state, in this case the reverse effect is observed due to the presence of localized magnetic moments in the material. A possible explanation to such behavior was attributed to the compensation between the magnetic field seen by the electronic spin of the superconductor and the exchange magnetic field due to the magnetic ions [67]. In order to achieve ferromagnetism at relatively high T_C, a solution consists of using a polymeric anionic network instead of discrete molecules. The presence of a ferromagnetic layer interlayed with conducting layers of TTF derivatives could give rise to novel magnetoresistance properties, since the ferromagnetic layer will create an internal magnetic field that can be quite strong, and that will obviously affect the conduction electrons. On the other hand, if in this approach the two networks are independent, this may lead to the preparation of a ferromagnetic superconductor, although superconductivity and ferroma-

gentism are thought to be mutually exclusive. Bimetallic oxalate-based layered complexes were used as the magnetic component. Crystals with alternating layers of the $[MnCr(ox)_3]^-$ anionic network and of ET were successfully obtained, which behave as ferromagnets below 5.5 K and are metallic down to at least 0.2 K [68]. Remarkably, the properties of $[M^{II}M^{III}(ox)_3]^-$ complexes can be changed at will from insulating to metallic and from paramagnetic to ferromagnetic, maintaining the overall structural features in such a way that the correlations between the two properties can be properly examined and determined. The hybrid approach to multifunctionality is not restricted to crystalline materials. Organized thin films and nano objects are also under investigation [69]. The possibility of exploiting magnetic properties of Ln-based compounds in such multifunctional materials is in view.

1.3.3 Contrast Agents for Magnetic Resonance Imaging

Finally, it is to remark that SMMs have been recognized as suitable materials which can be used as contrast agents for medical diagnostics [70]. In fact, these molecules comprise the chemical and magnetic structure of the gadolinium chelates with the superparamagnetism of the SPIOs (Superparamagnetic Iron Oxides), materials which represent some of the common magnetic resonance imaging (MRI) contrast agents in current use [71]. MRI contrast agents function by changing the nuclear resonant frequency, the longitudinal spin-lattice relaxation time T_1 and the transverse dephasing time T_2 of nearby aqueous hydrogen nuclei in biological systems. These changes allow to selectively enhance the contrast of structures of interest such as tumors, the vasculatory system and lesions. Gd^{3+}-based contrast agents shorten both the longitudinal and transverse relaxation times of water protons to approximately the same extent. This effect is detected as increased signal intensity in T_1-weighted MRI images when the appropriate pulse sequence is applied. A conceptually different approach to contrast enhancement is based on chemical exchange saturation transfer (CEST) [72]. This technique relies on dynamic chemical exchange processes inherent to biological tissues which allow to transfer saturated ^1H spins into the bulk water proton pool, which leads to a decrease of net magnetization and is detected as a negative contrast (darkening of the image) in MRI. The great benefit of using paramagnetic hyperfine shifting lanthanide complexes as CEST agents (PARACEST) is that the chemical shift difference between the two exchanging pools can potentially be much larger, up to several hundred ppm, facilitating easy saturation of one of the exchangeable spin pools without partial saturation of the bulk water pool. Moreover, since the water exchange rate on lanthanide complexes is extremely sensitive to the chemical environment, this has created unprecedented opportunities in the design of responsive PARACEST agents [73].

1.4 Thesis Outline and Motivation

The main scope of this work is the determination of the energy barrier, spin correlation time and spin-phonon coupling of several single molecule magnets based on different rare-earth ions. The characterization of these properties, indeed, is of major interest for aiming at the employment of rare-earth SMMs in new electronic devices exploiting bistable molecules or as novel contrast agents for medical diagnostics. Moreover, an experimental study of the magnetic properties of $[Pc_2\mathrm{Y}]^0$, which can be considered the parent compound of Pc_2Ln molecular magnets, is presented.
In the following Chapter, the general properties of Pc_2Ln rare-earth single molecule magnets are presented, starting from the chemical and structural characterization of the materials under investigation. An overview of the electronic and transport properties of Pc_2Ln-based systems is then illustrated, followed by a description of the ligand field levels structure of $[Pc_2\mathrm{Ln}]^-\mathrm{TBA}^+$ compounds. The theoretical background on the basis of the relaxation processes driving the transitions between rare-earth ion crystal field levels is elucidated and the Raman and specific heat experiments in $[Pc_2\mathrm{Tb}]^0$ and $[Pc_2\mathrm{Dy}]^0$ samples discussed.
In Chapter 3, the bulk magnetic properties derived by means of DC and AC magnetization measurements in diluted $[Pc_2\mathrm{Tb}]^-\mathrm{TBA}^+ \times n[\mathrm{TBA}]\mathrm{Br}$ and neutral $[Pc_2\mathrm{Ln}]^0$ (Ln = Tb, Dy or Y) compounds are presented, after a brief description of the SQUID magnetometer.
In Chapter 4, a description of the basic aspects of Nuclear Magnetic Resonance (NMR) and Muon Spin Rotation (μSR) techniques is reported.
Chapter 5 focuses on the analysis and discussion of NMR and μSR measurements, which have been performed on both diluted and neutral Pc_2Ln-based molecular magnets. In particular, the high temperature activated spin dynamics, involving phonon-assisted transitions among the crystal field levels, and the low-temperatures fluctuations driven by tunneling processes between the lowest-energy levels have been investigated.
In Chapter 6 the microscopic properties of $[Pc_2\mathrm{Y}]^0$ compound derived by means of NMR are discussed.
Finally, the main findings obtained during this Ph.D. work are resumed in Chapter 7.
Further information about samples chemical and structural details and about the instrumentation used to perform part of the measurements reported in this thesis can be find in the Appendix.

Chapter 2

General Properties of Rare-Earth Single Molecule Magnets

In this chapter, the fundamental properties of the $[Pc_2\text{Ln}]$-based complexes will be discussed. First, the chemical and structural characterization of the compounds containing terbium or dysprosium ions, that are the main object of this work, will be presented. Then, the general electronic and transport properties of rare-earth SMMs will be discussed, with reference to resistivity measurements in neutral $[Pc_2\text{Tb}]^0$. The ligand field levels structure of $[Pc_2\text{Ln}]^-\text{TBA}^+$ complexes, as derived by Ishikawa *et al.* in previous works, will also be presented. In addition, the magnetization relaxation mechanism involving spin-lattice interactions will be described. The intramolecular vibrational modes involved in the relaxation processes will be investigated through the Raman spectra measurements in the energy range of interest. Finally, specific heat (C_v) experiments on $[Pc_2\text{Tb}]^0$ compound confirm the prevalence of the lattice contribution to C_v against the magnetic one, as a consequence of the large number of atoms in the molecule.

2.1 Chemical and Structural Properties of Pc_2Ln-based Systems

The structure of $Pc_2\text{Ln}$ molecule consists of a positive rare-earth ion, possessing a total angular moment $\mathbf{J}=\mathbf{L}+\mathbf{S}$, and two phthalocianine ($Pc = \text{C}_{32}\text{H}_{16}\text{N}_8$) ligands forming a double-decker structure (Fig. 2.1). Each lanthanide ion is 8-fold coordinated by the pyrrole nitrogen atoms of the two Pc ligands [74][75]. As regards $Pc_2\text{Tb}$ molecule, calculations based on Density Functional Theory (DFT) show that 2.6 electrons are transferred from the terbium metal center to the Pc ligands (1 and 1.6 from the f and s channels, respectively) so

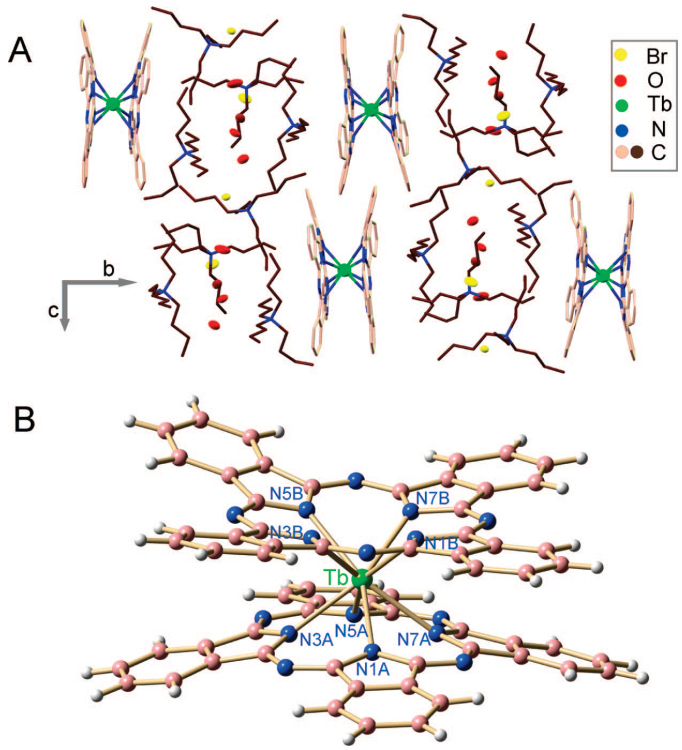

Figure 2.1: (A) Packing sketch of $[Pc_2\mathrm{Tb}]^-[\mathrm{TBA}]^+ \times 3$ [TBA]Br $\times$ 3 H_2O (**4**), showing the allocation of the $[Pc_2\mathrm{Tb}]^-$ complex anions in the unit cell. (B) Molecular structure of the $[Pc_2\mathrm{Tb}]^-$ complex anion in 4 showing the Tb^{3+} metal ion (green) coordinated by the phthalocyaninato ligands (carbons: pink; hydrogen: gray; nitrogens: blue). Relevant Tb-N (intramolecular) distances: Tb(1)-N(1A), 2.548(6) Å; Tb(1)-N(3A), 2.340(5) Å; Tb(1)-N(5A), 2.509(6) Å; Tb(1)-N(7A), 2.357(5) Å; Tb(1)-N(1B), 2.535(6) Å; Tb(1)-N(3B), 2.313(5) Å; Tb(1)-N(5B), 2.573(6) Å; Tb(1)-N(7B), 2.338(6) Å (see Appendix for further structural details).

that, with respect to the Tb atomic $6s^2 4f^9$ valence configuration, the metal center is predicted to have an ionic charge of 2.6+ [52]. Thus, as far as the magnetic properties are concerned, the Pc-complexed Tb ion is a very good approximation for an isolated Tb^{3+} ion having a total angular moment J = 6. Similar consideration can be done for isostructural compounds containing different lanthanide ions. The charge transferred from the Ln ion to the ligands is not sufficient to saturate them, since each Pc plane requires two electrons to be saturated. As a consequence, the molecule can exist in different forms depending on the oxidation state of the phthalocianine rings [35][37][76]. In the anionic form $[Pc_2\mathrm{Ln}]^-$ the organic core of the molecule adopts a closed shell π-electronic configuration and each Pc ring bears a formal charge of -2. The resulting negative charge located on the molecule needs to be stabilized by a counterion, such as the commonly used n-tetrabutylammonium $[\mathrm{TBA}]^+$

empirical formula	$C_{128}H_{182}Br_3N_{20}O_3Tb$
formula weight	2447.59
temperature	120(2) K
wavelength	0.34250 Å
crystal system, space group	monoclinic, $P2_1/c$
unit cell dimensions	a = 13.807(2) Å b = 37.015(5) Å c = 25.127(5) Å $\alpha = 90°$; $\beta = 100.764(9)°$; $\gamma = 90°$
volume	12616(3) Å^3
Z, calculated density	4, 1.289 Mg/m^3
absorption coefficient	0.846 mm^{-1}
$F(000)$	5136
crystal size, color	0.12 mm × 0.11 mm × 0.07 mm, blue
θ range for data collection	$1.01° \leq \theta \leq 10.97°$
limiting indices	$-15 \leq h \leq 15$, $-41 \leq k \leq 41$ $-27 \leq l \leq 27$
reflections collected/unique	64949/17144 [R(int) = 0.1127]
completeness to θ	94.6%
refinement method	full-matrix least-squares on F^2
data/restraints/parameters	17144/9/1415
reflections with I > 2σ(I)	11177
Extinction coefficient	0.0048(5)
largest diff. peak and hole	1.621 and −1.031 e·A^{-3}
goodness-of-fit on F^2	1.030
final R indices [$I > 2\sigma(I)$]	R1 = 0.0679, wR2 = 0.1569
R indices (all data)	R1 = 0.1136, wR2 = 0.1753

Table 2.1: X-ray data for $[Pc_2\text{Tb}]^-[\text{TBA}]^+ \times$ 3 $[\text{TBA}]^+Br^- \times$ 3 H_2O (**4**), experimental details, structure solutions and refinements.

molecule. The X-ray study for $[Pc_2\text{Ln}]^-\text{TBA}^+$ (Ln = Lu, Ho and Gd) has shown that in the complex with the smallest ion with f^{14} configuration, Lu^{3+}, the skew angle the two ligand make is 45.0° and the ligand field is approximately of D_{4d} symmetry [77]. The angle gradually becomes smaller with a decrease of the atomic number of the lanthanide ion. The distance between the two ligands regularly decreases as the lanthanide atomic number increases and is correlated with the change of ionic radii due to the lanthanide contraction. On the other hand, the neutral species $[Pc_2\text{Ln}]^0$ corresponds to one electron oxidation form which occurs on the ligand side of the complex. In this case, the organic core features the open shell π-electronic configuration, thus beside the f electrons strongly localized on the magnetic ion, the one-half spin system associated to the π unpaired electron delocalized over the two Pc rings is present.

2.1.1 Synthesis of $[Pc_2\text{Tb}]^-[\text{TBA}]^+n[\text{TBA}]\text{Br}$

The synthesis of $[Pc_2\text{Tb}]^-[\text{TBA}]^+$ (**1**) was carried out by employing several modifications of the general protocol based on the procedure published by Weiss and coauthors [35]. The synthesis of Pc_2M synthons relies mostly on templating reactions, starting from the phthalonitrile precursor, in the pres-

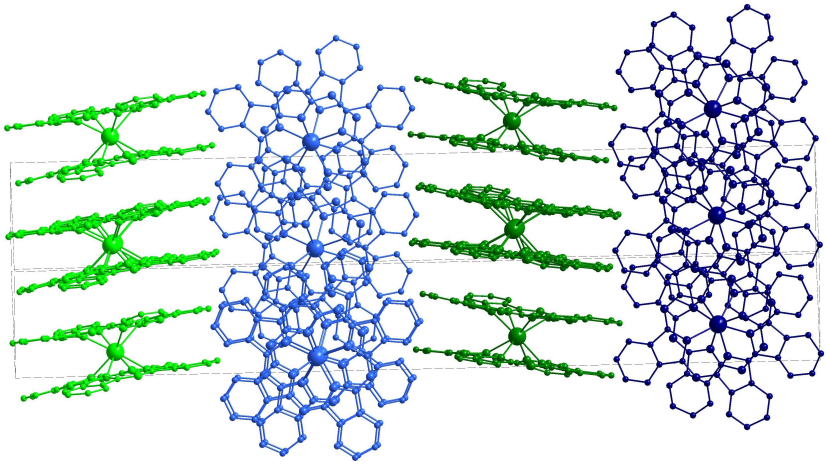

Figure 2.2: Packing sketch of $[Pc_2\mathrm{Tb}]^0$, showing the four independent orientations of $[Pc_2\mathrm{Tb}]^0$ molecules in the unit cell. Orthorhombic: P 2_1 2_1 2_1 (no. 19), a = 8.8377(5) Å, b = 10.5652(9) Å, c = 50.7480(29) Å.

ence of a strong base (e.g., DBU, alkoxides) and high-boiling solvents, such as pentanol or hexanol. The molecular assembly of $[Pc_2\mathrm{Tb}]^-[\mathrm{TBA}]^+$ was carried out by employing microwave energy, as an alternative to conventional heating. In this way, side reactions and especially formation of large amounts of empty phthalocyanine rings was avoided. Both forms, the anionic, $[Pc_2\mathrm{Tb}]^-$, and neutral, $[Pc_2\mathrm{Tb}]^0$, were obtained simultaneously (see Appendix for details), but their relative ratio, which strongly depends on heating gradients, allowed mostly formation of the negative form $[Pc_2\mathrm{Tb}]^-$ because of the fast thermal gradients induced through microwave heating. Purification of the negatively charged complex was very demanding, and is reported in detail in Appendix. The stabilization of the anionic form $[Pc_2\mathrm{Tb}]^-$ was obtained by stoichiometric addition of n-tetrabutylamonium bromide salt [TBA]Br while excess of salt has been used for the diamagnetically diluted preparations, $[Pc_2\mathrm{Tb}]^-[\mathrm{TBA}]^+$ × 143 [TBA]Br (**3**) and $[Pc_2\mathrm{Tb}]^-[\mathrm{TBA}]^+$ × 9 [TBA]Br (**2**). Starting from the diluted $[Pc_2\mathrm{Tb}]^-[\mathrm{TBA}]^+$ × 9 [TBA]Br sample, the molecular complex $[Pc_2\mathrm{Tb}]^-[\mathrm{TBA}]^+$ × 3 [TBA]Br × 3 H_2O (**4**) crystallized in MeOH, forming blue-violet needles, within few days. Collection of the structural parameters and solution refinements for **4** are given together in Table (2.1).

2.1.2 Synthesis of $[Pc_2\mathbf{Tb}]^0$, $[Pc_2\mathbf{Dy}]^0$ and $[Pc_2\mathbf{Y}]^0$

The synthesis of both samples was carried out by using several modifications of the protocol based on the published procedure reported in Ref. [74][77][78]. The anionic form $[Pc_2\mathrm{Ln}]^-$ (Ln = Tb, Dy or Y) was obtained through the procedure described in the previous Par. 2.1.1. In order to convert the unstabilized anionic form to the neutral one, the reaction mixture was presorbed on

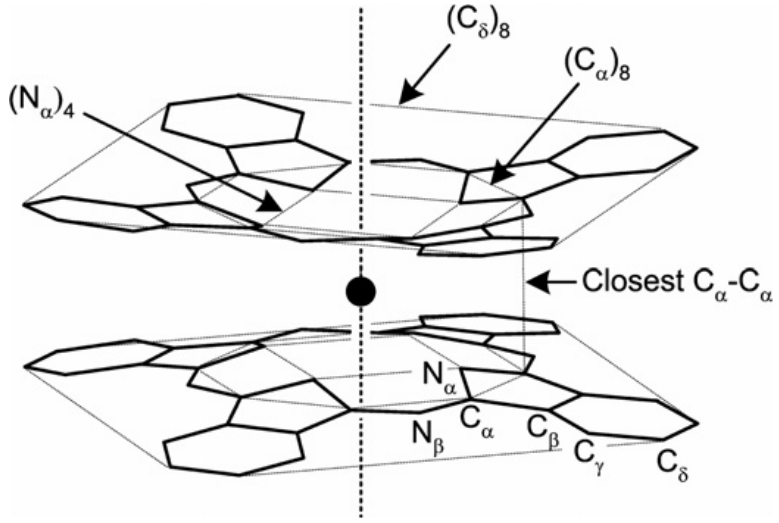

Figure 2.3: Schematic rapresentation of Pc_2Ln molecule: planes made by four inner nitrogen atoms, $(N_\alpha)_4$, eight inner carbon atoms, $(C_\alpha)_8$, and eight most-outer carbon atoms, $(C_\delta)_8$.

active (H_2O-0 %) basic alumina oxide. Purification was carried out by column chromatography on basic alumina oxide (deactivated with 4.6 % H_2O, level IV) with chlorophorm-methanol mixture (10:1) as eluent. In general, the yield was 30-35 %. By means of additional radial chromatography on silica gel followed by recrystallization from chloroform-hexane mixture, analytically pure powder samples were achieved (see Fig. 2.2). Deep green crystals of the products were obtained by using slow diffusion of CH_2Cl_2 into $C_2H_2Cl_4$ solution of the pristine $[Pc_2Ln]^0$. After 2 weeks, deep green needlelike crystals were obtained. The $[Pc_2Ln]^0$ molecules crystallized in the space group $P2_12_12_1$ (γ - phase) and were isomorphous to each other [79].

2.2 Electronic Structure of Pc_2Ln

It has been shown by a semi-empirical quantum chemical study that the π-electronic system of the double-decker complex is composed of the linear combination of the two Pc ligand π orbitals [80]. The lowest unoccupied molecular orbital (LUMO) of Pc molecule is of e_g symmetry and is essentially a π^* orbital with a probability density predominantly distributed about the centre of the ring. The highest occupied molecular orbital (HOMO) is a π non-bonding orbital centered on the carbons closest to the centre of the ring (C_α). This orbital belongs to the a_{1u} representation. The second highest occupied molecular orbital (next-HOMO) is of the b_{2g} type and is primarily localized on the pyrrole nitrogens as a linear combination of four lone pair type orbitals. The HOMO and next-HOMO (a_2 and b_1 symmetry respectively) of anionic form $[Pc_2Ln]^-$,

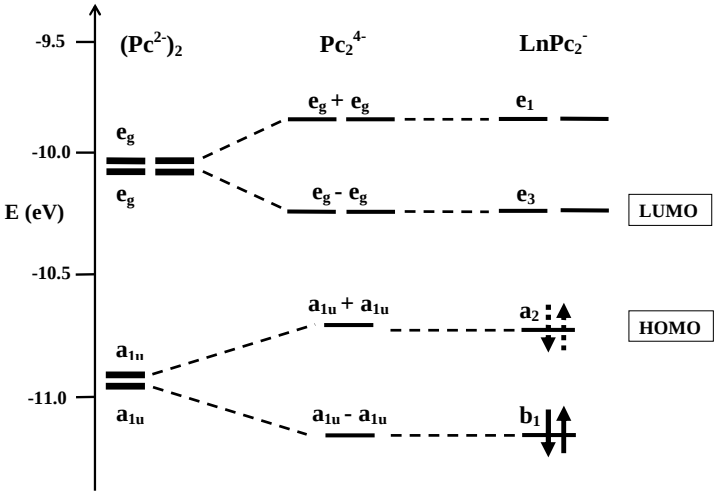

Figure 2.4: Schematic rapresentation of HOMO, next-HOMO, LUMO and next-LUMO of Pc_2Ln constructed from two isolated Pc ligands. When the complex is oxidized, the electrons in the anti-bonding HOMO are removed first.

which is the most stable oxidation state, are described as anti-bonding and bonding linear combination of the HOMOs of the Pc ligands (see Fig. 2.4). The metal ion plays a relatively small role in stabilizing the frontier orbitals of the two Pc rings and the metal-ring interaction may be understood in terms of second-order intermolecular perturbations [81]. The major component in the splitting of the energy levels is due to the ring-ring interaction, that can be approximated by the mixing of orbitals of the same energy on adjacent rings, since an inspection of the eigenvectors of the Hamiltonian matrix reveals that there is very little mixing between the orbitals on the same ring. In this analysis, the first-order perturbation theory for degenerate intermolecular states provides the relationship

$$\Delta E_i = (\beta_{ii'} - E_i^0 S_{ii'}) \propto S_{ii'} \quad , \tag{2.1}$$

where $S_{ii'}$, is the overlap between the i-th molecular orbital of fragment 1 and the corresponding orbital of fragment 2, and $\beta_{ii'}$ is the interaction energy of the perturbation. In summary, the ring-ring splitting interactions are dependent upon the overlap between Pc molecular orbitals.

When the complex is oxidized, the electrons in the anti-bonding HOMO are removed first. In the cationic complex $[Pc_2\text{Ln}]^+$, two electrons are removed from the a_2 orbital, which is now LUMO, and the b_1 orbital becomes HOMO accordingly. Since the strength of the bonds between the C_α atoms in facing Pc ligands has a crucial role for determining the inter-planar distance, it is expected that the removal of the electrons in the anti-bonding HOMO causes shorter Pc-Pc distance which has the effect to strengthen the ligand-

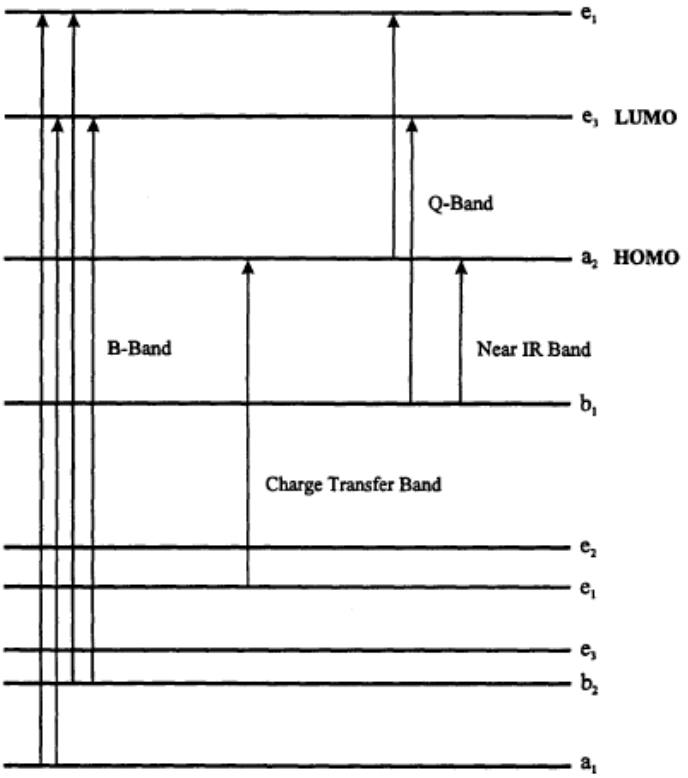

Figure 2.5: Diagram of electronic transitions in $[Pc_2\text{Ln}]^n$.

field potential under which the lanthanide ion is placed [81]. In fact, the closest inter-planar C_α-C_α distance is predicted to be shortened upon oxidation by ca. 0.10 Å, which is a significant amount. Accordingly, the $(N_\alpha)_4$-$(N_\alpha)_4$ distance, which directly affects the LF potential to the lanthanide ion, is shortened by 0.08 Å [82].
Optical absorption transitions were assigned by the use of dipole transition selection rules for the D_{4d} point group (see Fig. 2.5) [83][81]. The Q band (650-750 nm) is essentially associated with electron density moving from the a_2 and b_1 orbitals that are strongly centered on C_α to the lowest unoccupied e_3 and e_1 orbitals, centered on pyrrole (N_α) and isoindole nitrogens (N_β). The component of this band associated with the a_2 orbital diminishes as the oxidation state of the Pc_2Ln species increases from -1 to +1. The presence of a band at about 450 nm for the radical and cationic species (CTI band) is found to correlate to electrons in the highest occupied e_1 orbital being excited into the hole(s) in the a_2 orbital. Another band which appears for these two species over the 1220-900 nm range is due to the transitions from the highest occupied b_1 orbital to the a_2 orbital. Finally, he multiplet of bands in the 400-300 nm range, the B band, is found to correspond to transitions associated with the highest occupied b_2 and a_1 (π) orbitals to the two lowest unoccupied orbitals.

2.3 Transport Properties of Pc_2Ln

Inorganic materials with conductivities intermediate between those of metals and those of insulators form a homogeneous class of materials possessing a low density of intrinsic charge carriers associated with high mobilities and a temperature activated conductivity. These materials may be p- or n-doped and may be used to form junctions and associated electronics devices such as photoconductors or field effect and bipolar transistors [84]. On the contrary, members of the organic molecular family showing intermediate conductivities reveal very disparate properties. As already mentioned, molecular materials are constituted of molecular units that can be individually characterized by their properties, such as chemical nature, shape, redox potentials and polarity. The molecular units are organized in a second step to give a condensed phase (amorphous or polycrystalline films, liquid crystals, single crystals) [85]. A molecular semiconductor can be defined as a material characterized by an intrinsic conductivity in the semiconducting range, that can be doped with electron acceptors and electron donors to yield highly conducting materials. Within these hypothesis, neither mesomolecular systems (from naphthalene to pentacene), nor macromolecular systems (polyacetylene, polydiacetylene etc.) belong to the molecular semiconductor class [84]. In fact, in many cases intermediate conductivities have been obtained but always as a result of doping. They are consequently insulators when undoped, due to the large energy difference between the HOMO and LUMO orbitals which prevents creating free charge carriers. Phthalocyanine radicals are exceptions to that rule, since they show intrinsec semiconducting properties [86]. This difference is important since devices usually associated with semiconductors such as diodes or transistors cannot be realized using doped insulators [87]. Especially, bis(phthalocyaninato) lanthanide (Pc_2Ln) and lithium phthalocyanine (PcLi) are easily reduced and oxidized and the HOMO-LUMO difference is correspondingly significantly smaller with respect to standard mesomolecular or macromolecular systems. Moreover, in some phthalocyanine radicals the intermolecular interaction energy can be large, thus yielding a smaller effective activation energy. Several studies on the conductivity properties of Pc_2Lu and PcLi were performed [88]. These systems are respectively typical narrow- and broad-band intrinsic molecular semiconductors and have been used for the preparation of devices such as field-effect transistors [89]. They show electrical properties drastically different from all molecular compounds studied before. In fact, the activation energies of conduction of PcM (M = Cu, Ni) or PcH$_2$ are expected to be much higher than those found for Pc_2Lu and PcLi [88]. The room temperature conductivity in standard molecular crystals PcM is in all cases less than $10^{-10}\ \Omega^{-1}cm^{-1}$, with an activation energy of the order of 2 eV. On the other hand, the room temperature conductivity of a Pc_2Lu thin film and single-crystal is about $10^{-5}\ \Omega^{-1}cm^{-1}$, more than 5 orders of magnitude higher than that for PcCu or PcH. The experimental activation energy of conduction is $\Delta E \simeq 0.52$ eV. Remarkably, the room temperature conductivity of

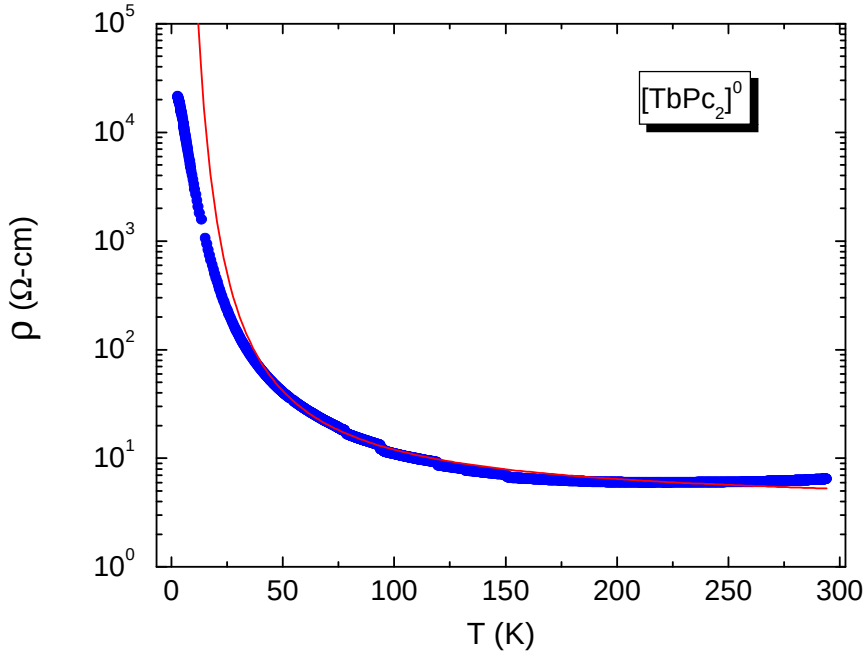

Figure 2.6: Temperature dependence of resistivity ρ, measured for a $[Pc_2\text{Tb}]^0$ crystal. Solid line represents the best fit of the activated trend in the 220 - 30 K region.

a single crystal of PcLi was $2 \cdot 10^{-3}\ \Omega^{-1}cm^{-1}$ with an activation energy of 0.2 eV. Contrary to the previous case, there is a strong disagreement between the experimental and calculated activation energies of conduction ($E_{theo} = 1.1$ eV). This clearly indicates a strong interaction between PcLi units, and collective electronic energy levels must be present. From spin dynamic measurement, the bandwidth was estimated to be of the order of 50 meV for Pc_2Ln and more than 1 eV for PcLi. These materials are therefore the first two members of the class of molecular semiconductors having either localized or collective electronic levels [88]. Moreover, the effective mobility of charge carriers found in thin films of Pc_2Ln, as determined from space charge limited currents, was exceptionally high, being more than 2 orders of magnitude higher than for other molecular compounds. This observation is of the utmost importance in considering how to obtain well-behaved devices, in particular bipolar transistors, in which the switching time is inversely proportional to the mobility of carriers.

2.3.1 Resistivity measurements in $[Pc_2\text{Tb}]^0$

In order to investigate the transport properties of the neutral terbium-(bis)phtha locyaninato, resistivity measurements on single crystal samples of $[Pc_2\text{Tb}]^0$ were performed. The experiments were carried out in the 2.8 - 294 K temperature range, with current along the crystal c-axis, DC mode, and by using a

four-terminal technique. Contacts were made by attaching 0.01 mm diameter gold wires to the samples with conductive paste and sub-μA currents were used. The samples were left free-standing to minimize thermal stress and consequent cracking. The voltage has been measured with a voltmeter with an internal impedance larger than 10 $G\Omega$. Three different crystals have been measured and they all showed an increasing resistance on cooling from 2.5 kohm to greater than 2 Mohms below 15 K. In Fig. (2.6) the temperature dependence of the resistivity for a crystal with a $2.72 \cdot 10.3$ area/lenght ratio is shown. The room temperature conductivity was found to be $\sigma \sim 10^{-1}\Omega^{-1}cm^{-1}$, much larger then the typical values of the other phthalocyanine-based compounds described in the previous section. The resistivity ρ behaviour with temperatures shows some interesting features. In fact, ρ presents an initial smooth decrease on cooling from its room temperature value $\rho \simeq 6.4\ \Omega \cdot cm$, till about 220 K. On the contrary, below T = 220 K, the resistivity shows an activated growth down to about 25 K. Noteworthy, the activation energy associated to the semiconductive trend is $\Delta E \simeq 11\ meV$, about one order of magnitude smaller with respect to PcLi crystal. This results again suggests the presence of a strong interaction between $[Pc_2\mathrm{Tb}]^0$ molecules, as happens in PcLi. The partial overlap between the a_2 orbitals of the adjacent molecules should favour electron delocalization, thus yielding the metallic behaviour at high temperatures. However, the low temperature insulating trend can be attributed to electrons correlations, which were found to be significant in Pc-based systems, particularly at half-band filling [90]. Therefore, due to the on-site Coulomb repulsion U, the hopping integral t among adjacent molecules can be easily overcame, leading to a Hubbard insulating behaviour. Hence, the activated behaviour of the resistivity should be ascribed to such correlation effects rather than to the band structure, which should typically lead to much larger activation energies. In addition, the band structure and, accordingly, the hopping integral t appear to sizeably depend on the local structure, in particular, on the buckling of the Pc ring plane and on the rotation of adjacent Pc rings [81]. Hence it is possible that at high T the crossover from a negative to a positive $d\rho/dT$ with increasing T, might be ascribed to those structural effects.

2.3.2 Surface-Supported Pc_2Tb Molecules

The future technological applicability of SMMs is presently hampered by the difficulty of adsorbing these molecules onto surfaces and by the lack of understanding on whether their magnetic properties are modified upon adsorption. Recently, single molecules and molecular clusters of Pc_2Tb were succesfully deposited on the Cu(111) surface in ultrahigh vacuum conditions using a dry imprint technique [52]. Scanning tunneling microscopy (STM) demonstrated that Pc_2Tb molecules adsorb on one Pc molecular plane in a flat lying configuration on the surface, preserving their molecular structure. In addition, experimental density of state investigation together with theoretical calculations based on density functional theory demonstrated that the magnetic properties

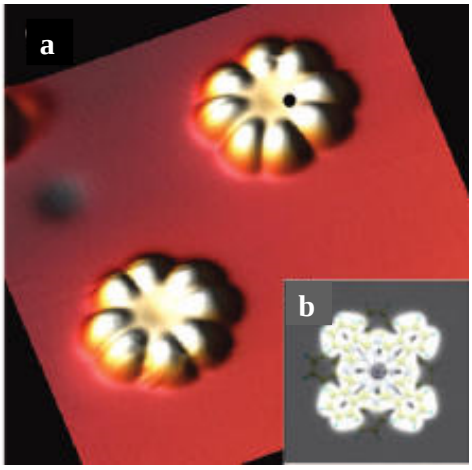

Figure 2.7: (a) Constant current topograph of two isolated Pc_2Tb molecules supported by the Cu(111) surface and (b) simulated STM image of an isolated Pc_2Tb molecule [52].

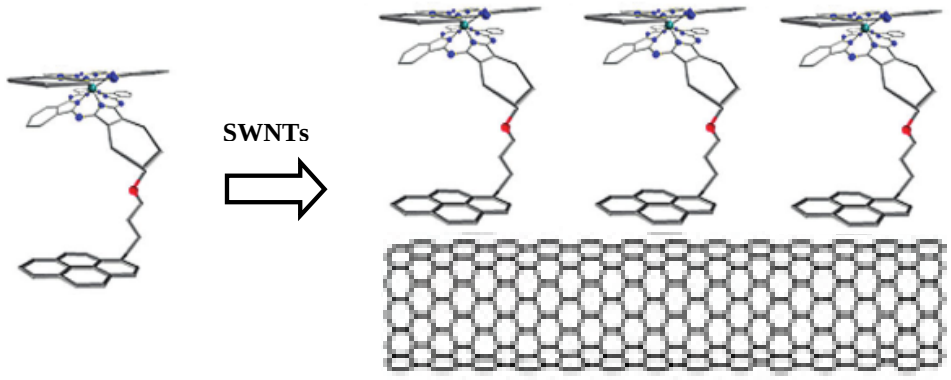

Figure 2.8: Schematic picture of heteroleptic pyrenyl-containing bis-phthalocyanines grafted on a single-walled carbon nanotubes .

of [Pc_2Tb] deriving from the Tb [III] ion are preserved even in the presence of a strong molecular interaction with the metal surfaces. In fact, the strong hybridization between the ligand molecular orbitals and the electron states of the metal surface completely suppresses the delocalized ligand spin system, but preserves the large magnetic moment of the Tb ion, which is only weakly affected by the presence of the surfaces [52]. This is possible thanks to the decoupling between the two spin systems, which plays a fundamental role in preserving the the SMM properties of surface-supported Pc_2Tb molecules. In addition, the molecular structures and the electronic transport properties of Pc_2Ln and PcLn molecules (Ln = Tb^{3+}, Dy^{3+} and Y^{3+}) on Au(111) surfaces have been investigated [79]. In particular, Tb-Pc and Dy-Pc molecules were found to exhibit p-type and ambipolar semiconducting properties, respectively. Thus, these molecules seem to be very suitable to be used as the active layer

in top- and bottom-contact thin-film organic field-effect transistors (OFETs), which probably represent the most prominent constituent of next generation microelectronis. On the other hand, the rich and well studied chemistry of phthalocyanines allows adding tailored functionalities to these SMMs, so as to organize them in hybrid structures [91] while the SMM behavior is maintained. In this direction, a new heteroleptic pyrenyl-containing bis-phthalocyanine, exhibiting typical properties of single molecule magnets, have recently been synthesized. The complex was successfully attached to single-walled carbon nanotubes (Fig. 2.8) (SWNTs) using π interactions of the pyrene-functionality with highly purified SWNTs. An investigation of the magnetic properties of the SMM-SWNT conjugate allowed to demonstrate that the SMM behavior is retained and even improved in the hybride systems, likely due to the suppression of intermolecular interactions, in contrast to many d-metal clusters on surfaces [92]. The obtained results propose the SMM-SWNT conjugate as a promising constituent unit in magnetic single-molecule measurements using molecular spintronics devices [62].

2.4 Ligand Field Levels Structure of $[Pc_2\mathbf{Ln}]^-\cdot \mathbf{TBA}^+$ Complex

In this section, the rare-earth SMMs typical features arising from the presence of *f*-electrons in a strong crystal field, are presented. The *f*-electrons in $[Pc_2\mathrm{Ln}]$-based complex possess properties which are close to those of isolated ions. Due to the strong spin-orbit coupling, in the framework of perturbation theory the total angular moment $\mathbf{J} = \mathbf{L} + \mathbf{S}$ associated with the electronic configuration of the lanthanide ion can be considered as a good quantum number for the total hamiltonian

$$\hat{\mathcal{H}} = \hat{\mathcal{H}}_0 + \hat{\mathcal{H}}_{SO} + \hat{\mathcal{H}}_{CF} + \hat{\mathcal{H}}_{Zee} \quad , \tag{2.2}$$

where the leading term $\hat{\mathcal{H}}_0$ comprises the intra-atomic Coulomb interactions and the second term $\hat{\mathcal{H}}_{SO}$ represents the spin-orbit coupling $\hat{\mathcal{H}}_{SO} = \xi_{LS}\mathbf{L}\cdot\mathbf{S}$. The perturbative terms $\hat{\mathcal{H}}_{CF}$ and $\hat{\mathcal{H}}_{Zee}$ are, respectively, the crystal field hamiltonian, inducing the partial removal of the degeneracy in J_z, and the Zeeman interaction, which yields a further shift in the energy levels structure. The knowledge of the ground multiplet J splitting is of crucial importance for understanding the magnetic properties of a lanthanide complex. The past studies on the multiplet structures of lanthanide *f* systems were reported only for the cases for which sharp emission or absorption bands or both were available. In $[Pc_2\mathrm{Ln}]$-based complex, however, neither fluorescence nor absorption spectra associated with lanthanide centers are obtainable because of low-lying *Pc*-centered energy levels quenching the lanthanide fluorescence and the extremely intense Pc-centered absorption bands concealing the lanthanide-centered bands. Ishikawa and collaborators first proposed a new indirect method to determine electronic structures of a series of dinuclear and

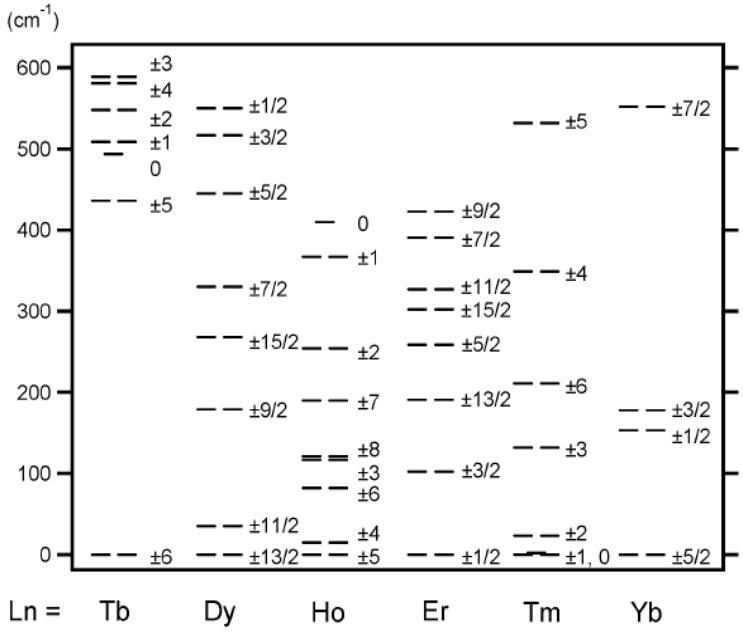

Figure 2.9: Energy diagram of the substates of the ground multiplets of $[Pc_2\text{Ln}]^- \cdot$ TBA$^+$ (Ln = Tb, Dy, Ho, Er, Tm, or Tb) determined in ref[47]. The J_z value of each substate is indicated to the right of the corresponding energy level.

mononuclear lanthanide complexes with phthalocyanine [93][47]. The exact magnetic hamiltonian of a system with orbital and spin angular moments **L** and **S** under external magnetic field **H** is

$$\hat{\mathcal{H}} = g\mu_B(\mathbf{L} + 2\mathbf{S}) \cdot \mathbf{H} + \hat{\mathcal{H}}_{CF} \quad , \tag{2.3}$$

where g is the Landè factor and μ_B is the Bohr magneton. The CF term belonging to the C_4 point group can be written as [94]

$$\hat{\mathbf{F}} = A_2^0\langle r^2\rangle\alpha\hat{\mathbf{O}}_2^0 + A_4^0\langle r^4\rangle\beta\hat{\mathbf{O}}_4^0 + A_4^4\langle r^4\rangle\beta\hat{\mathbf{O}}_4^4 + A_6^0\langle r^6\rangle\gamma\hat{\mathbf{O}}_6^0 + A_6^4\langle r^6\rangle\gamma\hat{\mathbf{O}}_6^4 \quad . \tag{2.4}$$

In Eq. (2.4) the $\hat{\mathbf{O}}_k^q$ matrices are polynomials of the total angular momentum matrices J^2, J_z, J_- and J_+, the coefficients α, β and γ are the constants tabulated by Stevens [95] and the z axis is chosen to coincide with the C_4 axis. From the work of Stevens, it is indeed possible to represent any operator acting only on the orbital moment as an equivalent operator acting on states of total **J**. Hence, the oscillations of the crystalline electric field, which act only on the orbital part of **J**, in the limit of strong spin-orbit coupling can be transformed to operate directly on states of **J** whith suitable multiplicative factors. The coefficients $A_k^q\langle r^k\rangle$ are the CF parameters to be determined. Since they are expected to vary fairly regularly from the f^{18} system to the f^{13} system, the

assumption that each parameter is expressed as a linear function of the number n of f electrons was made:

$$A_k^q\langle r^k\rangle(n) = a_k^q + b_k^q(n-10) \qquad n = 8, 9, ..., 13 \quad . \tag{2.5}$$

Through ten-dimensional simplex minimization calculations, which moves both a_k^q and b_k^q, the best set of fully optimized CF parameters was obtained [47]. A set of $A_k^q\langle r^k\rangle$ coefficients and a finite external field determine the wave functions and magnetic moments of all the substates. The substate structures of a series of lanthanide complexes having isomorphic structures $[Pc_2\mathrm{Ln}]^-\cdot$ TBA^+ (Ln = Tb, Dy, Ho, Er, Tm, Yb) were determined by finding the set of the LF parameters that reproduce simultaneously the ^{1}H NMR paramagnetic shifts $\Delta\delta$ and the temperature dependence of magnetic susceptibilities χ_m [47]. In particular, in Tb-based complex the lowest substates are $|m = 6\rangle$ and $|m = -6\rangle$, which have the largest J_z values within the $J = 6$ ground state (Fig. 2.9). This indicates the presence of a strong uniaxial magnetic anisotropy along the C_4 axis. The next sublevel lies at about 400 cm^{-1}, yielding a predominant population of the lowest levels up to relatively high temperature (the population ratio remains 99% at 100 K, according to the Boltzmann distribution). The second interesting system is $[Pc_2\mathrm{Dy}]^-\cdot$ TBA^+, in which the lowest substates are $|m = 13/2\rangle$ and $|m = -13/2\rangle$, possessing the second largest J_z values in the $J = 15/2$ state. The next substates $|11/2\rangle$ and $|-11/2\rangle$ lie at about 40 cm^{-1} above, thus the ground state population is more than 99% up to about 10 K.

As it will be shown in Chapter 3, important information about the energy level structure of Tb- and Dy-based compounds can be derived from DC magnetization and AC suceptibility measurements. In fact, in $[Pc_2\mathrm{Tb}]^0$ complex static and dynamic susceptibily analysis allow to estimate an energy barrier for the spin reversal of about 750 K, a value much larger than that reported by Ishikawa and collaborators for $[Pc_2\mathrm{Tb}]^-\cdot$ TBA^+ complex [32]. The estimated barrier is also larger than that derived from Ishikawa in the same nominal compound [49]. As regard $[Pc_2\mathrm{Dy}]^0$, static uniform susceptibility behaviour with temperature allows for the determination of the ground spin multiplet low-energy level structure. The derived energy splitting between the ground states and the first excited levels was found to be in good agreement with the value estimated from AC susceptibility analysis.

In Chapter 5, it will be shown how the anisotropy energy barriers for all the compounds under investigation were deduced by means of Nuclear Magnetic Resonance and Muon Spin Relaxation techniques. Though macroscopic and microscopic results present some differences in the low temperature range, the values for the high temperature activated barriers estimated from macroscopic and microscopic techniques were found to be very similar.

In the next section, the basic mechanism leading the transitions among CF levels will be discussed. In fact, the interaction between the magnetic spin levels and the lattice vibrations is on the base of the magnetization relaxation processes.

2.5 Relaxation Processes of Lanthanide Ions

The relaxation mechanism of lanthanide ions in crystalline environments have been understood in terms of the energy exchange processes between the paramagnetic ions and phonon radiation, which are induced by the modulation of the crystal or ligand field under the action of the lattice vibrations [94] [96]. In the last 1930s Heitler and Teller [97] and Fierz [98] first showed that the modulation of the crystalline field led to a spin-lattice interaction much stronger than that produced by modulation of the magnetic dipolar interaction. Their qualitative studies were followed by quantitative investigations of the effects of modulations of the crystalline electric field in the iron group alums by Kronig [99] and Van Vleck [100], but their results did not agree with experimental findings. Later, in the 1960s, investigations of spin-lattice relaxation in rare-earth salts by Orbach and collaborators [101] led to more accurate results, which seemed to be in fair agreement with theory. The orbit-lattice interaction is a dynamic crystalline field effect, e.g. the change in the crystalline electric field upon a deformation of the equilibrium configuration in the surrounding ions. It is thus natural to expand the orbit-lattice interaction potential $V_{o.l.}$ with the powers of the fluctuating strain tensor $\tilde{\varepsilon}$ caused by the lattice vibrations [101]:

$$V_{o.l.}(j) = \sum_{n,m} V_n^m(\mathbf{r_j})\varepsilon_{nm}(\mathbf{r_j}) \quad , \tag{2.6}$$

where $\mathbf{r_j}$ is the radius vector to the j-th paramagnetic ion site. There are three major processes to be considered for the transition between the lowest two substates: (1) the one phonon (or direct) process [99][100], in which a phonon of the same energy as the energy difference δ_{ab} between the spin-up and spin-down states is absorbed or emitted by the spin system (Fig. 2.10). The two levels can be split either by the Zeeman interaction or by the ligand-field potential or both; (2) the Raman process [100], where a phonon of any energy $h\nu_p$ is scattered by the spin system generating a phonon with an energy of $h\nu_p + \delta_{ab}$ or $h\nu_p - \delta_{ab}$; (3) the Orbach process [101], involving a phonon absorption by a direct process to excite the spin system to a higher state at an energy Δ above the lowest sublevels, followed by the emission of another phonon with an energy of $\Delta + \delta_{ab}$ or $\Delta - \delta_{ab}$ (Fig. 2.11).
Consider the hypothetical sets of states of figure (2.10). The populations N_a

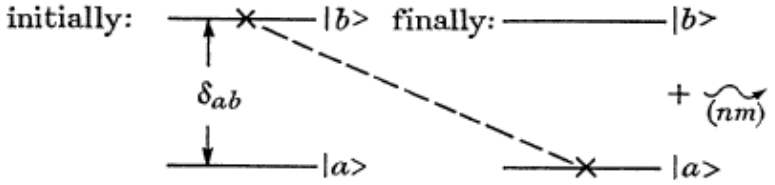

Figure 2.10: Schematic diagram of the direct process. A single transition is made from $|b\rangle$ to $|a\rangle$ and a phonon of energy δ_{ab} is emitted.

and N_b of the states $|a\rangle$ and $|b\rangle$ respectively are supposed to be given. The system is prepared at temperature $T_S \neq T$, where T_S is the spin temperature and T is the lattice temperature. The spin temperature T_S is defined by the relation $N_b/N_a = exp(-\delta_{ab}/K_B T_S)$. The lattice is assumed to be in closed contact with a heat bath of infinite heat capacity at the constant temperature T. The orbit-lattice interaction will induce transitions between the states $|b\rangle$ and $|a\rangle$ and we ask for the rate at which the spin system can come to thermal equilibrium with the lattice by means of emission or absorbtion of a single phonon. From first-order time-dependent perturbation theory, the probability $W_{b\to a}$ per unit time of making transitions between state $|b\rangle$ and $|a\rangle$ induced by the orbit-lattice interaction (2.6) is

$$W_{b\to a} = \frac{2\pi}{\hbar}|\langle a|\sum_j V_{o.l.}|b\rangle|^2 \rho(E_{ab}) \quad , \tag{2.7}$$

where $\rho(E)$ is the phonon radiation field energy density and j goes over all spin sites in the state $|b\rangle$. Using expansion (2.6) for $V_{o.l.}$ and assuming $\rho(E_{ab}) = \delta(E_b - E_a)$, Eq. (4.41) becomes

$$W_{b\to a} = \frac{2\pi}{\hbar}\int |\sum_{n,m,j}\langle a|V_n^m(\mathbf{r_j})\varepsilon_{nm}(\mathbf{r_j})|b\rangle|^2 \frac{4\pi V}{(2\pi)^3} 3k^2 dk\delta(E_b - E_a) \quad , \tag{2.8}$$

where we have summed over all phonon modes. Here, $\mathbf{k}$ is the wave vector of the phonon with mean velocity v (neglecting the differences in velocity between phonon modes), V the volume of the crystal and E_b and E_a are the initial and final system energies respectively. From Eq. (2.8), it is possible to derive the final expression for $W_{b\to a}$ [101]

$$W_{b\to a} = \frac{3}{2\pi\rho v^5\hbar}\left(\frac{\delta_{ab}}{\hbar}\right)^3 |\langle a|\sum_{n,m} V_n^m|b\rangle|^2 N_b(N+1) \quad , \tag{2.9}$$

and, similarly, the transition probability $W_{a\to b}$ for the inverse process which involves transitions from $|a\rangle$ to $|b\rangle$ with the absorption of a phonon [101]

$$W_{a\to b} = \frac{3}{2\pi\rho v^5\hbar}\left(\frac{\delta_{ab}}{\hbar}\right)^3 |\langle a|\sum_{n,m} V_n^m|b\rangle|^2 N_a N \quad . \tag{2.10}$$

The net transition probability per unit time to go from $|b\rangle$ to $|a\rangle$, dN_b/dt, is equal to $W_{b\to a}$ minus $W_{a\to b}$:

$$dN_b/dt = \frac{3}{2\pi\rho v^5\hbar}\left(\frac{\delta_{ab}}{\hbar}\right)^3 |\langle a|\sum_{n,m} V_n^m|b\rangle|^2 [N_b(N+1) - N_a N] \quad . \tag{2.11}$$

If all other levels of the rare-earth ion are essentially unpopulated, or their population are assumed indipendent of the lowest two states, it results $dN_b/dt =$

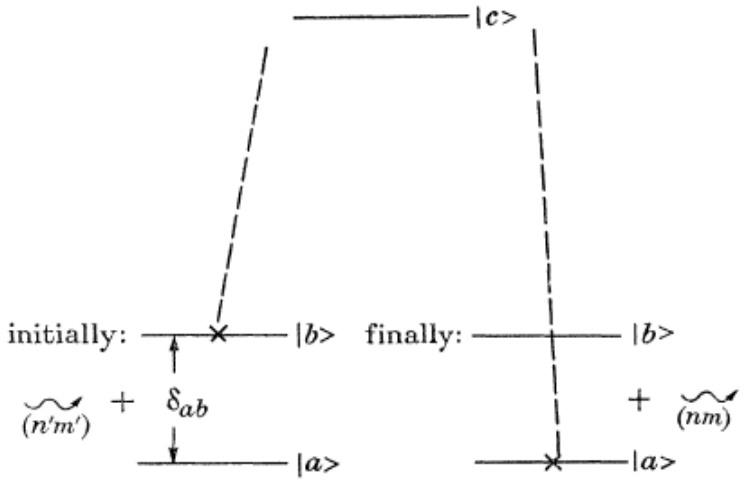

Figure 2.11: Schematic diagram of the two-phonon process. A phonon of energy $\hbar\omega_{n'm'}$ is absorbed by the spin system and an intermediate transition form $|b\rangle$ to $|b\rangle$ occurs. A phonon of energy $\hbar\omega_{nm}$ is then emitted and a transition occurs from $|c\rangle$ to $|a\rangle$ completing the process.

$-dN_a/dt = 1/2d(N_b - N_a)/dt$. Thus, if we define $(N_b - N_a)_{T_S(t)}$ the population difference associated with the spin temperature T_S at the time t, $T_S(0)$ the initial spin temperature and by replacing the thermal equilibrium N by its statistical average $N = [exp(\hbar\omega/KT) - 1]^{-1}$, it can be easily found

$$(N_b - N_a)_{T_S(t)} - (N_b - N_a)_T = [(N_b - N_a)_{T_S(0)} - (N_b - N_a)_T] \cdot exp(-t/\tau) \quad , \quad (2.12)$$

where the relaxation rate $1/\tau$ has been defined as

$$\frac{1}{\tau} = \frac{3}{2\pi\rho v^5 \hbar} \left(\frac{\delta_{ab}}{\hbar}\right)^3 coth\left(\frac{\delta_{ab}}{2K_B T}\right) |\langle a| \sum_{n,m} V_n^m |b\rangle|^2 \quad . \quad (2.13)$$

If $\delta_{ab} \ll K_B T$, the relaxation time expression reduces to the well known form

$$\frac{1}{\tau} = \frac{3\delta_{ab}^2 K_B T}{\pi\rho v^5 \hbar^4} |\langle a| \sum_{n,m} V_n^m |b\rangle|^2 \quad , \quad (2.14)$$

which gives a linear dependence on T.

Differently from direct processes, Raman and Orbach transitions involve two-phonon processes, which are of the next higher order in time-dependent perturbation theory. Indeed, they involve $V_{o.l.}$ taken twice and an intermediate excited state $|t\rangle$, resulting in the creation and destruction of two phonons, whose difference in energy equals the splitting in the partecipant spin states (Fig. 2.11). The effective orbit-lattice interaction for two phonon processes is then of the form

$$V_{eff} = \sum_t \frac{V_{o.l.}|t\rangle\langle t|V_{o.l.}}{(E_0 - E_t)} \quad , \quad (2.15)$$

where $(E_0 - E_t)$ is the energy difference between the initial and the intermediate state and the summation is over all the accessible intermediate states $|t\rangle$. It can be demonstrated [94] that in the case of non-Kramers systems, which contain even number of electron as in a Tb^{3+} ion, the relaxation time for Raman and Orbach processes, respectively, obey the following expressions:

$$\left(\frac{1}{\tau}\right)_r = R_r T^7 \tag{2.16}$$

and

$$\left(\frac{1}{\tau}\right)_{Or} = R_{Or}\Delta^3\{exp(\Delta/K_B T) - 1\}^{-1} \quad , \tag{2.17}$$

where R_r and R_{Or} are proportional to matrix elements or products of matrix elements of $V_{o.l.}$ between $|a\rangle$ and $|b\rangle$. As regard Kramers systems, containing odd numbers of electrons as in Dy^{3+} ion case, direct and Orbach processes lead to the same expressions for relaxation times as in non-kramers complexes. Instead, the relaxation time associated with Raman processes becomes

$$\left(\frac{1}{\tau}\right)_r = R_r T^9 + R'_r(\delta_{ab}/K_B)^5 T^7 \quad . \tag{2.18}$$

In the range where $\delta_{ab} \ll K_B T \ll \Delta$, the Orbach term is approximated by $R_{Or}\Delta^3 exp(-\Delta/K_B T)$, which indicates a thermally activated character of this process. If the Orbach process is dominant, it is then possible to estimate the value of Δ, corresponding to the "barrier height" in the double-well-potential picture, by the Arrhenius analysis of the magnetization relaxation time τ dependence on temperature.

2.6 Raman Spectroscopy in $[Pc_2\mathbf{Ln}]^0$ Molecular Magnets

Raman spectroscopy is a versatile technique for studying the intramolecular vibrational modes involved with the spin relaxation processes in phthalocyanine compounds. According to the single crystal X-ray diffraction structural analyses of bis(phthalocyaninato) rare earth complexes $(Pc)_2$Ln (Ln = Y, La, Ce, Pr, Nd, Er, Lu), their static symmetry is D_4 or D_{4d} depending on the twist (skew) angle between the two macrocyclic rings, which ranges from 38° to 45° [102][103]. On the other hand, to interpret the observed Raman vibrational spectra, local C_{4v} symmetry for the fragment M(Pc) was reasonably assumed [104]. The C_{4v} symmetrical unsubstituted phthalocyanine metal fragment M(Pc) contains 57 atoms, so there are 63 IR-active and 105 Raman-active modes among the 168 total normal vibrational modes. There are only $22A_1$ totally symmetric fundamental vibrations active in the spontaneous Raman spectra, although the fragment M(Pc) contains a large number of atoms and

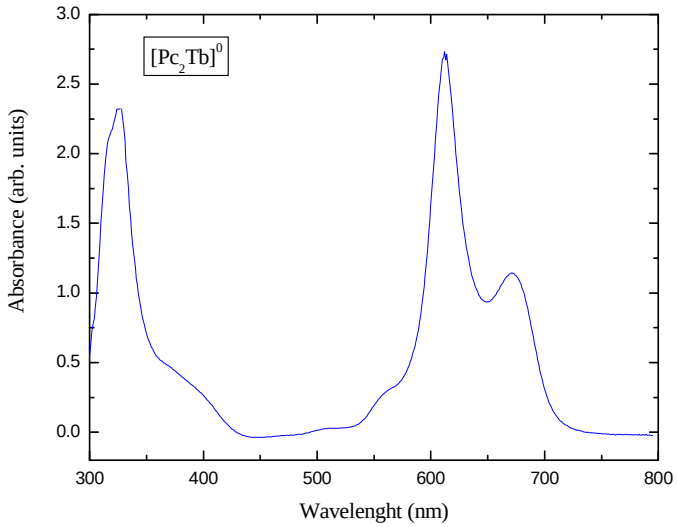

Figure 2.12: The UV-vis spectra of $[\text{Pc}_2\text{Tb}]^0$ in $CHCl_3$.

thus possesses many possible normal vibrational modes. In the resonance Raman scattering, a number of new frequencies could be attributed to the related $22B_1$, $20B_2$, and 41E type in view of the Herzberg−Teller mechanism. The vibrational modes for the fragment M(Pc) with C_{4v} symmetry may be summarized as follows, where "IR" and "R" represent Infrared- and Raman-active modes, respectively.

$$\Gamma_{vib} = 22A_1(IR, R) + 19A_2 + 22B_1(R) + 20B_2(R) + 41E(IR, R) \quad . \quad (2.19)$$

A_1 and E modes are both IR- and Raman-active. B_1 and B_2 modes are Raman-active and A_2 modes are vibrationally inactive.
The absorption spectra of Pc_2Tb show a typical B band at $316 - 325$ nm with a weak shoulder peak at the lower energy side of 342−358 nm (Fig. 2.12). The Q bands appear as a strong absorption in the range of 658−689 nm together with the vibronic components at 570−596 nm and 595−618 nm. The Raman spectra in $[Pc_2\text{Ln}]^0$ complexes (Ln = Dy, Tb and Y) show a large number of vibrational modes, yet revealing the high molecular symmetry of these compounds. The observed Raman spectroscopic bands (Fig. 2.13) were partially assigned, based on the previous description of normal modes for bis(phthalocyaninato) metal derivatives [105]. Due to the similar electronic structure and electronic absorption properties, the three compounds under investigation show similar Raman characteristics.

2.6.1 Experimental Details

Resonance Raman spectra were recorded on a few grains of $[Pc_2\text{Ln}]^0$ (Ln = Tb, Dy or Y) powders by means of a J.Y. LabRAM HR spectrometer, equipped with a He-Ne laser excitation source emitting at wavelength of 632.8 nm and

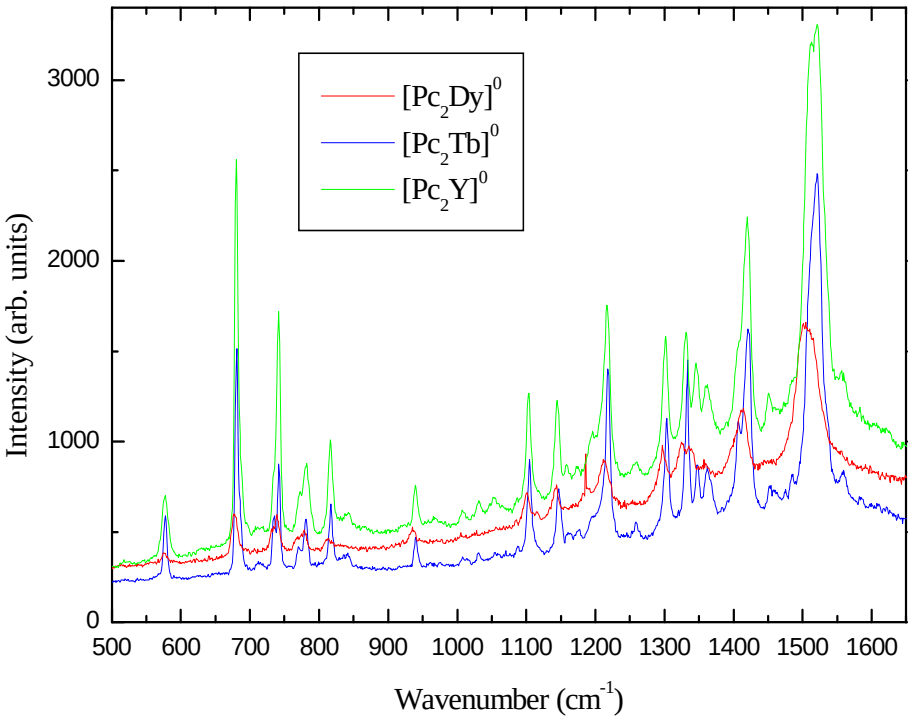

Figure 2.13: Raman spectra on powders of $[Pc_2\mathrm{Ln}]^0$ (Ln = Dy, Tb and Y) in the region of 500-1800 cm^{-1}, with excitation at 633 nm.

at the maximum power of 20 mW, and by means of a Xplora J.Y. spectrometer equipped with a diode laser emitting at 785 nm (20 mW) . The microscopes work in back scattering mode and were fitted with three objective lenses (10x, 50x and 100x). For these experiments, the 50x objective was employed giving a spot size of about 1 μm and a spectral resolution <2 cm^{-1}. Laser power at the sample was approximately 0.08 mW.

2.6.2 Raman Spectra with Excitation at 632.8 nm

With laser excitation at 633 nm, which is nearly in resonance with the Q band absorptions at $658 - 689$ nm, Raman bands in the range of $1300 - 1600$ cm^{-1} derived from isoindole ring stretching vibrations and the aza group stretching are selectively intensified. For Pc_2, the weak bands at ca. $574 - 577$ cm^{-1} and $812 - 817$ cm^{-1} and a band at $678 - 680$ cm^{-1} with medium or strong intensity are attributed to phthalocyanine breathing [106], and the wavenumbers of all these modes show a dependence on the rare earth size, slightly blue-shifting along with the lanthanide contraction. This is not true for the yttrium double-decker compound, which deviates from the linear relationship between wavenumber and ionic radii, established for the other tervalent rare-earth complexes. This deviance is probably due to the intrinsic difference between yttrium and the lanthanides, namely the absence of f electrons. The

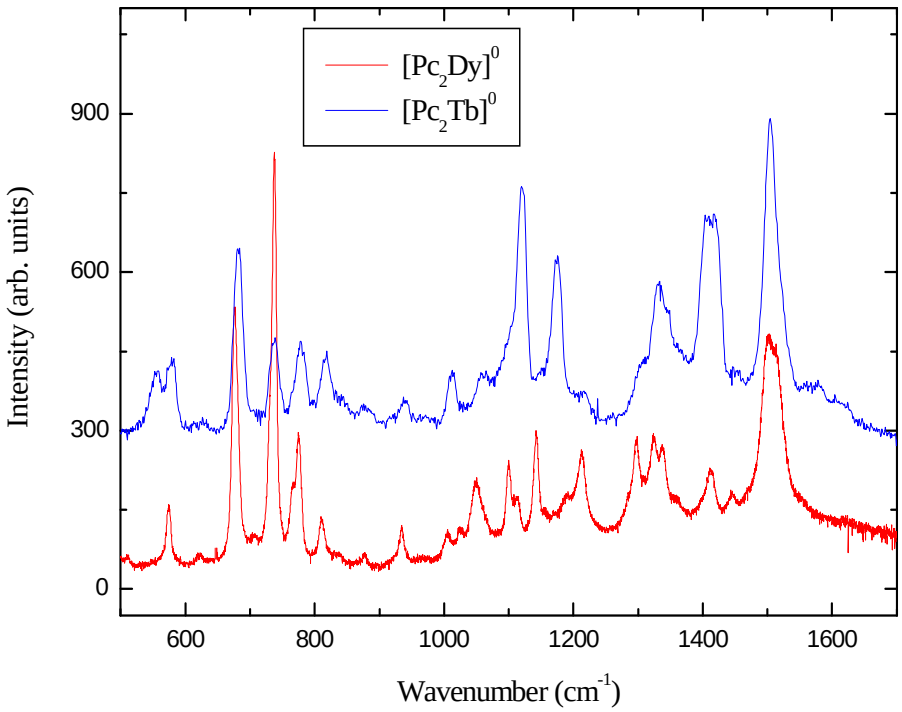

Figure 2.14: Raman spectra on powders of $[Pc_2Ln]^0$ (Ln = Dy, Tb) in the region of 500-1700 cm^{-1}, with excitation at 785 nm.

medium band at ca. 740 cm^{-1} is due to aromatic phthalocyanine C−H wagging [106]. In the range of $1000-1300$ cm^{-1}, there are several weak or medium bands lying at ca. 1006, 1030, 1103, 1174, 1196, 1215, and 1301 cm^{-1}, which are assigned to aromatic C−H bending. The pyrrole breathing presents two bands in the region of around 1140 and 1500 cm^{-1}. The former comprises a single peak with medium intensity at ca. 1138-1145 cm^{-1} whereas the latter overlaps with the aza stretching vibration in the same region to form a broad band at 1495-1525 cm^{-1} for all the three compounds. The intense band in the range 1409-1423 cm^{-1} and the weak band in the range 1444-1451 cm^{-1} are attributed to isoindole stretching vibrations. The former intense band discussed above, together with the aza stretching band at 1512-1525 cm^{-1}, shows dependence on the rare earth radius, also shifting to higher energy along with the rare earth contraction (exepting for Pc_2Y compound).

2.6.3 Raman Spectra with Excitation at 785 nm

Using the excitation laser line at 785 nm that is far away from resonance with the Q absorption bands, the macrocyclic ring deformation and ring radial vibrations between 500 and 1000 cm^{-1} in the Raman spectra of Pc_2Ln (Ln = Tb, Dy) are selectively intensified (Fig.2.14). In fact, the Pc breathing at 675-679 cm^{-1} and the aromatic C-H wagging at ca. 739 cm^{-1} are some of

the most intense bands. The band locating at 1327-1329 cm^{-1} with medium intensity is assigned to the pyrrole C=C stretching vibrations coupled with benzene C=C stretching vibrations and the one at about 1342 cm^{-1} to the isoindole stretching vibrations. Similar to those excited with 633 nm laser line, the bands of the coupled pyrrole C=C and aza C=N stretching vibrations in the region of 1507-1521 cm^{-1} overlap to form a broad, unresolved envelope. The vibrations of Pc_2Ln at 675-679 cm^{-1} assigned to the Pc breathings, at 1407-1422 cm^{-1} attributed to the isoindole stretching vibrations, and at 1508-1521 cm^{-1} due to the coupling of aza and pyrrole stretching vibrations are found to slightly shift to higher energy in Tb-based compound, due to the small radius contraction of terbium with respect to dysprosium ion [106].

2.7 Specific Heat in $[Pc_2\mathbf{Tb}]^0$ Molecular Magnet

2.7.1 Experimental details

The specific heat measurements were performed by using a MagLab^{Exa} Measurement System and an Oxford Instruments microcalorimeter. Differently from the traditional adiabatic calorimetry, which involves supplying a thermally isolated sample with a known amount of heat and measuring the change in its temperature, the calorimetry technique used here is known as the time-constant or relaxation method and it must be employed when working at cryogenic temperatures. It consists of changing step-wise the the power supplied to the sample. Associated with the new power level is a new equilibrium temperature at which the rate of heat loss to the surroundings matches the rate of heating. The chip temperature will grow exponentially toward this new level according to

$$T = T_1 + \Delta T_0(1 - exp(-t/\tau)) \tag{2.20}$$

where T_1 is the initial temperature and $T_1+\Delta T_0$ is the final equilibrium temperature (see Fig. 2.15). The time constant $\tau = R_{TH}C$ is the product of the heat capacity of the chip and the effective thermal resistance between the sample and its surroundings. The thermal resistance is obtained from the relation $R_{TH} = \Delta T_0/\Delta P$. This quantity, considered infinite in the adiabatic case, now becomes an integral part of the measurement. The heat capacity can then be calculated as

$$C = \frac{\tau}{R_{TH}} \tag{2.21}$$

If the temperature increment is small compared with T_1, then the heat capacity is approximately that of the sample at the initial temperature T_1. In order to perform this measurement, it is necessary to have a means of supplying heat to the sample and of measuring its temperature. In addition, the sample must be reasonably well isolated thermally from its surroundings so that its thermal time constant is not too small. The heater and thermometers should have a

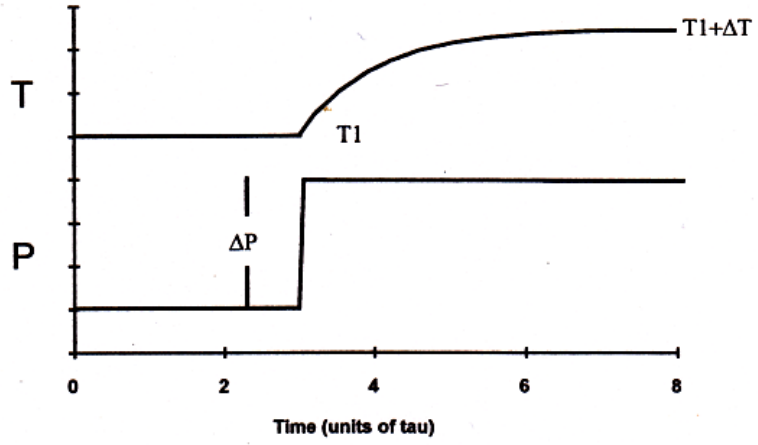

Figure 2.15: Power and temperature time evolution during a transient.

small heat capacity compared with that of the sample in order to minimize errors due to addenda subtraction. They must also be in intimate thermal contact with the sample so that they all act as one thermal unit. In Appendix some details of the Oxford Instrument calorimeter are described.

2.7.2 Analysis of Results

The molar specific heat was measured in the temperature range 4 - 170 K (Fig. 2.16). The large number of atoms contained in one molecule gives rise to a huge lattice contribution to the specific heat in the whole investigated range of T. Thus, the magnetic contribution given by the two-level Schottky model

$$C_{Sch}(T) = R\left(\frac{\Delta}{T}\right)^2 \frac{exp(\frac{\Delta}{T})}{[1+exp(\frac{\Delta}{T})]^2} \tag{2.22}$$

is masked by the lattice specific heat. In Eq. (2.22), Δ is the energy separation between the two levels and $R = N_A K_B$ is the molar gas constant. In zero applied field, $\Delta \sim 800$ K corresponds to the energy gap which separates the lowest levels with $J_z = \pm 6$ from the first excited states $J_z = \pm 5$. The two-level system specific heat shows a peak at about T = 330 K and it is therefore negligible in the temperature range under examination. The application of an external magnetic field H = 3 T leads to the Zeeman splitting of the lowest levels $J_z = \pm 6$, given by $\Delta E_{Zee} = 12 g \mu_B H \simeq 36K$. The corresponding two-level system specific heat is shown in the inset of Fig. (2.16). This contribution is about one order of magnitude smaller than lattice contribution at T = 15 K, where the Schottky peak appears, therefore it does not affect the total specific heat. In fact, the temperature dependence of the measured specific heat does not depend on the external magnetic field (Fig. 2.16). Instead, the plot of

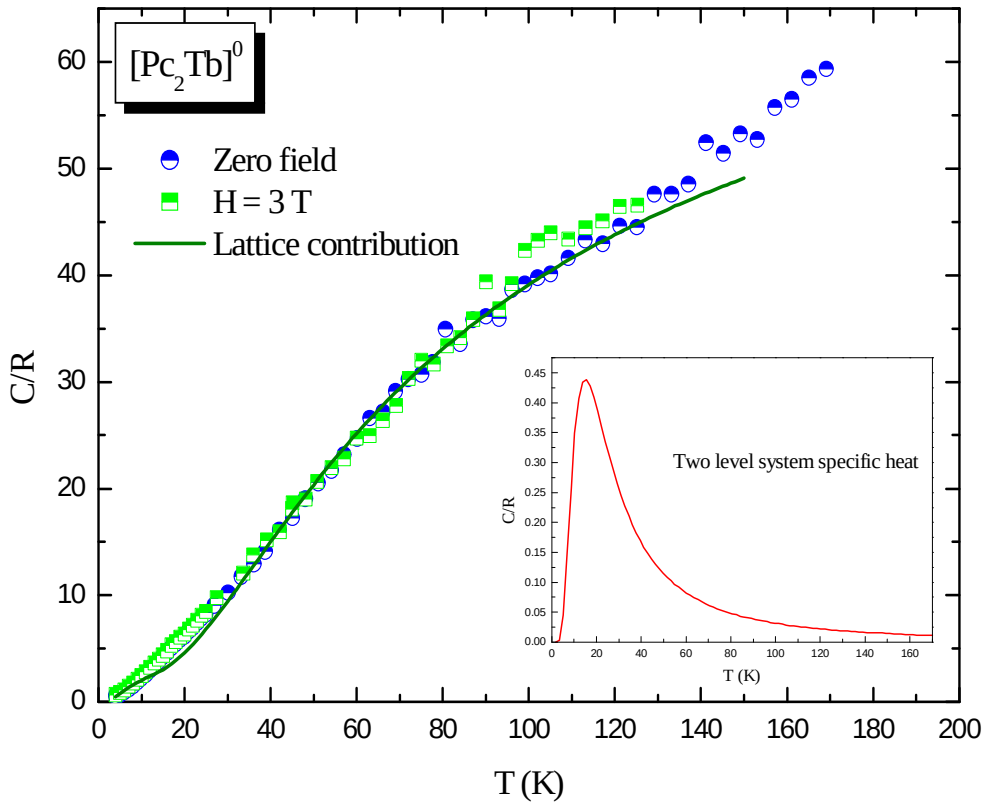

Figure 2.16: Temperature dependence of molar specific heat in the gas constant R units, in the $[Pc_2\mathrm{Tb}]^0$ compound. The data taken in zero applied field (blue circles) and in H = 3 T (light green squares) show the same trend indicating that the magnetic contribution to specific heat is negligible with respect to lattice contribution (solid green line), derived according to Eq. (2.23). In the inset, the two level system molar specific heat, in the R units, associated with an energy barrier $\Delta = 36K$.

C(T) can be reproduced by using a combination of Debye- and Einstein-like contributions [107]:

$$C_{latt}(T) = 9R\left(\frac{T}{\theta_D}\right)^3 \int_0^{\theta_D/T} \frac{x^4 e^x dx}{(e^x-1)^2} + pR\frac{(\Delta_E/T)^2 e^{(\theta_E/T)}}{(e^{(\theta_E/T)}-1)^2} \quad . \qquad (2.23)$$

From Eq. (2.23), the estimated Debye temperatures is $\theta_D \approx 40$ K, the Einstein temperature is $\theta_E \simeq 180$ K and the involved optical branches are $p \simeq 50$. However, in the temperature range 4-20 K, when the integral in Eq. (2.23) can be considered temperature independent and the Einstein-like contribution can be neglected, C(T) can be nicely fitted by a power low $C(T) \sim T^D$,

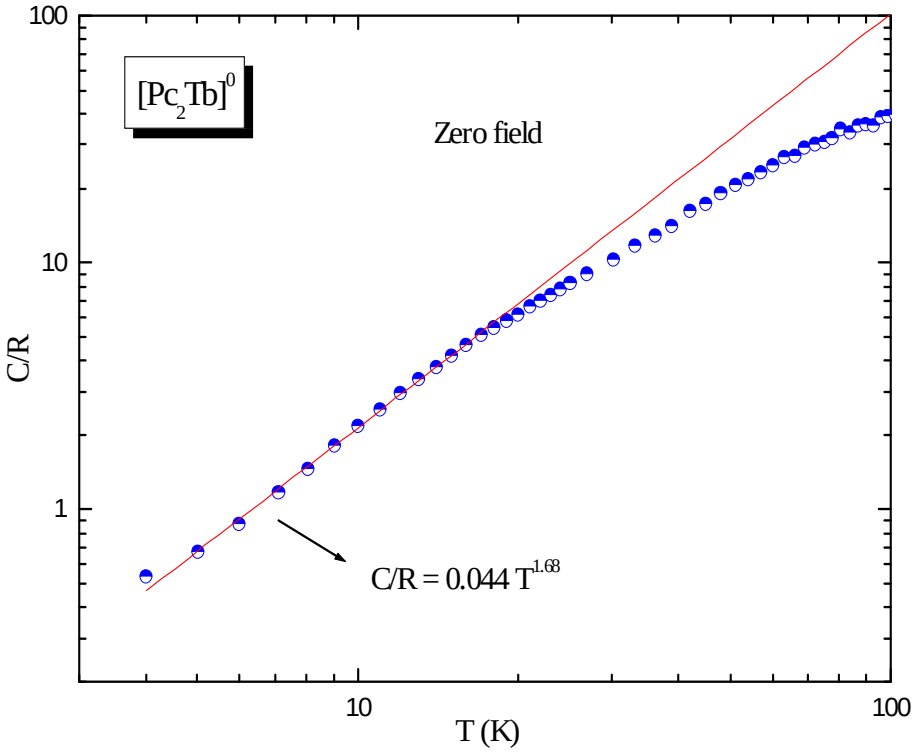

Figure 2.17: Temperature dependence of molar specific heat in the gas constant R units, in the range 4-20 K, for the $[Pc_2Tb]^0$ compound. The experimental data can be approximated with a power law $C/R(T) \sim T^D$, with $D = 1.68$.

with $D = 1.68$ (Fig. 2.17), which reproduces the Debye contribution better than the commonly used T^3 law. In fact, the specific heat low temperature behaviour $C \sim T^D$ reflects the dimensionality D of the lattice. The estimated value D = 1.68 is then an evidence of the low-dimensionality of the system, in which $[Pc_2Tb]^0$ molecules are piled up forming mono-dimensional chains. The vibrational modes propagate preferentially along the chains, even if a weak coupling among chains is present ($1 < D < 2$). This result is quite similar to what obtained in other molecular magnets, like Fe_{10} and Fe_6, with $D \sim 2.7$ [108]. Remarkably, similar power law with $D \sim 2.4 - 2.8$ was used to describe the lattice specific heat in $(TMTSF)_2X$ ($X = PF_6$ and AsF_6) and $(TMTTF)_2Br$ salts and ascribed to special low-dimensional phonon modes in those systems [109].

Chapter 3

Bulk Magnetic Properties of Pc_2Ln Molecular Magnets

In this chapter, the bulk magnetic properties of Pc_2Ln (Ln = Tb, Dy, Y) molecular magnets are described, starting from the analysis of their static and dynamic susceptibility. In diluted $[Pc_2\text{Tb}]^-\text{TBA}^+_N$ complexes, the magnetic properties were found to strongly depend on the magneto-thermic history, which crucially influence the arrangement of TBA groups around the Pc_2Tb molecules, thus yielding different crystal field effects on the rare-earth ion. The importance of the role of TBA matrix will be also evidenced by the nuclear spin-lattice relaxation rates measurements and by the correlation time dependence on temperature, reported later on in Chapter 5. On the other hand, in the neutral $[Pc_2\text{Tb}]^0$ and $[Pc_2\text{Dy}]^0$ the bulk magnetic properties were found to be independent on the magneto-thermic history. From the static uniform susceptibility analysis, is thus possible to derive the low-energy crystal field level structure for both samples. The results are compatible with those derived from the AC susceptibility and also in satisfactory agreement with the findings obtained by means of NMR and MuSR.

Finally, the magnetic properties of the $[Pc_2\text{Y}]^0\text{CH}_2\text{Cl}_2$ compound will be consider separately. In fact, due to the closed-shell configuration of the Y^{3+} ion, the magnetism of this system is solely associate to the unpaired π electron delocalized between the two phthalocyanine rings. The onset of antiferromagnetic interactions at low temperature will be demonstrated in the end of this chapter.

3.1 Technical aspects and experimental details

3.1.1 The SQUID Magnetometer

DC magnetization and AC susceptibility measurements were performed by means of an MPMS-XL7 (Magnetic Property Measurement System) Quantum

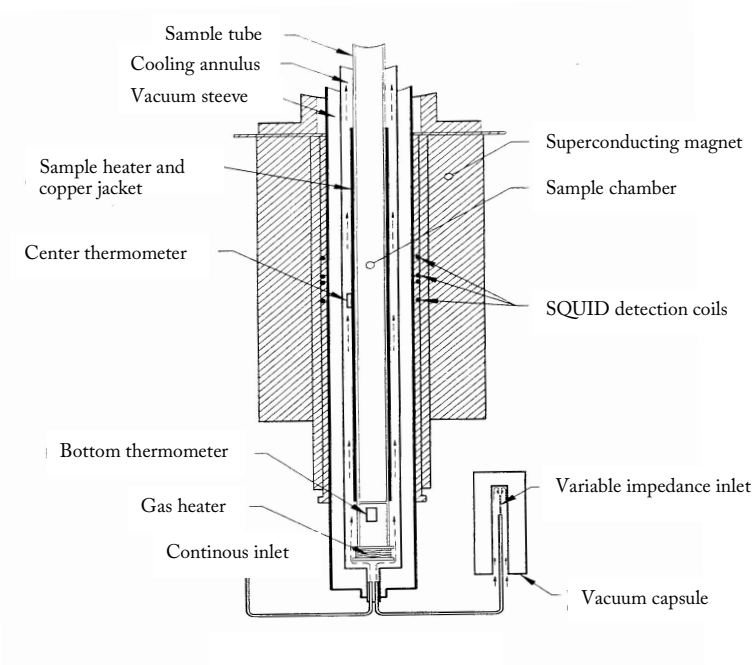

Figure 3.1: Probe cross section of the SQUID magnetometer.

Design SQUID magnetometer, able to detect magnetic moments in the range [10^{-7} emu - 2 emu]. The principal components of this measurements system comprise a Temperature Control System, which provides for accurate control of the sample temperature in the range 2 K - 400 K, through the control of the heat flow into the sample space and of the gas flow, in order to provide enough cooling power. Then, a Magnet Control System Current provides magnetic fields from zero to positive and negative 7 tesla. The rf SQUID detector is the heart of the magnetic moment detection system and it will be described below. It provides reset circuitry, auto-ranging capability and highly balanced second-derivative sample coil array. The Sample Handing System allows for rotating the sample smoothly through the detection coils without transmitting undue mechanical vibrations to the SQUID. Finally, the Computing Operating System provides the option of working under standard sequence controls, or diagnostic controls which will invoke individual functions.

The extraordinary sensivity to magnetic moments of materials is based on the rf-SQUID (Superconductive QUantum Interference Device). A SQUID device consist of a closed superconducting (SC) loop including one or two Josephson junctions in the loop's current path. Because of the quantized state of the SC ring and the strong non-linear behaviour of the Josephson junction, the SQUID is capable of resolving changes in external magnetic field that approach 10^{-15} tesla, yet can be made to operate in fields as large as 7 tesla. The supercurrent flowing in a two Josephson junctions superconducting loop is related to the linked magnetic flux $\Phi(B)$ through the expression [112]

$$I \simeq cos(\pi \frac{\Phi(B)}{\Phi_0}) \quad , \tag{3.1}$$

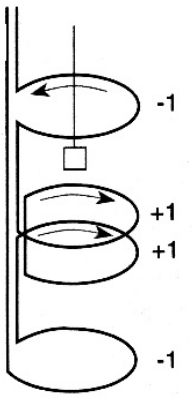

Figure 3.2: Detection coil. A gradiometer configuration is used to reduce noise in the detection circuit caused by fluctuations in the large magnetic field of the superconductive magnet.

where $\Phi_0 = 2.07 \cdot 10^{-7}$ G·cm^2 is the flux quantum, giving the period of current oscillations. Thus, from the detection of the current I it is possible to deduce the magnetic flux on the circuit, with resolution smaller than the flux quantum Φ_0. Although the SQUID is the source of the instrument sensitivity, it does not detect directly the magnetic field from the sample. Instead, the sample moves through a system of superconducting detection coils inductively coupled to the SQUID. Any change in the magnetic flux in the detection coil induces a proportional change in the persistent current in the detection circuit. Since the SQUID functions as a highly linear current-to-voltage convertor, the variations in the current produce corresponding variations in the SQUID output voltage, which are proportional to the magnetic moment of the sample. The sample is mounted in a sample holder that is attached to the end of a rigid sample road. The sample road enters the sample space through a special type of double seal designed to allow the rod to be actuated by a drive mechanism located outside of the chamber. The top of the sample transport road is attached to a stepper-motor-controlled platform which is used to drive the sample through the detection coil in a series of discrete steps. The detection coil is a single piece of SC wire wound in a set of three coils configured as a second-order (second-derivative) gradiometer, positioned at the center of the SC magnet. In this configuration, the upper coil is a single turn wound clockwise, the center coil comprises two turns wound counter-clockwise and the bottom coil is a single turn wound clockwise. The gradiometer configuration is used to minimized background drifts in the SQUID detection system caused by relaxation in the magnetic field of the SC magnet. In fact, if the magnetic field is relaxing uniformly, ideally the flux change in the two-turn center coil will be exactly canceled by the flux change in the single-turn top and bottom coils. On the other hand, the magnetic moment of a sample can be measured by moving the

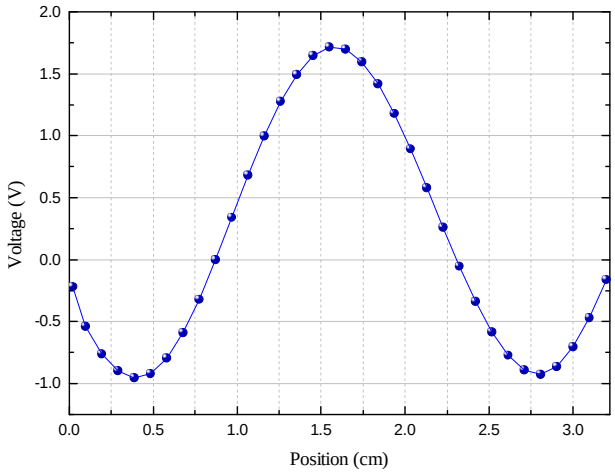

Figure 3.3: Typical shape of the output voltage in function of the relative position sample-detection coil. The solid line represents the best fit of the theoretical signal of a dipole moving through a second-order gradiometer.

sample through the detection coil because the counterwound coil set measures the local changes in magnetic flux density produced by the dipole field of the sample.

The whole apparatus is placed inside a highly insulating chamber filled with liquid helium in order to assure the superconductivity of the circuit (Fig. 3.1). Instead, the sample space is thermally isolated from the rest of the system and maintained at low pressure with static helium gas. At the top of the sample space an airlock can be evacuated and purged with clean helium gas, boil-off from the liquid helium bath in the dewar. Two thermometers determine the sample temperature and provide for temperature control.

3.1.2 DC Magnetization Measurement

During a DC magnetization measurement the sample is stopped at a number of positions over the specified scan lenght and at each stop several readings of the SQUID voltage are collected and averaged. The complete scan can be repeated a number of times and the signals averaged to improve the signal-to-noise ratio. The currents induced in the detection coil are ideally those associated with the movement of a point-source magnetic dipole through a second-order gradiometer detection coil. The spatial dependence of the ideal sign is shown in Fig. (3.2). In order to analyze the SQUID output signal, the area under the SQUID voltage versus position curve is integrated, since it is proportional to the magnetic moment **M**. The sample must be well centered in the detection coil and fairly long scan length are required to get accurate results. Alternatively, the sample magnetization can be derived from a fit of the theoretical signal of a dipole moving through a second-order gradiometer to the actual SQUID output signal using a linear regression algorithm. A scan

short as 2 cm can be used now, but the sample must remain well centered as well.

3.1.3 AC Susceptibility Measurement

A standard measurement of the AC susceptibility is a two-point measurement that positions the sample in two locations within the SQUID detection coil and measures the effect of a "nulling" waveform on the sample's magnetic moment at each location, canceling all spurious signals at the AC measurement frequency. In the first part of the measurement the sample transport positions the sample in the center of the positively oriented, bottom SQUID detection coil and then the system applies an oscillating AC magnetic field to the sample. The AC SQUID response is monitored and the nulling waveform, which will cancel the AC response, is calculated. The nulling waveform is injected into the SQUID feedback circuitry and the AC SQUID response is recorded. The iterative calculation of the nulling waveform continues until the amplitude of the wave iteration is smaller than the null amplitude level, the regression fit is less than 0.001 or the number of iteration exceeds 20. Once drive nulling is complete, MPMS system measures the remnant signal M_b in the bottom detection coil. The data is fit to the equation

$$M_b = A + Bt + M'cos(\omega t) + M''sin(\omega t) \quad , \tag{3.2}$$

where A is any remaining DC offset, B term originates from the linear drift in the field or temperature, ω is the angular frequency of the AC drive signal and M' and M'' are proportional to that part of the in-phase and out-of-phase components that has not been completely removed from the measurement by the drive-nulling procedure. In the second part of the two-point measurement, the sample transport positions the sample in the center of the two middle, negatively oriented detection coils. The AC drive signal and nulling waveform last used are applied. The nulling waveform still cancels the signal generated by the gradiometer imbalance, while the AC signal generated by the sample changes polarity when moved to the middle coils. Thus, the component of the nulling waveform that nulled the sample response in the bottom coil now adds constructively to the sample signal. The twin loops of the middle coils and the added signal of the nulling waveform create an AC susceptibility sine wave that has a triple amplitude. Then the system measures the remnant signal M_c in the middle coils and fits again the data into Eq. (3.2). Each component of susceptibility is finally calculated from the difference between the two measurements:

$$M = N\frac{M_c - M_b}{f(c) - f(b)} \quad , \tag{3.3}$$

where N is an overall normalization factor for the amplitude of the moment and $f(x)$ represents the normalized response function of the magnetometer to

an idealized dipole at position x along the the central axis of the gradiometer. Any residual signal caused by imperfect nulling of the gradiometer imbalance is the same in both positions and is therefore removed from the data. The number of measurement to average can be chosen by the user.

3.2 Static Uniform Susceptibility of $[Pc_2\mathbf{Tb}]^-\mathbf{TBA}^+ \times n[\mathbf{TBA}]\mathbf{Br}$

The samples under examination are characterized by molar ratios $[Pc_2\mathrm{Tb}]^-/\mathrm{TBA}^+$ of $1 \div 10$ and $1 \div 144$ respectively. The temperature dependence of DC magnetization **M** was measured for both samples in a static applied magnetic field H = 0.45 T and in the temperature range 3 - 320 K. The experiment was performed three times, by adopting different cooling procedures. First, the system was cooled down from room temperature to 3 K in an external field H = 5 T, at the rate of 10 K/min. Then, the cooling rate was decreased to 1 K/min keeping the same field of 5 T. Finally, the cooling was performed in zero-field (ZF) at the rate of 1 K /min. Since the magnetization depends linearly on the

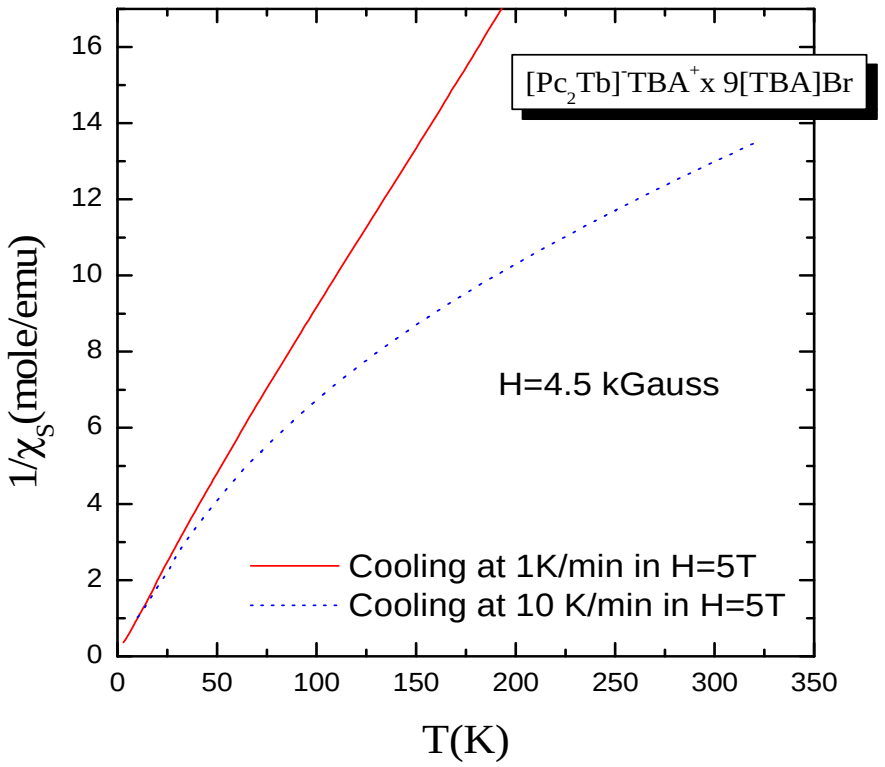

Figure 3.4: Temperature dependence of the inverse of static molar susceptibility χ_S^{-1} for $[Pc_2\mathrm{Tb}]^-\mathrm{TBA}^+ \times 9[\mathrm{TBA}]\mathrm{Br}$ compound. The two curves were obtained after different cooling procedures (1 K/min cooling rate, solid line, and 10 K/min cooling rate, dotted line).

external field in the explored range of temperature and for such values of the applied fields, the static molar susceptibility is given by

$$\chi_S = \frac{M}{H}\frac{p_{mol}}{p} \quad , \tag{3.4}$$

where p and p_{mol} are, respectively, the sample weight and the molar weight of the compound. The experimental behaviour of χ_S^{-1}, obtained for different cooling rates, is reported for $[Pc_2\text{Tb}]^-\text{TBA}^+ \times 9[\text{TBA}]\text{Br}$ in Fig. (3.4). The two trends are remarkably different, suggesting that the final disposition of the TBA groups around the Pc_2Tb molecules depends in a crucial way on the cooling rate. In fact, since the crystal field on the rare-earth ion is strongly influenced by the TBA arrangement, in turn the magnetic properties of the system are much influenced by the cooling process. This result points out the importance in the choice of the cooling procedure, which must be keep unchanged to assuring the reproducibility of the experiments. This effect only concerns diluted compounds, while magneto-thermic effects do not affect undiluted $[Pc_2\text{Tb}]^-\text{TBA}^+$ and neutral $[Pc_2\text{Ln}]^0$ complexes.

3.3 Static and Dynamic Susceptibility in Neutral $[Pc_2\text{Ln}]^0$

In the neutral $[Pc_2\text{Ln}]^0$ (Ln = Tb, Dy or Y) no special precaution in the cooling process was adopted. In fact, since the molecular packing does not allow for molecular motions at high temperatures, the crystalline structure, and thus the crystal field symmetry, do not depend on how fast the system is cooled down. In $[Pc_2\text{Tb}]^0$ the static, uniform susceptibility χ_S was determined in the temperature range 2 - 300 K in a static field H = 500 Gauss and even in the presence of an applied pressure. Susceptibility behaviour with T follows the Curie law

$$\chi_S(T) = \frac{g^2\mu_B^2 J(J+1)N_A}{3k_B T} \quad , \tag{3.5}$$

with Curie constant $C = g^2\mu_B^2 J(J+1)N_A/(3k_B) = 9.55 \pm 0.01$ erg·K/G^2. This value is consistent with a spin magnetic moment for the Tb^{3+} ion $\mu_{eff} = g\sqrt{J(J+1)} = 8.74\ \mu_B$, slightly smaller than the value $\mu_{eff} = 9.72\ \mu_B$ expected for a isolated Tb^{3+} ion. This result reflects the presence of a strong antiferromagnetic interaction between the lanthanide f electrons and the phthalocyaninato ligand radical electron. In fact, this antiferromagnetic coupling leads to a reduction of both the J value and the ion spin multiplicity of the free ion term, which is characterized by a ground state $^7F_6$ (symbol: $^{2S+1}F_J$). The new state that arises from the AF interaction with the unpaired electron is a $^6F_{11/2}$ state. The corresponding Landè g factor, given by

$$g = 1 + \frac{J(J+1) + S(S+1) - L(L+1)}{2J(J+1)} \quad , \tag{3.6}$$

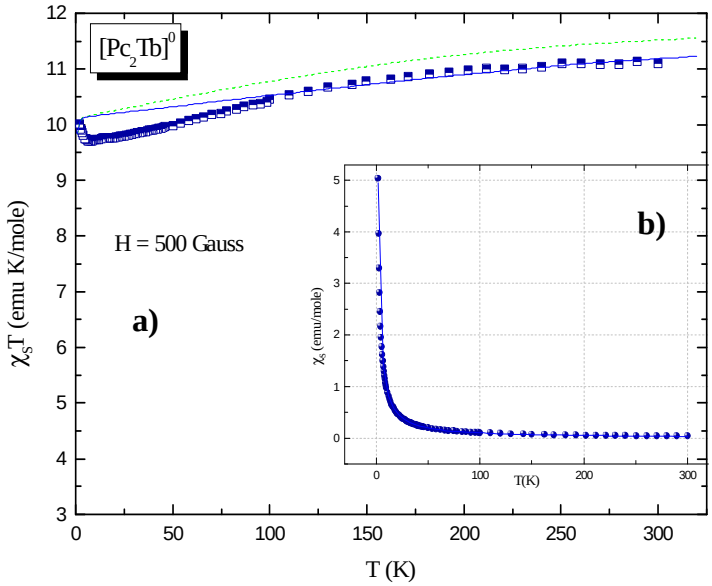

Figure 3.5: a) Temperature dependence of static molar susceptibility times T ($\chi_S T$) for neutral $[Pc_2\mathrm{Tb}]^0$ compound. Experimental data (squares) are plotted together with theoretical curves deduced assuming an energy barrier $\Delta = 880$ K (solid line) and the CF level splittings proposed by Ishikawa for $[Pc_2\mathrm{Tb}]^-\mathrm{TBA}^+$ in ref. [47](dotted line). b) Temperature dependence of static molar susceptibility, showing a Curie trend. The best fit to Eq. (3.5) (solid line) gives the value C = 9.87 ± 0.01 erg·K/G^2 for the Curie constant.

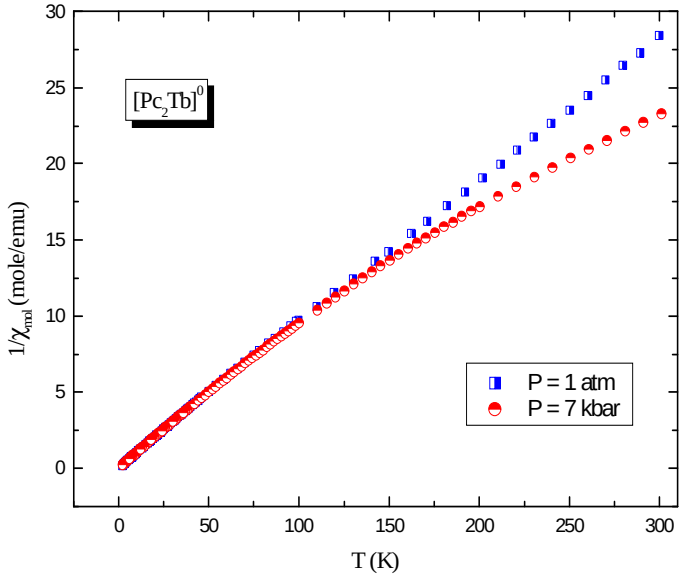

Figure 3.6: Temperature dependence of the inverse of static molar susceptibility χ_S^{-1} for neutral $[Pc_2\mathrm{Tb}]^0$ compound, under atmospheric pressure (blue squares) and under the applied pressure P = 7 kbar (red circles).

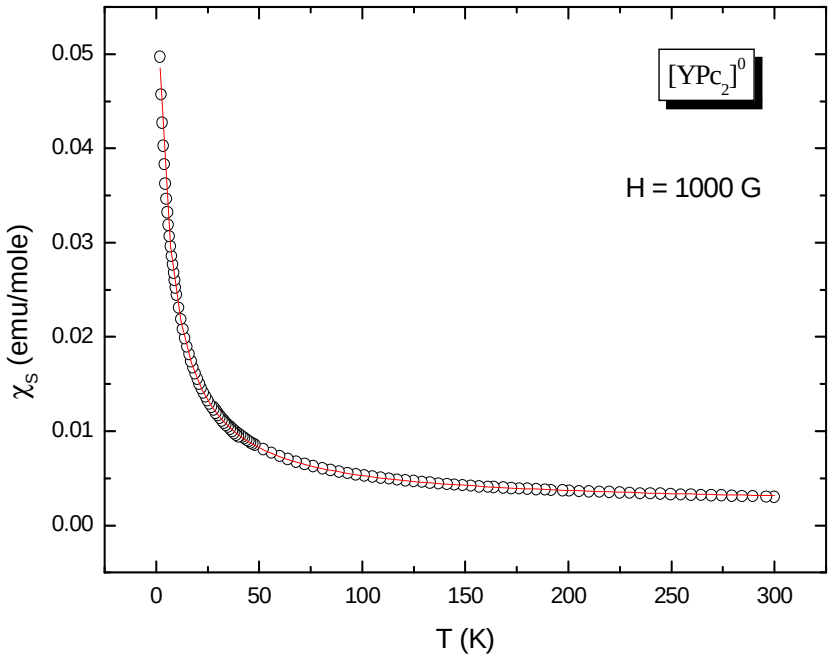

Figure 3.7: Temperature dependence of static uniform suceptibility χ_S for $[Pc_2\text{Y}]^0$ complex. χ_S follows the Curie-Waiss law with CW temperature $\theta \simeq$ -5.37 K and Curie constant $C \simeq 0.342$ erg K/G^2.

is g = 1.45 and the expected moment is $\mu_{eff} = 8.7\mu_B$. It must be noticed that in Pc_2Tb compound the crystal field anisotropy barrier is much larger with respect to the thermal energy k_BT in the investigated temperature range. Therefore, the Curie-law trend must be associated with the Zeeman splitting removing the degeneracy of the two lowest levels $J_z = \pm 6$. With respect to low T susceptibility trend, the system thus behaves as a two-level system with total angular moment J = 6 and components along the quantization axes $J_z = \pm 6$. The temperature dependence of $\chi_S T$ allows to derive an estimate for the energy gap which separates the lowest levels from the first excited states (see discussion). This gap was found to be remarkably larger with respect to the value estimated by Ishikawa *et al.* in the anionic form $[Pc_2\text{Tb}]^-\text{TBA}^+$, on the basis of crystal field calculations [47].

In $[Pc_2\text{Dy}]^0$ the susceptibility T dependence, measured in H = 1000 G, is well reproduced by a Curie law with C = 9.56 $\pm$ 0.02 erg·K/G^2, associated with a spin magnetic moment for the Dy^{3+} ion $\mu_{eff} = 8.74\ \mu_B$. This value is much smaller than that expected for the isolated Dy^{3+} ion ($\mu_{eff} = 10.65\ \mu_B$). In fact, the same considerations reported above about the AF coupling between lanthanide ion spin and the unpaired π electron are still valid. On the other hand, it must be remarked that in Dy complex, due to the crystal field the lowest substates are characterized as $J_z = \pm 13/2$, the second largest in the $J = 15/2$ ground state. Accordingly, the effective ion magnetic moment

becomes smaller in the double-decker structure with respect to the isolated ion. As it will be discussed in the next paragraph, the analysis of $\chi_S T$(T), allows for the determination of the low energy level structure of the Dy^{3+} ion spin multiplet $J = 15/2$.

In $[Pc_2Y]^0CH_2Cl_2$ complex, the behaviour of the static susceptibility with temperature is well reproduced by the Curie-Waiss (CW) law, with CW temperature $\theta \simeq$ -5.37 K, indicating the onset of antiferromagnetic correlations at low T (Fig. 3.7). Moreover, the application of an external pressure yields a modification in the behavior of susceptibility with T in both $[Pc_2Y]^0CH_2Cl_2$ and $[Pc_2Tb]^0$ complexes, suggesting the possibility to modify the overlap of π orbitals with pressure (Fig. 3.14-3.6). In $[Pc_2Y]^0CH_2Cl_2$, the strength of the AF interactions was found to vary with pressure, probably due to the increase in the π orbital overlap (see discussion), while in $[Pc_2Tb]^0$ further measurements are necessary to understand the observed changes in χ(T) induced by pressure.

In $[Pc_2Tb]^0$ and $[Pc_2Dy]^0$ complexes, in-phase ($M'-$ real) and out-of-phase ($M''-$imaginary) AC magnetization data were collected in H_{ac} = 4 G oscillating magnetic field at frequencies between 10 and 1488 Hz, in the 10-80 K temperature range and for different applied static fields (Fig. 3.8-3.9). The real ($\chi'(\omega) = \frac{M'(\omega)}{H_{ac}}$) and the imaginary ($\chi''(\omega) = \frac{M''(\omega)}{H_{ac}}$) components of susceptibility are given by

$$\chi'(\omega) = \chi_S + \frac{\chi_S - \chi_\infty}{1 + \omega^2\tau^2} \quad , \quad \chi''(\omega) = \frac{(\chi_S - \chi_\infty)\omega\tau}{1 + \omega^2\tau^2} \quad . \tag{3.7}$$

In Eq. (3.7), χ_S represents the susceptibility measured in the limit $\omega << \tau^{-1}$, e.g. static susceptibility, while χ_∞ is that found in the opposite limit $\omega >> \tau^{-1}$, where ω is larger than any characteristic frequency of the system under investigation.
In $[Pc_2Tb]^0$, a sharp drop in $\chi'T$ is observed on cooling in correspondence to a peak in χ''/χ_S, which progressively shifts to lower temperatures as the AC frequency is lowered (Fig. 3.8). As it will be discussed in Par. 3.4, this behaviour clearly indicates a progressive slowing down of the dynamics on cooling. Indeed, when the characteristic time associated to spin reversal matches the inverse of the irradiation field frequency, the absorbtion of the system becomes maximum, thus yielding a peak in the susceptibility imaginary part. In $[Pc_2Dy]^0$ analogous but slightly broader peaks are observed at lower temperature (Fig. 3.9), suggesting a faster dynamic. This is in fact what one should expect, since the CF splitting effect is much smaller in Dy complex and the typical magnetization relaxation times are thus shorter.

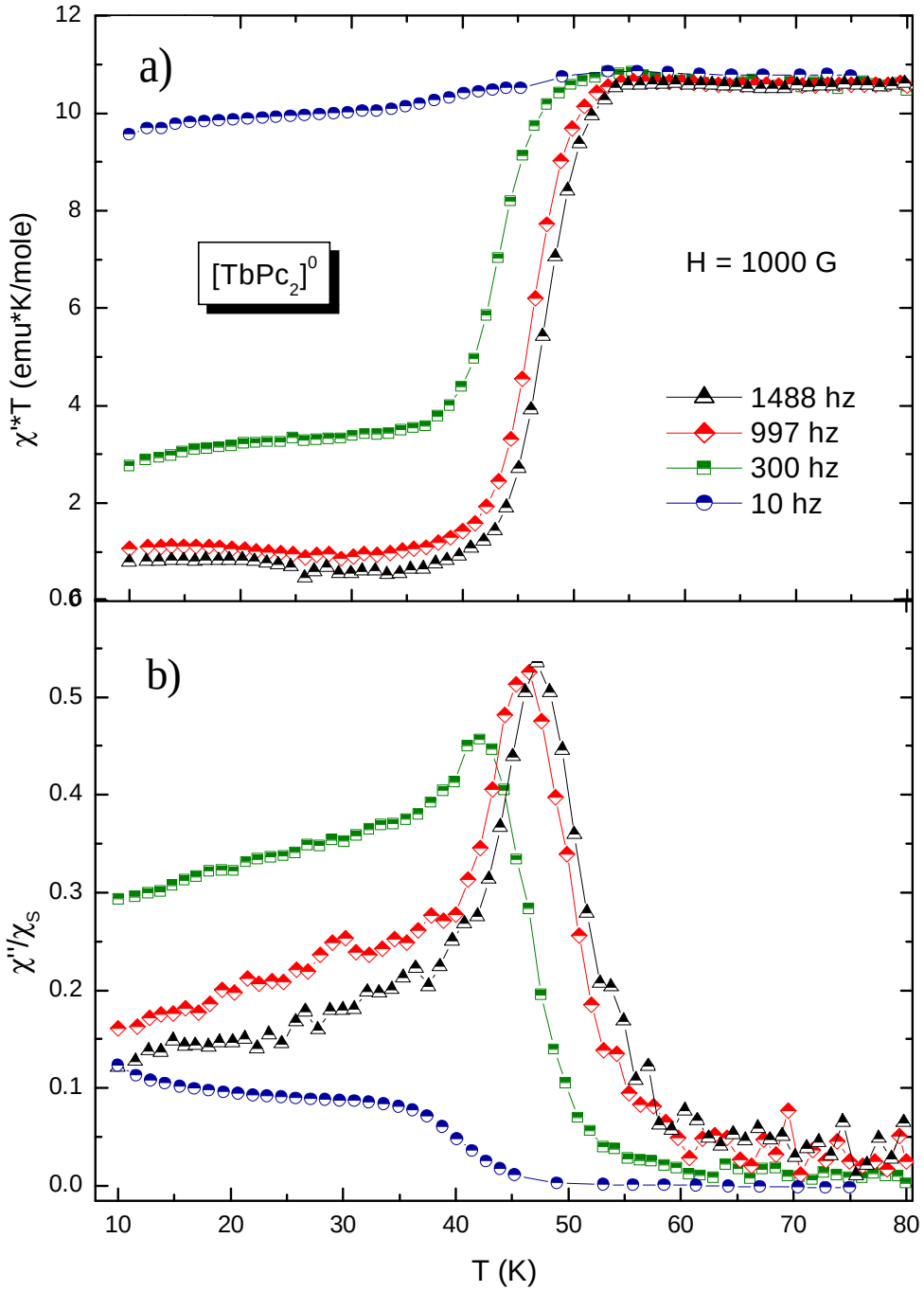

Figure 3.8: Temperature dependence of a) $\chi'T$ and b) χ''/χ_S in $[Pc_2\text{Tb}]^0$, where χ', χ'' and χ_S are in-phase-AC, out-of-phase-AC and DC molar magnetic susceptibilities, respectively. The measurements were performed in 4 G oscillating magnetic field at 10, 300, 997 and 1488 Hz, in the presence of a 1000 G DC component.

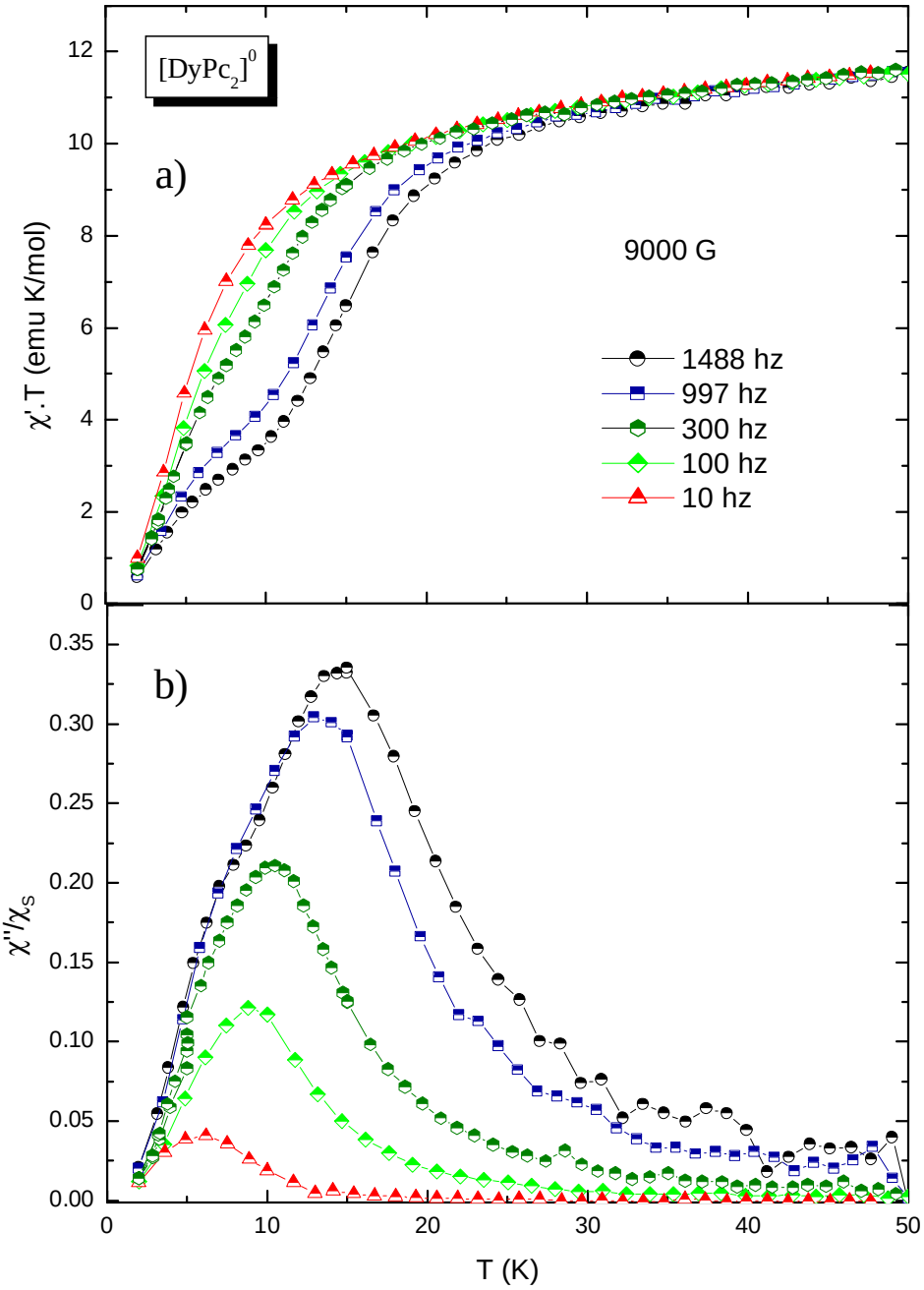

Figure 3.9: Temperature dependence of a) $\chi'T$ and b) χ''/χ_S in $[Pc_2\mathrm{Dy}]^0$. The measurements were performed in 4 G oscillating magnetic field at 10, 100, 300, 997 and 1488 Hz, in the presence of a 9000 G DC component.

3.4 Analysis of Results and Discussion

In diluted $[Pc_2\mathrm{Tb}]^-\mathrm{TBA}^+ \times n[\mathrm{TBA}]\mathrm{Br}$ complexes the static magnetic susceptibility was found to strongly depend on the magneto-thermic history of the sample, due to the presence of molecular motions at high temperature, that will be better defined through NMR spectra analysis reported in Chapter 5. High temperature molecular dynamics involve TBA^+ diamagnetic groups which play a fundamental role in the definition of the crystal field at the Tb^{3+} ion. Thus, since the cooling procedure determines the arrangement of TBA^+ molecules around the magnetic ion, it also gives an important contribute in the characterization of the magnetic properties of the system. For this reason, together with the difficulties in the precise evaluation of the diamagnetic contribution to χ_S coming from TBA^+ groups, it is quite hard to get information on the energy level structure of these systems from susceptibility analysis. On the contrary, in neutral $[Pc_2\mathrm{Ln}]^0$ powders magnetic properties do not depend on the cooling rate, then it is possible to estimate the energy gap to spin reversal and the low-energy level structure. Since the experiments were performed on powders, the molecules and the CF axis are randomly oriented with respect to the external field $\mathbf{H}||\hat{\mathbf{z}}$. Thus the total magnetization $\mathbf{M}$ can be deduced by summing the contributions of the molecules with the anisotropy axis perpendicular and parallel to $\hat{\mathbf{z}}$, namely $M(T) = \frac{2}{3}M_{x,y}(T) + \frac{1}{3}M_z(T)$, with

$$M_i(T) = N_A \frac{\sum_{k=-J}^{+J} \langle \mu_i^k \rangle \, e^{-\frac{E_i^k}{T}}}{\sum_{k=-J}^{+J} e^{-\frac{E_i^k}{T}}} \quad , \quad i = x, y, z \quad . \tag{3.8}$$

In Eq. (3.8), E_i^k represents the k-th eigenvalue of the hamiltonian:

$$\hat{\mathcal{H}} = \hat{\mathcal{H}}_{CF} + g\mu_B \hat{\mathbf{J}} \cdot \mathbf{H} \quad , \tag{3.9}$$

where $\hat{\mathcal{H}}_{CF}$ is the crystal field hamiltonian and $g\mu_B \hat{\mathbf{J}} \cdot \mathbf{H}$ is the Zeeman term. $\langle \mu_i^k \rangle$ is the expectation value of the i-th component of the magnetic moment over the k-th eigenstate of the hamiltonian. In Fig. (3.5), the temperature dependence of $\chi_S T$ for neutral $[Pc_2\mathrm{Tb}]^0$ compound is shown. Experimental data are compared to the theoretical curves derived from Eq. (3.8), by using different values for the CF levels. The dotted line is obtained by assuming the CF level splittings proposed by Ishikawa for $[Pc_2\mathrm{Tb}]^-\mathrm{TBA}^+$ in ref. [47]. Instead, the solid line simulates the $\chi_S T(T)$ of a system with an energy gap of 880 K, corresponding to the value obtained by means of microscopic techniques (see Chapter 5). The assumption of a higher barrier allows to reproduce better the experimental data. Nevertheless, the behaviour of χ_S with temperature crucially depends on the crystal field levels splittings only at very high T, since the energy barrier is much larger than the thermal energy in the investigated temperature range. Therefore it is not possible to derive further informations about higher levels.

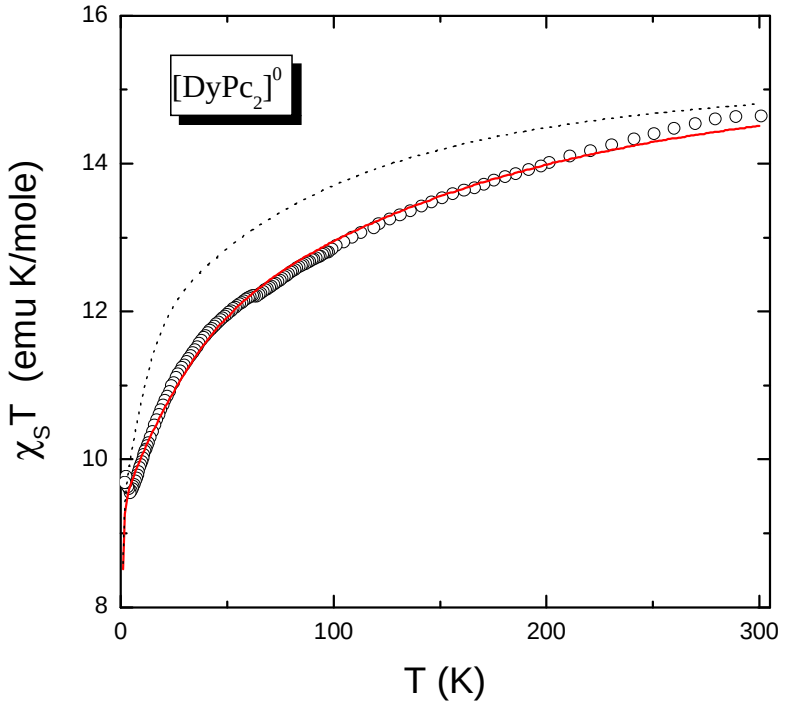

Figure 3.10: Temperature dependence of $\chi_S T$ in $[Pc_2\mathrm{Dy}]^0$ for H = 1000 Gauss (open circles) and the best fit to Eq.(3.8) (solid line). The dashed line corresponds to the behaviour calculated on the basis of $[Pc_2\mathrm{Dy}]^-\cdot\mathrm{TBA}^+$ CF splittings derived by Ishikawa *et al* in [47].

This is not the case for $[Pc_2\mathrm{Dy}]^0$ complex, where susceptibility analysis allows for the determination of the fundamental multiplet $J = 15/2$ sublevels structure. In order to analyze $\chi_S T(T)$ in $[Pc_2\mathrm{Dy}]^0$, we started again from the CF structure for the $J = 15/2$ ground-state multiplet initially derived by Ishikawa *et al.* for $[Pc_2\mathrm{Dy}]^-\mathrm{TBA}^+$ [47]. Then we varied the splitting among the levels until we found the best fit to the experimental data. Two sets of possible solutions were found to fit reasonably well $\chi_S T$ data. However, only one of them yielded a splitting between the lowest lying energy levels around 65 K, the value derived from AC susceptibility measurements (see later on). The estimated energy splittings are thus $\Delta_1 = 65$ K, corresponding to the separation between the $|m = \pm 13/2\rangle$ ground states and the $|m = \pm 9/2\rangle$ first excited levels, $\Delta_2 = 47$ K between the $|m = \pm 9/2\rangle$ levels and the $|m = \pm 11/2\rangle$ second excited levels and $\Delta_3 = 460$ K between the $|m = \pm 11/2\rangle$ levels and the $|m = \pm 15/2\rangle$ third excited levels. These values differ from the ones deduced for $[Pc_2\mathrm{Dy}]^-$ on the basis of crystal field calculations ($\Delta_1 \simeq 56$K, $\Delta_2 \simeq 196$K, $\Delta_3 \simeq 126$K)[47]. As it can be seen in Fig. (3.10), a good fit of the experimental data is found.
The estimate of Δ_1 is in excellent agreement with the value deduced from AC susceptibility measurements. In both $[Pc_2\mathrm{Dy}]^0$ and $[Pc_2\mathrm{Tb}]^0$ the maxima in

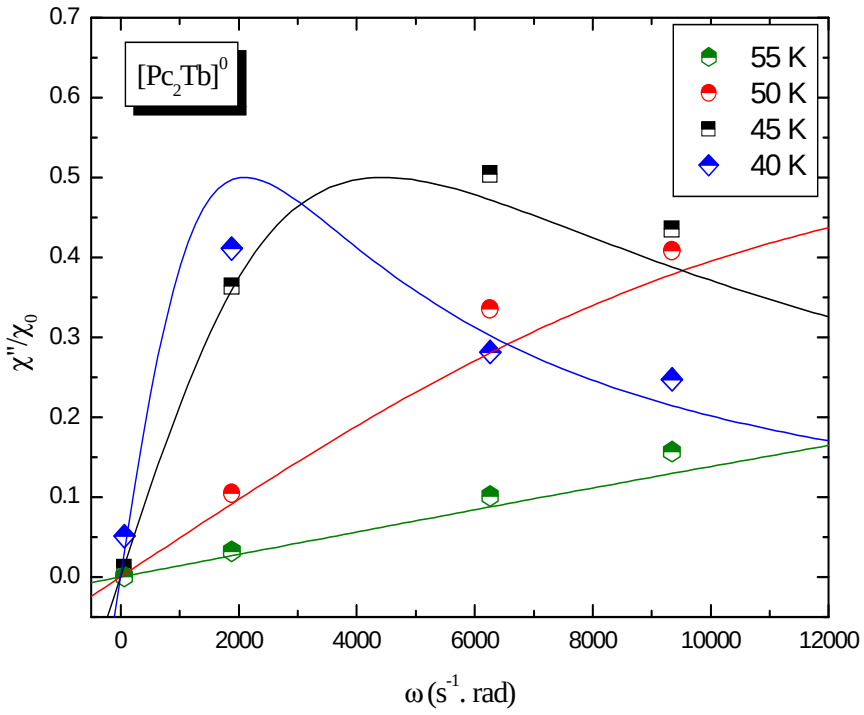

Figure 3.11: Angular frequency dependence of χ''/χ_S in $[Pc_2\mathrm{Tb}]^0$, measured for different temperatures. Solid lines represent theoretical curves derived according to Eq. (3.10).

χ''/χ_S shifting to lower temperature upon decreasing the irradiation frequency clearly indicate a progressive slowing down of the dynamics on cooling. In the case of a monodispersive dynamical relaxation mode, at the peak temperature (T_m) the bulk magnetization relaxation time $\tau_c(T_m)$ matches the inverse of the angular frequency ω of the applied oscillating field, according to the expression ($\chi_S \gg \chi_\infty$)

$$\chi''(\omega) = \frac{\chi_S \omega \tau_c}{1 + \omega^2 \tau_c^2} \quad . \tag{3.10}$$

The validity of this expression was checked by performing frequency scans at a fixed temperature. As can be seen in Fig. (3.11), the above expression is satisfied in the explored T range. The linear relation of $ln(\tau_c^{-1}(T_m))$ to 1/T (Fig. 3.12) indicates that the Orbach process is dominant in the high temperature range and that the Arrhenius law $\tau_c = \tau_0 exp(\Delta/T)$ for the correlation time is obeyed. From the fit of $[Pc_2\mathrm{Tb}]^0$ data in Fig. (3.12) one estimates a value for the energy barrier $\Delta = 750 \pm 35$ K, much larger than the one reported by Ishikawa *et al.* ($\Delta \simeq 590$ K) in the same nominal compound [49]. The fit of $[Pc_2\mathrm{Dy}]^0$ data in Fig. (3.12) gives a much smaller activation energy $\Delta = 64 \pm 2$ K, which corresponds quite well to the one obtained from the analysis of the static susceptibility data (Fig. 3.10), and provides an estimate for the separation among the lowest energy levels of $[Pc_2\mathrm{Dy}]^0$.

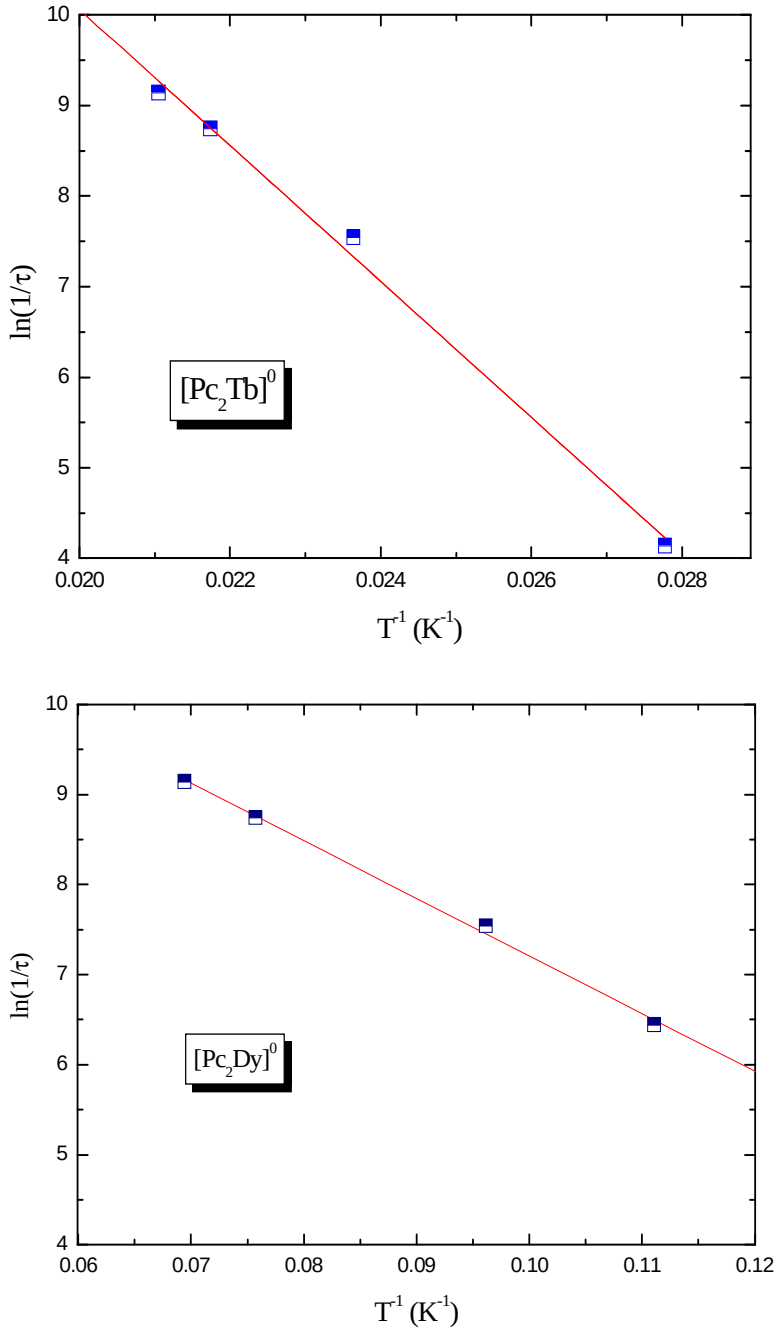

Figure 3.12: Natural logarithm of the spin correlation rate against the inverse of the χ''/χ_S peak temperature for $[Pc_2\text{Tb}]^0$ (H = 1000 Gauss) (top) and for $[Pc_2\text{Dy}]^0$ (H = 9000 Gauss) (bottom). The lines correspond to the best fits for an activated behaviour for a barrier $\Delta \simeq 750$ K for $[Pc_2\text{Tb}]^0$ and $\Delta \simeq 64$ K for $[Pc_2\text{Dy}]^0$.

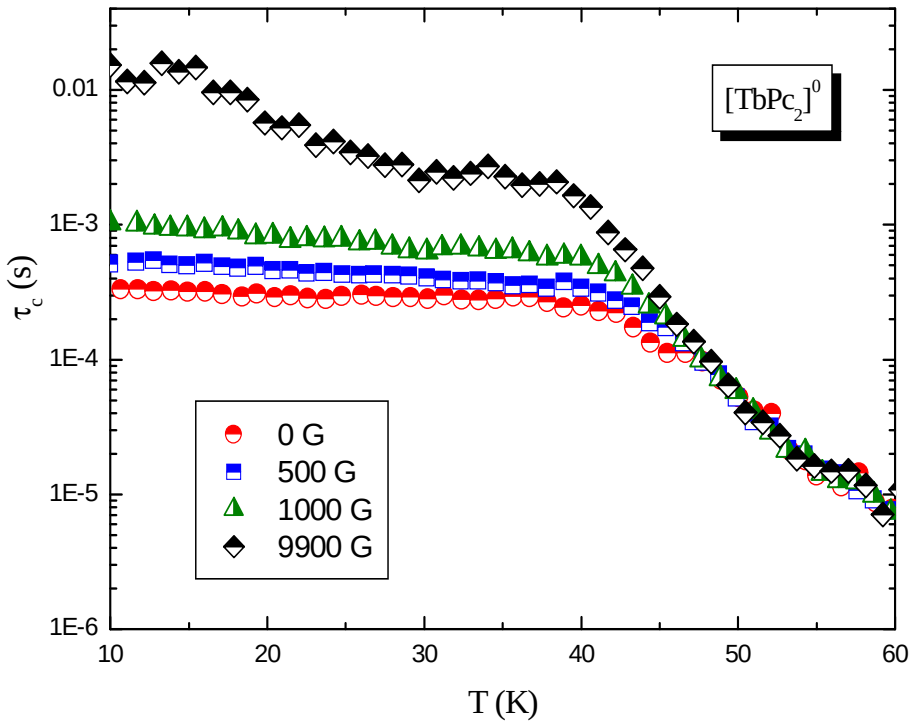

Figure 3.13: Temperature dependence of τ_c, deduced from Eq. (3.10) for a static field of 0, 500, 1000, 9900 Gauss in $[Pc_2\mathrm{Tb}]^0$.

From Eq. (3.10) the behaviour of τ_c as a function of T was derived (Fig. 3.13). The high T activated trend can be evidenced only in the 45-60 K range from AC susceptibility data, due to the too low signal-to-noise ratio in χ''/χ_S vs T plot at higher temperatures. Below T = 45 K a plateau associated with tunneling processes among the $|m = \pm 6\rangle$ low-energy levels is present. In this region the magnetization correlation time is temperature independent since the crystal field levels broadening associated with their finite lifetimes yields a partial overlapping of the lowest levels themselves. However, it is noticed that the plateau lies at different values depending on the magnitude of the applied field. In fact, the external magnetic field leads to a Zeeman splitting of the two-fold degenerate ground state, which is proportional to the field intensity, $\Delta E_{Zee} = 12 g \mu_B \mathbf{J} \cdot \mathbf{H}$. This splitting inhibits the the tunneling transitions between the lowest levels and, consequently, causes a reduction of the tunneling rate.

$[Pc_2\mathrm{Y}]^0$ complex can be described as a chain of spin-1/2 radicals involving a doubly degenerate orbital. Indeed, yttrium is a non-magnetic atom with closed-shell configuration and the unpaired electron of a $[Pc^- Pc^{2-}]$ mixed-valence pair occupies indistinctly both macrocyclic Pc rings with equal energy. Thus, considering also the spin degeneracy, it results that the multiplicity relative to each radical is 4 and that for a chain of N radicals is 4^N. Moreover, Pc molecules are stacked one above the other, with a staggered angle of 45° which

entails orthogonality of magnetic orbitals. Therefore Pc_2Y molecule obeys to the D_{4d} point-group symmetries. On the other hand, the stacking of Pc_2Y molecules differs in the solvated $[Pc_2Y]\cdot CH_2Cl_2$ and nonsolvated α-Pc_2Y, while intramolecular distances remain the same [113]. Thus, the D_{4d} point group is maintained for the nonsolvated species, while the full symmetry is lowered for the solvated one. Accordingly, the interaction between adjacent radicals along the chain is expected to result from competing mechanism, depending on the relative position of magnetic orbitals in both complexes. A significant overlap of π orbitals should promote antiferromagnetic interactions, while orbital degeneracy should stabilize ferromagnetism [113]. It has been demonstrated that in the presence of orbital degeneracies the Heisemberg model is no longer valid and the exchange hamiltonian must be written [114]

$$\hat{\mathcal{H}}_{exch} = \sum_{m,m',n,n'} [b_{mm'}b_{m'm}/U(S_i,S_j)]C^*_{ms}|S_i\rangle\langle S_i|C_{nt}C_{m's}|S_j\rangle\langle S_j|C^*_{n't} + \hat{\mathcal{H}}_{sym} \quad , \tag{3.11}$$

where $\hat{\mathcal{H}}_{sym}$ stands for the symmetrical part of $\hat{\mathcal{H}}_{exch}$ obtained by interchanging i and j subscripts. In the case of $[Pc^- - Pc^{2-}]$ radical and for an infinite chain the actual exchange hamiltonian can be expressed as [113]

$$\hat{\mathcal{H}}_{exch} = -\sum_i [J\mathbf{S_i}\cdot\mathbf{S_{i+1}} + J'\mathbf{L_i}\cdot\mathbf{L_{i+1}} + J''\mathbf{L_i}\cdot\mathbf{S_i} + 2(J+J')\mathbf{S_i}\cdot\mathbf{S_{i+1}}\mathbf{L_i}\cdot\mathbf{L_{i+1}}] \quad , \tag{3.12}$$

where i runs over radical species, J and J' are the exchange constants along parallel chains and J'', referring to the spin-orbit coupling, is the interaction along rungs. Since J may be positive or negative, while J' may only be negative[113], it follows that several attractive situations may be encountered, from 1D ferromagnetism to 1D antiferromagnetism, depending on the sign of the exchange pathways. It has been demonstrated that $[Pc_2Y]^0$ contains either FM or AF chains, depending on whether the crystallization solvent CH_2Cl_2 is present or not.

In the solvated, neutral $[Pc_2Y]^0CH_2Cl_2$, static susceptibility follows Curie-Waiss law

$$\chi_S(T) = \frac{C}{T-\theta} \quad , \tag{3.13}$$

with an antiferromagnetic C-W temperature $\theta = -5.37 \pm 0.04$ K. The estimated Curie constant $C = g^2\mu_B^2 S(S+1)N_A/(3k_B) = 0.342 \pm 0.002$ erg·K/G^2 is close to the value 0.375 erg·K/G^2, expected for a spin-1/2 AF (Fig. 3.7). This result indicates the presence of a significant overlap of π orbitals, that favours AF interactions. Susceptibility measurement under pressure were performed in order to investigate how changes in the molecular packing can eventually modify orbital overlap and thus the nature of magnetic interactions. The external pressure seems to yield a reduction in the AF interactions. In fact, the C-W temperature reaches the value $\theta \simeq -2.8$ K already at the pressure P = 1.5 kbar (Fig. 3.14).

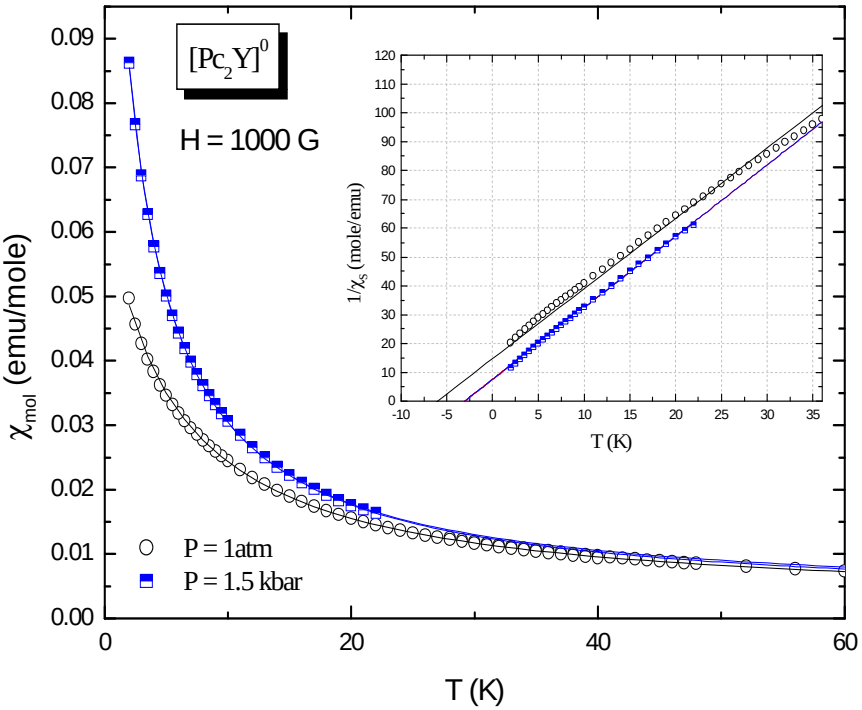

Figure 3.14: Temperature dependence of static molar susceptibility χ_S for neutral $[Pc_2\mathrm{Y}]^0\mathrm{CH_2Cl_2}$ compound, under atmospheric pressure (open circles) and under the applied pressure P = 1.5 kbar (blue squares). In the inset, linear fits of χ_S^{-1} evidence the variation of the C-W temperature by applying a pressure, from $\theta \simeq 5.37$ K to $\theta \simeq -2.8$ K.

Chapter 4

NMR and μSR Techniques

4.1 Nuclear Magnetic Resonance

The Nuclear Magnetic Resonance (NMR) is a powerful technique to investigate the local dynamics of a system. In fact, the nuclei are microscopic probes able to sense the fluctuations of local fields induced by the external environment, the *lattice*, which comprises the electrons, the neighbouring nuclei, the ionic charge distribution, etc.. Hence, the NMR technique allows to describe the static and dynamic properties of the ground state of the Pc_2Ln-based molecular magnets through the study of the interactions between the electronic spins and the nuclei. In particular, interesting information about the fluctuations of the electronic magnetization along the anisotropy axis were derived starting from the analysis of the spin-lattice relaxation times T_1. Indeed, as it will be shown in this chapter, the relaxation rate $1/T_1$ is proportional to the spectral density associated with the spin fluctuations, and it thus allows for the study of the low-frequency spin excitation of the system under investigation. In the following, a brief description of the NMR technique is presented.

4.1.1 Time Evolution of Nuclear Magnetization in the Presence of Magnetic Fields

The NMR signal is generated by the nuclear magnetization $\mathbf{M}$, which needs an applied magnetic field $\mathbf{H}_0$=$H_0\hat{\mathbf{z}}$ to be produced. The time evolution of the magnetization in the laboratory frame of reference (Σ_{xyz}) can be deduced from a classical approach, solving the equation [117]

$$\frac{d\mathbf{M}}{dt} = \gamma \mathbf{M} \wedge \mathbf{H_0} \quad , \tag{4.1}$$

which gives

$$M_z(t) = cost; \quad M_x(t) = M_\perp \cos(\gamma H_0 t); \quad M_y(t) = -M_\perp \sin(\gamma H_0 t) \quad , \tag{4.2}$$

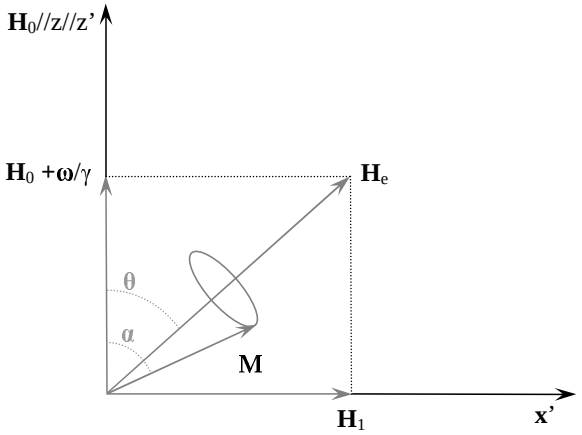

Figure 4.1: Sketch of the time evolution of $\mathbf{M}$ in $\Sigma'_{x'y'z'}$. The magnetization precesses around an effective field H_e which coincides with $\mathbf{H}_1$ if $\omega = \omega_0$.

for the three components of $\mathbf{M}$. Thus, as an effect of the external magnetic field, the nuclear magnetization $\mathbf{M}$ precesses around $\mathbf{H}_0$ at the Larmor frequency $\omega_0 = \gamma\mathbf{H_0}$. In order to analyze the time evolution of $\mathbf{M}$ due to the interactions with the lattice, it is useful to introduce a new frame of reference, $\Sigma'_{x'y'z'}$, rotating around $\mathbf{H}_0$ at a frequency $\omega = \omega_0$. In fact, such a frame of reference allows to get rid of the effect of $\mathbf{H}_0$ on the time evolution of $\mathbf{M}$. Now, if one adds the effect of a radio frequency (rf) field $\mathbf{H}_1$ rotating in a the plain xy at frequency ω, clockwise, in the frame of reference Σ' the magnetic moment will precess around the effective field (see Fig. 4.1)

$$\mathbf{H_e} = (H_0 - \frac{\omega}{\gamma})\hat{\mathbf{z}}' + H_1\hat{\mathbf{x}}' \quad . \tag{4.3}$$

Therefore, in the resonance condition $\omega = \omega_0$, $\mathbf{M}$ precesses around $\mathbf{H}_1$ at a frequency $\omega_1 = \gamma\mathbf{H_1}$. Thus, through the rf field $\mathbf{H}_1$ it is possible to tilt the nuclear magnetization, which is initially along the $\hat{\mathbf{z}}$ axis, in the xy plane. In fact, the angle α formed by $\mathbf{M}$ with the $\hat{\mathbf{z}}$ axis changes with time according to

$$\cos(\alpha(t)) = 1 - 2\sin^2\theta\sin^2(\frac{\omega_1 t}{2}) \quad , \tag{4.4}$$

which in the resonance condition becomes

$$\cos(\alpha(t)) = \cos(\omega_1 t) \quad . \tag{4.5}$$

Consequently, every time the condition $t = (2n+1)\frac{\pi}{2\omega_1}$ is verified, we have $\alpha = 90°$ and $\mathbf{M}$ lies in the xy plane.

On the other hand, the same physical results derived from a classical point of view can be obtained by means of the quantum mechanics formalism. For the sake of simplicity, consider that the ensamble of nuclear spins is characterized by a unique quantum number I = 1/2. In the presence of a static field $\mathbf{H}_0$

along z and of a rf field $H_1(t) = H_1 e^{i\omega_0 t}$ rotating in the xy plane at the Larmor frequency, the hamiltonian of the system can be write

$$\hat{\mathcal{H}} = -\gamma\hbar\hat{\mathbf{I}} \cdot \mathbf{H_0} - \gamma\hbar\hat{\mathbf{I}} \cdot \mathbf{H_1}(t) \quad . \tag{4.6}$$

The expectation values of the three components of $\hat{\mathbf{I}}$ can be calculated on the wavefunction solving the Schrodinger equation associated with the hamiltonian 4.6. Thus one obtains [118]:

$$\langle I_z(t)\rangle = -\frac{1}{2}\cos(\omega_1 t) \tag{4.7}$$

$$\langle I_x(t)\rangle = \frac{1}{2}\sin(\omega_1 t)\cos(\omega_0 t) \tag{4.8}$$

$$\langle I_y(t)\rangle = -\frac{1}{2}\sin(\omega_1 t)\sin(\omega_0 t) \quad . \tag{4.9}$$

Moreover, since we are dealing with an ensamble of nuclear spins we have to consider the statistical average given by [118]

$$\langle\overline{I_{x,y,z}}\rangle = \sum_{m=-1/2}^{+1/2} \langle m|I_{x,y,z}|m\rangle \frac{e^{-E_m/k_B T}}{Z} \quad , \tag{4.10}$$

with $|m\rangle$ and E_m eigenstates and eigenvalues, respectively, of $\hat{\mathcal{H}}$. By solving Eq. (4.10), analogous results of Eq. (4.7 - 4.9) can be derived [119]. In particular, in the rotating frame of reference Σ' we have

$$\langle\overline{I_z(t)}\rangle \propto \langle\overline{M_z(t)}\rangle = M_0\cos(\omega_1 t) \tag{4.11}$$

where M_0 is the maximum value of the component z of magnetization, and

$$\langle\overline{I_{x,y}(t)}\rangle \propto \langle\overline{M_{x,y}(t)}\rangle = \pm\frac{1}{2}M_\perp\sin(\omega_1 t) \quad . \tag{4.12}$$

Since even a small perturbation can tilt the magnetization on the xy plane ($\omega_1 \gg |\omega - \omega_0|$), in general we have $H_1 \ll H_0$. Thus, the term associated with H_1 in Eq. (4.6) can be treated as a perturbation of the Zeeman term $\hat{\mathcal{H}}_0 = -\gamma\hbar\hat{\mathbf{I}} \cdot \mathbf{H_0}$. At the equilibrium, the statistical population $N_\pm$ of the two Zeeman levels of energy $E_\pm = \pm\gamma\hbar H_0/2$ is characterized by an exponential growth $N_\pm \sim exp(-E_\pm/k_B T)$ and the spin temperature T_S equals the bath temperature T. When the resonance condition is satisfied, the field H_1 has the effect of inducing magnetic dipole transitions between the two spin levels. The statistical populations of the levels is thus modified and the system is brought out of equilibrium, with $T \neq T_S$ ($T_S = \infty$ when $N_+ = N_-$). From Eq. (4.11), the probability to flip a spin from $|m = +1/2\rangle$ to $|m = -1/2\rangle$ can be calculated, yielding to the Rabi equation

$$p_-(t) = \frac{1 - 2\langle\overline{I_z(t)}\rangle}{2} = \sin^2(\frac{\omega_1 t}{2}) \quad . \tag{4.13}$$

Thus, by irradiating the system with an rf field at frequency ω_0 it is possible to tilt the nuclear magnetization at the desired angle with respect to the z axis, varying the length of the applied pulses.

However, when all the hyperfine interactions present in a sample are considered, the solution for the time evolution of $\langle\overline{M_{x,y}(t)}\rangle$ can be quite complicated. Therefore, it is convenient to consider the phenomenological *Bloch equations* given by the following relations [120]:

$$\frac{dM_z}{dt} = \gamma(\mathbf{M} \wedge \mathbf{H_0})_z + \frac{M_0 - M_z}{T_1} \quad , \tag{4.14}$$

$$\frac{dM_{x,y}}{dt} = \gamma(\mathbf{M} \wedge \mathbf{H_0})_{x,y} - \frac{M_{x,y}}{T_2} \quad . \tag{4.15}$$

In Eq. (4.14) and (4.15) T_1 and T_2 are phenomenological quantities, describing how fast the equilibrium conditions are restored. In particular, the so-called *spin-lattice relaxation time* T_1 describes the time evolution of M_z and it is thus related to the modifications in the populations of the Zeeman levels. The transition between the spin levels can occur after the exchange of energy with the lattice excitations, thus T_1 measurements can give information on the low-frequency electronic spin excitations. On the other hand, the *spin-spin relaxation time* T_2 describes the decay of $M_{x,y}$ with time, mainly due to processes which do not imply an exchange of energy with lattice excitations, such as nuclear dipole-dipole interactions or inhomogeneities in the local magnetic fields. In fact, due to such processes each spin probes a field slightly different from its surrounding spins and precedes at a frequency slightly different from them.

As already mentioned, by means of pulsed NMR it is possible to detect the signal generated by the time evolution of nuclear magnetization in a frame of reference rotating at ω_0. In practice, the rotating field is obtained through an electrical alternate current at radio frequency flowing within a coil, oriented for example along x. The resulting oscillating field can be considered as the superimposition of two fields rotating clockwise and anticlockwise, respectively. However, when the resonance condition is fulfilled one can consider only the component of the rf field which is in phase with the magnetization precessional motion, since the other component does not affect the time evolution of $\mathbf{M}$. If the pulse length is $\tau = (\pi/2)(1/\gamma H_1)$ (for short, "$\pi/2$ pulse"), the nuclear magnetization is rotated by an angle $\pi/2$. If $\tau = \pi(1/\gamma H_1)$, instead, the magnetization rotates of an angle π (named "π pulse"). The xy components of the magnetization precessing after τ produce the so-called FID (Free Induction Decay) signal $G(t)$, which is detected by the same coil generating the rf field. In fact, the voltage $\mathcal{E}$ induced in the coil by the time evolution of the nuclear magnetization, according to Faraday-Maxwell's law, is proportional to the precessional frequency in the laboratory frame of reference and to the nuclear in-plane magnetization M_{xy}, according to the following equation:

$$\mathcal{E} = -\frac{1}{c}\frac{d\Phi}{dt} = -\omega_0 K M_{xy}(t) \quad , \tag{4.16}$$

where $d\Phi/dt$ is the flux variation induced in the coil by $M_{xy}(t)$. The signal detected by the coil in Σ can be transformed into the one in Σ' by mixing it with a reference signal oscillating at ω_0.

It can be shown that the FID signal G(t) is related with the in-plane component of the magnetization trough the expression [118]

$$G(t) = Tr\{M_x(t)M_x(0)\} \quad , \tag{4.17}$$

with

$$M_x(t) = e^{i\hat{\mathcal{H}}_P t/\hbar} M_x(0)\, e^{-i\hat{\mathcal{H}}_P t/\hbar} \quad . \tag{4.18}$$

The hamiltonian $\hat{\mathcal{H}}_P \ll \hat{\mathcal{H}}_0$ in Eq. (4.18), governing the time evolution of M_x, comprises all the other magnetic interactions involving the nuclear spins.

From the Bloch equations it is easy to derive the time evolution of $\mathbf{M}$ after $\mathbf{H}_1$ is switched off:

$$M_z(\tau) = M_{eq}(1 - \exp(-\frac{\tau}{T_1})) \quad , \tag{4.19}$$

or, analogously,

$$y(\tau) \doteq \frac{M_{eq} - M_z(\tau)}{M_{eq}} = \exp(-\frac{\tau}{T_1}) \quad , \tag{4.20}$$

and

$$M_{xy}(\tau) = M_\perp \exp(-\frac{\tau}{T_2}) \quad , \tag{4.21}$$

where $M_\perp$ is the initial value of the magnetization in xy plane. Depending on which relaxation time one is interested in, different pulse sequences can be used in pulsed NMR.

4.1.2 NMR Typical Sequences for T_1 and T_2 Measurements

A possible way to measure the T_2 relaxation time is to apply to the sample a $\pi/2$ pulse in phase with the coordinate axis x' of the rotating frame Σ'. Thus, the nuclear magnetization, initially parallel to the z≡ z' axis, is directed along the y' axis when the coil starts to work as a receiver (t = 0). The FID signal, decaying to zero with a characteristic time called T_2^*, can thus be recorded. The time T_2^* comprises both intrinsic and extrinsic effects, as magnetic field inhomogeneities associated with a distribution of paramagnetic shifts or just with the inhomogeneity of the external magnetic field over the sample volume. Since one usually is interested in the intrinsic decay of the NMR signal, it is convenient to resort to the *Hahn Sequence*, or *Spin Echoes technique*. In this sequence, after a time delay τ, a second pulse along x' or y' of length π is applied. The effects of the π pulse is to reverse the time evolution of the in-plane components of the nuclear magnetization (see Fig. 4.2). Therefore, the

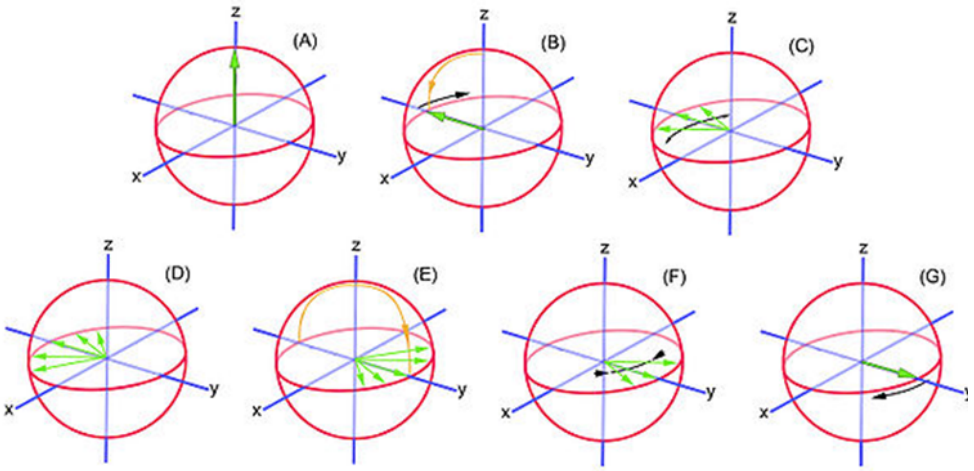

Figure 4.2: Sketch of the Hahn Sequence. In (E) a π pulse is applied. It enables to phase different components of the nuclear magnetization after a 2τ delay.

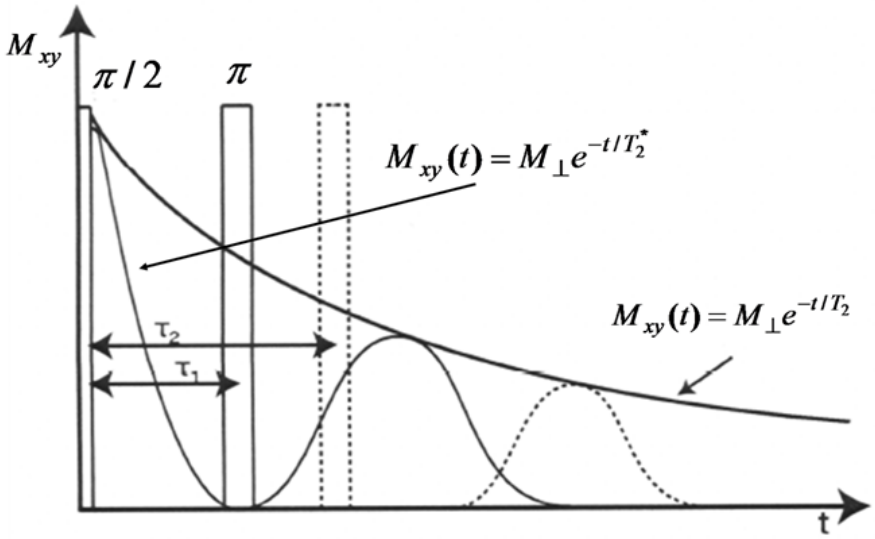

Figure 4.3: Typical sequence used to determine the spin-spin relaxation time.

dephasing of the spins during the first half of the sequence [0 - τ] is recovered in the second half, after the π pulse. The nuclear magnetization is then reconstructed after the time 2τ, but it is weakened by a factor exp(-$2\tau/T_2$) due only to the intrinsic spin-spin interactions. Reconstructing the echo for different τ values, T_2 can be derived.
To measure the T_1 relaxation time, the *saturation sequence* $(\pi/2)_{sat}$ - τ - $\pi/2$ - τ_{echo} is usually employed. $(\pi/2)_{sat}$ represents a train of pulses separated by a time τ_{sat} with $T_2 \ll \tau_{sat} \ll T_1$. It is used to cancel the z component of

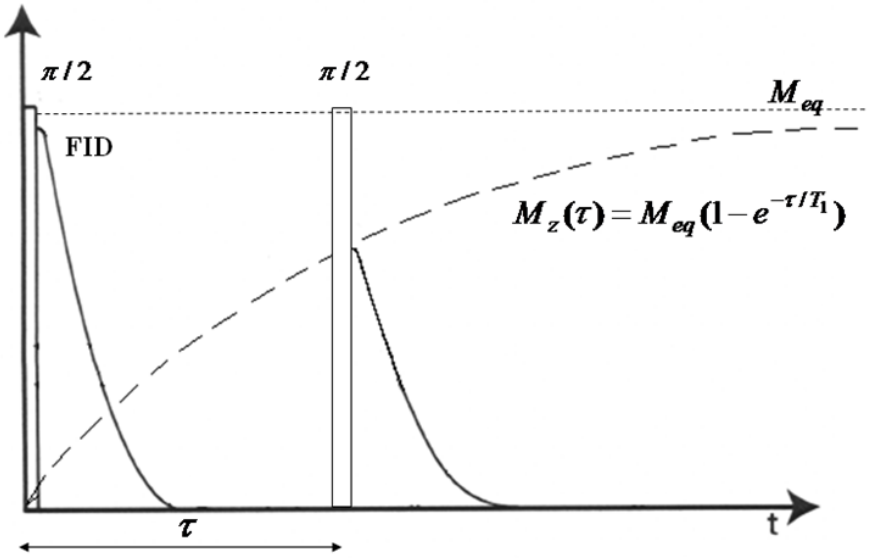

Figure 4.4: Typical sequence used to determine the spin-lattice relaxation time.

the magnetization. The second pulse drives the magnetization restored along z after τ into the perpendicular plane, while the third pulse creates the spin echo. Fixing τ_{echo} to a constant value $\ll T_2$ and varying τ, the T_1 time can be deduced (Fig. 4.4).

4.1.3 Hamiltonian of Interaction

The time evolution of the nuclear magnetization is determined by the hyperfine interactions acting on the nuclei. Thus, in order to correctly interpret the shape of the FID signal it is necessary to consider all the interactions acting on the nuclei. The nuclear hyperfine hamiltonian can be written as the sum of four terms:

$$\hat{\mathcal{H}} = \hat{\mathcal{H}}_Z + \hat{\mathcal{H}}_{nn} + \hat{\mathcal{H}}_{ne} + \hat{\mathcal{H}}_Q \quad , \tag{4.22}$$

where $\hat{\mathcal{H}}_Z = -\gamma\hbar \sum_j \hat{\mathbf{I}}_j \cdot \mathbf{H}_0$ is the Zeeman Hamiltonian, $\hat{\mathcal{H}}_{nn}$ is the nuclear dipole-dipole interaction, $\hat{\mathcal{H}}_{ne}$ describes the interactions between the nuclear and electronic spins, while $\hat{\mathcal{H}}_Q$ is the quadrupole hamiltonian associated with the interaction of the nuclear quadrupole moment Q with the electric field gradient generated by the charge distribution around the nucleus. For the analysis of the microscopic properties of the Pc_2Ln-based molecules under investigation, only the $\hat{\mathcal{H}}_{nn}$ and $\hat{\mathcal{H}}_{ne}$ interactions will be considered. The nuclear dipole-dipole interaction is

$$\hat{\mathcal{H}}_{nn} = \sum_{j<k} \frac{\hbar^2\gamma_n^2}{r_{jk}^3} \left(\hat{\mathbf{I}}^j\hat{\mathbf{I}}^k - 3\frac{(\hat{\mathbf{I}}^j\mathbf{r}_{jk})(\hat{\mathbf{I}}^k\mathbf{r}_{jk})}{r_{jk}^2} \right) \quad , \tag{4.23}$$

and it causes an homogeneous broadening of the resonance line. Nucleus-electron interaction is much stronger than nucleus-nucleus dipolar interaction (indeed $\gamma_n/\gamma_e \approx 10^{-3}$) and can be written

$$\hat{\mathcal{H}}_{ne} = -\gamma\hbar \sum_{i,k} \hat{\mathbf{I}}_i \, \tilde{A}_{ik} \, \hat{\mathbf{S}}_k \quad , \tag{4.24}$$

where $\tilde{A}_{ik}$ is the hyperfine coupling tensor. In general, $\tilde{A}_{ik}$ is a sum of a dipolar term plus a contact scalar term A'_{ji} which commutes with Zeeman Hamiltonian $\hat{\mathcal{H}}_Z$. The hyperfine tensor can then be written

$$\tilde{A}_{ik} = -\gamma_n\gamma_e\hbar^2 \left(\frac{r_{ik}^2 \tilde{I} - 3 \, \mathbf{r}_{ik} \cdot \mathbf{r}_{ik}}{r_{ik}^5} \right) - A'_{ik} \quad , \tag{4.25}$$

where $\tilde{I}$ is the identity tensor. The hyperfine field at the i-th nucleus is thus given by $\mathbf{h_i} = \sum_k \tilde{A}_{ik}\hat{\mathbf{S}}_k$. If the electron spins have a non-zero average polarization $\langle\hat{\mathbf{S}}\rangle$, then the local field probed by the nuclei is $\mathbf{h_i} = \sum_k \tilde{A}_{ik}\langle\hat{\mathbf{S}}_\mathbf{k}\rangle$. Therefore, it is possible to directly estimate $\langle\hat{\mathbf{S}}\rangle$ from the resonance frequency in the local field. In fact, when an external field is applied the nuclei experience a magnetic field

$$\mathbf{H} = \mathbf{H_0} + \sum_k \tilde{A}_{ik}\langle\hat{\mathbf{S}}_k\rangle \quad , \tag{4.26}$$

and the resonance frequency is then shifted to

$$\omega = \omega_0(1 + \tilde{K}) \quad , \tag{4.27}$$

with

$$\tilde{K} = \frac{\sum_k \tilde{A}_k\langle\hat{\mathbf{S}}_\mathbf{k}\rangle}{H_0} \quad . \tag{4.28}$$

The paramagnetic shift K of the NMR resonance spectrum is thus related to the static uniform susceptibility $\chi(\mathbf{q} = 0, \omega = 0)$ associated with those electron spins which interact with the nuclear ones, according to the equation

$$\tilde{K} = \sum_k \tilde{A}_k\chi(\mathbf{q} = 0, \omega = 0) \quad . \tag{4.29}$$

4.1.4 NMR Spectra

The NMR spectrum is defined as the Fourier transform of the FID signal G(t):

$$f(\omega - \omega_0) \propto \int G(t) \, e^{-i(\omega-\omega_0)t} dt \quad . \tag{4.30}$$

The quantity $f(\omega - \omega_0)$ represents the number of nuclei resonating at a frequency belonging to the infinitesimal interval $[\omega, \omega + d\omega]$. In the rigid lattice

approximation, the NMR spectrum is a gaussian. If the static field inhomogeneity effects are canceled by means of a spin echo sequence, the width of the NMR spectrum is mainly given by the local field distribution at each nucleus due to dipolar interactions with the neighbouring nuclei. However, due to the time dependence of the hyperfine hamiltonian, it is possible to observe a modification in the NMR spectra, which depends on the characteristic correlation times of the local field fluctuations. The hyperfine hamiltonian, which is considered as a perturbation of the Zeeman hamiltonian $\hat{\mathcal{H}}_Z$, can be written

$$\hat{\mathcal{H}}_{\mathcal{P}} = -\hbar\gamma \sum_i I_z^i h_z^i(t) = -\hbar \sum_i I_z^i \Delta\omega_i(t) \quad , \tag{4.31}$$

where the term $\Delta\omega_i(t)$ describes the fluctuations in the resonance frequency of the i-th nucleus. The FID signal is given by

$$G(t) = Tr\{e^{i\mathcal{H}_{\mathcal{P}}t/\hbar} M_x e^{-i\mathcal{H}_{\mathcal{P}}t/\hbar} M_x\} \quad . \tag{4.32}$$

By considering a stationary gaussian distribution for the fluctuations with a mean-square amplitude $\langle\Delta\omega^2\rangle$, Eq. (4.32) becomes [119]:

$$G(t) = G(0)\exp[-\langle\Delta\omega^2\rangle \int_0^t (t-\tau) g(\tau) d\tau] \quad , \tag{4.33}$$

where

$$g(\tau) = \frac{\langle\Delta\omega(t+\tau)\,\Delta\omega(t)\rangle}{\langle\Delta\omega^2\rangle} \tag{4.34}$$

is the normalized correlation function describing the fluctuation of the resonance frequency. The correlation time τ_c describes the characteristic decay time for $g(t)$ and it is defined as follows:

$$\tau_c = \int_0^\infty g(\tau) d\tau \quad . \tag{4.35}$$

Two limiting cases can be now distinguished:
Slow motion regime. $\tau_c \gg t$, where t is the time over which the FID signal is detected. Then $G(t)$ is characterized by a gaussian decay ($g(\tau) \simeq g(0) \simeq 1$)

$$G(t) \simeq G(0)\exp(-\langle\Delta\omega^2\rangle t^2/2) \quad , \tag{4.36}$$

as it is expected in the case of the rigid lattice approximation. In this regime the spin-spin relaxation rate is defined as $1/\mathrm{T}_2 = 1/\langle\Delta\omega^2\rangle$.
Fast motion regime. If $\tau_c \ll t$, Eq. (4.33) can be simplified as

$$G(t) \simeq G(0)\exp(-\langle\Delta\omega^2\rangle t\,\tau_c) = G(0)\exp(-t/T_2') \quad , \tag{4.37}$$

where the relaxation rate of the FID signal is

$$\frac{1}{T_2'} = \langle\Delta\omega^2\rangle\tau_c \quad . \tag{4.38}$$

It is to notice that since the FID decay is exponential, the $1/\mathrm{T}_2'$ represents the full width at half maximum of the corresponding lorentian spectrum. In fact, the line-width decreases upon decreasing τ_c and the so-called *motional narrowing* of the NMR line occurs.

4.1.5 Nuclear Spin-lattice Relaxation Rate $1/T_1$

The nuclear spin-lattice relaxation time T_1 describes the recovery to the equilibrium of the nuclear magnetization after a $\pi/2$ rf pulse. From the measurements of the characteristic time T_1 it is possible to derive information about the lattice dynamics in the MHz frequency range. In particular, by means of the $1/T_1$ analysis the low frequency excitation associated with the Ln^{3+} ion fluctuations in Pc_2Ln SMMs were investigated .
In the general case of $I > 1/2$ the recovery law can be deduced starting from the *master equations* [122]

$$\frac{dN_i}{dt} = \sum_j (W_{ji}N_j - W_{ij}N_i) \quad . \tag{4.39}$$

which describe the time evolution of the hyperfine levels populations N_i in terms of their transition probabilities W_{ij}. By solving the system of Eqs. (4.39), one finds

$$y(\tau) \doteq \frac{M_{eq} - M_z(\tau)}{M_{eq}} = \sum_j c_j \, e^{-\alpha_j \frac{\tau}{T_1}} \quad , \tag{4.40}$$

where the spin-lattice relaxation rate T_1 is defined as

$$1/T_1 \doteq 2W_{+-} \quad , \tag{4.41}$$

with W_{+-} the probability transition between the hyperfine levels $|m = +1/2\rangle \doteq |+\rangle$ and $|m = -1/2\rangle \doteq |-\rangle$. Eq. (4.40) reduces to Eq. (4.20) when I=1/2. The nuclear transitions are induced by the fluctuations of the local fields associated with the lattice dynamics. The corresponding time-dependent hamiltonian is given by

$$\hat{\mathcal{H}}_p(t) = -\gamma\hbar\hat{\mathbf{I}} \cdot \mathbf{h}(t) \quad . \tag{4.42}$$

In the framework of the the so-called *weak collision* approximation, which requires that the time dependent perturbation is small with respect to the Zeeman hamiltonian, the term (4.42) can be treated through a perturbation theory approach. The averaged transition probability between the levels $|+\rangle$ and $|-\rangle$ in the interval t is thus

$$\overline{P_{+-}(t)} = \frac{1}{\hbar} \left| \int_0^t e^{-iE_+t'/\hbar} \, \overline{\langle +|\hat{\mathcal{H}}_p(t)|-\rangle} \, e^{+iE_-t'/\hbar} dt' \right|^2 \quad . \tag{4.43}$$

By defining the correlation function

$$G(\tau) = \overline{\langle +|\hat{\mathcal{H}}_p(\tau)|-\rangle\langle -|\hat{\mathcal{H}}_p(0)|+\rangle} = \frac{\gamma^2\hbar^2}{4}\langle h_+(\tau)h_-(0)\rangle \quad , \tag{4.44}$$

the transition probability per unit time W_{+-} can be written as follows

$$W_{+-} = \frac{1}{\hbar} \int_{-t}^{t} e^{i\omega_0\tau} G(\tau) d\tau \quad . \tag{4.45}$$

The spin-lattice relaxation rate is thus proportional to the Fourier transform of the correlation function, e.g. the spectral density $J(\omega)$, at the resonance frequency ω_0:

$$\frac{1}{T_1} = 2W_{+-} = \frac{\gamma^2}{2}\int_{-\infty}^{\infty} e^{i\omega_0\tau}\langle h_+(\tau)h_-(0)\rangle d\tau = \frac{\gamma^2}{2}J(\omega_0) \quad , \tag{4.46}$$

where the integration limits can be moved to $\pm\infty$ since the characteristic time in which $G(\tau)$ decays is usually much shorter than the measurement time t. As expected from the magnetic-dipole selections rules, in Eq. (4.46) only the transverse components of the fluctuating magnetic field at the nucleus contribute to the relaxation rate $1/T_1$. If the correlation function $G(\tau)$ is characterized by an exponential decay

$$\langle h_+(\tau)h_-(0)\rangle = \langle \Delta h_\perp^2\rangle \, \exp(\frac{-t}{\tau_c}) \quad , \tag{4.47}$$

with *correlation time* τ_c and mean-squared amplitude $\langle \Delta h_\perp^2\rangle$, Eq. (4.46) becomes

$$\frac{1}{T_1} = \frac{\gamma^2}{2}\langle \Delta h_\perp^2\rangle \frac{2\tau_c}{1+\omega_0^2\tau_c^2} \quad . \tag{4.48}$$

The spectral density $J(\omega)$ is thus a lorentzian of width $1/\tau_c$ and centered at $\omega = 0$, whose shape depends on the lattice excitation while its area remains constant. The quantity $J(\omega_0)$ reaches its maximum value when the characteristic frequency of fluctuations matches the larmor frequency. When this condition is satisfied ($\omega_0\tau_c = 1$) the relaxation rate becomes

$$\left(\frac{1}{T_1}\right)_{max} = \frac{\gamma^2}{2}\langle \Delta h_\perp^2\rangle \frac{1}{\omega_0} \quad , \tag{4.49}$$

and an estimate of the hyperfine field at the nuclei can be deduced from the measurement of $(1/T_1)_{max}$. When $\omega_0\tau_c \neq 1$, two limiting cases can be distinguished:

$$\textit{Fast motion regime}, \ \text{if } \omega_0\tau_c \ll 1 \longrightarrow \ \frac{1}{T_1} = \frac{\gamma^2}{2}\langle \Delta h_\perp^2\rangle\tau_c \quad , \tag{4.50}$$

$$\textit{Slow motion regime}, \ \text{if } \omega_L\tau_c \gg 1 \longrightarrow \ \frac{1}{T_1} = \frac{\gamma^2}{2}\langle \Delta h_\perp^2\rangle\frac{1}{\omega_0^2\tau_c} \quad . \tag{4.51}$$

As it will be discussed later on in Chapter 5, in Pc_2Ln-based molecular magnets the nuclear magnetization relaxation is driven by the fluctuations of the Ln^{3+} ion electronic spins, which are coupled to the nuclei through hyperfine interactions. The electronic spin dynamics are directly related to the finite life-time τ_m of each sublevel m within the ground spin multiplet J, whose broadening is due to the spin-phonon coupling. The relaxation rate $1/T_1$ can

thus be expressed as the sum of all the contributions coming from each sublevel m, opportunely weighted with the Boltzmann factor [116]:

$$\frac{1}{T_1} = \frac{\gamma^2 \langle \Delta h_\perp^2 \rangle}{Z} \sum_m \frac{\tau_m \, e^{\frac{-E_m}{k_B T}}}{1 + \omega_0^2 \tau_m^2} \quad . \tag{4.52}$$

It is to note that in Eq. (4.52) each lorentzian describing the broadening of level m is now centered at the corresponding frequency $\omega_m \pm \omega_0$. While in the high temperature range the $1/\mathrm{T}_1$ measurement allows to derive information about the spin-phonon interactions, at very low temperature the thermal fluctuations are prevented and only the lowest levels are populated. In this range, the spin dynamics are driven by quantum fluctuations among the lowest states, which strongly depend on the mixing of the levels themselves.
On the other hand, Eq. (4.46) is quite general and can be applied both to metal and insulators. In particular, in a paramagnetic insulator the fluctuations are associated with electron spin excitations $\mathbf{h}(t) = \sum_i \tilde{A}_i \mathbf{S_i}(t)$. When the exchange coupling J_{ex} among the spins is much smaller than the thermal energy ($k_B T \gg J_{ex}$), the correlation function for each component of the i-th spin is [121]

$$\langle S^i_{x,y,z}(t) S^i_{x,y,z}(0) \rangle = |S_{x,y,z}|^2 e^{-\omega_{ex}^2 t^2/2} \quad , \tag{4.53}$$

where $\omega_{ex} = (J_{ex}/\hbar)\sqrt{2zS(S+1)/3}$ is the Heisemberg exchange frequency. Then one can find the following temperature independent expression for the relaxation rate:

$$1/T_1 = \frac{\gamma^2}{2} \sum_i \left([A^i_{xx}]^2 + [A^i_{yy}]^2 + [A^i_{zz}]^2 \right) \frac{S(S+1)}{3} \frac{\sqrt{2\pi}}{\omega_{ex}} \quad . \tag{4.54}$$

Eq. (4.54) allows to estimate ω_{ex} in the non-magnetic, neutral $[Pc_2\mathrm{Y}]^0$ compound, by means of $1/\mathrm{T}_1$ measurements in the high temperature limit (see Chapter 6). In general, in the presence of collective spin excitations the fluctuating field is

$$\mathbf{h}(t) = \frac{1}{\sqrt{N}} \sum_{\mathbf{q}} \sum_i e^{i\mathbf{q}\mathbf{r}_i} \tilde{A}_i \mathbf{S_q}(t) \quad . \tag{4.55}$$

By substituting the transverse components of $\mathbf{h}(t)$ in Eq. (4.46) and by making use of the fluctuation-dissipation theorem, the nuclear relaxation time becomes [121],[123]

$$1/T_1 = \frac{\gamma^2}{2N} \sum_{\mathbf{q}} \left(|A_{\mathbf{q}}|^2 \frac{\mathrm{Im}\chi_{\alpha\alpha}(\mathbf{q}, \omega_0)}{\omega_0} \right)_\perp \qquad \alpha = x, y, z \quad , \tag{4.56}$$

where $|A(\mathbf{q})|^2 = |\sum_i A^i_\alpha exp(i\mathbf{q}r_i)|^2$ is the form factor giving the hyperfine coupling of the nuclei with the spin excitations at wave-vector $\mathbf{q}$ and $\chi_{\alpha\alpha}(\mathbf{q}, \omega)$ is the dynamic susceptibility.

4.2 Muon Spin Relaxation

Muon Spin Relaxation or Rotation (μSR) technique makes use of muons as microscopic probes to be used to investigate a variety of phenomena in condensed matter physics, including those concerning magnetism, superconductors, semiconductors and quantum diffusion. Beams of positive spin-polarized muons, which are spin-1/2 particles, can be implanted in a sample in order to probe its static and dynamic properties, starting from the detection of the precession and relaxation of the muon spins in the presence of internal local magnetic fields and external fields. In this work, μSR technique was used in conjunction with NMR to probe the low-energy dynamics associated with rare-earth ion spins in lanthanide double-decker molecular magnets. In fact, the muon spin-lattice relaxation rate (λ) behaviour with temperature can be related to the rare-earth spin correlation time temperature dependence in the same way as for $1/T_1$. One of the advantages of μSR with respect to NMR is that it does not need the application of an external magnetic field to polarize the muons since the muon beam is already 100 % spin polarized when implanted in the sample, as it will be shown in the next paragraph. Thus, the experiments can be performed either in zero-field or in the presence of static or oscillating external fields, whose orientation can be parallel or perpendicular with respect to the direction of the muons polarization. The second important advantage is that by means of μSR it is possible to detect the signal in the sub-100 ns range, allowing to measure very fast spin-lattice relaxation times, reaching values of the order of 10 μs^{-1}. Hence, μSR measurements were performed in those samples characterized by a very large hyperfine coupling between the $f-$electrons localized on the rare-earth ion and the protons, since the detection of the NMR signal was prevented due to the too fast proton relaxation rates $1/T_1$. μSR measurements were carried out either at ISIS pulsed muon facility of Rutherford Appleton Laboratory, on MuSR beam line, or at PSI (Paul Scherrer Institute) muon facility on GPS (General Purpose Surface-Muon Instrument) and LTF (Low Temperature Facility) beam lines. In contrast to the ISIS measurements, the continuous beam muon production at PSI allows for a much more accurate determination of the short-time relaxation, as it will be shown in Chapter 5.
In the following, a brief description of the μSR technique will be presented.

4.2.1 Muon Production and Implantation

At μSR facilities beams of protons are accelerated up to 800 MeV by using synchrotrons or cyclotrons and made collide onto a carbon or berillium target, in order to produce muons. In fact, the proton-target collision causes the production of pions through the reaction

$$p + p \rightarrow \pi^+ + p + n \quad , \tag{4.57}$$

while the pions decay into muons and muon-neutrinos via

$$\pi^+ \rightarrow \mu^+ + \nu_\mu \quad . \tag{4.58}$$

Remarkably, by selecting pions which stop in the target and therefore are at rest while decaying, a beam of 100% spin-polarized muons can be produced. This is possible since the pion has zero spin and neutrino has negative helicity, which means that its spin is aligned antiparallel with its momentum. As a consequence, muon and neutrino spins must be opposite and they both are antiparallel with muon and neutrino momenta, respectively (see Fig. 4.5). Thus, some of the muons originating from motionless pions reach the sample under investigation with an energy of about 4 MeV and are fully polarized with respect to their flying direction. On the contrary, muons produced with moving pions are not polarized and they need special focusing magnets to be 60-80% polarized. After implanted in the sample, muons thermalize in few picoseconds, mainly by ionization of atoms and scattering with electrons. Since all the effects contributing to muons thermalization are Coulombic, the muon polarization is not affected at this stage. Moreover, only the initial part of the muon path is affected by radiation damage. The muon can still propagate through the sample for a distance of about 1 μm, far enough from sites where the high energy incident beam could have caused any lattice vacancy. The muon is characterized by a lifetime $\tau_\mu = 2.2$ μs and it decays in a three body process (Fig. 4.6)

$$\mu^+ \rightarrow e^+ + \nu_e + \bar{\nu}_\mu \quad . \tag{4.59}$$

The only detectable particle produced in this reaction is the positron e^+, whose energy varies depending on how momentum is distributed between the three particles. The phenomenon of not conserving parity, proper of weak interactions [124], leads to a propensity for the positron to be emitted predominantly along the direction of the muon spin when it decays (Fig. 4.7). The emission probability associated with a positron of energy E emitted along the direction forming an angle θ with the spin direction is

$$W^+(\theta, \epsilon) = 1 + A^+(\epsilon) cos\theta \quad , \tag{4.60}$$

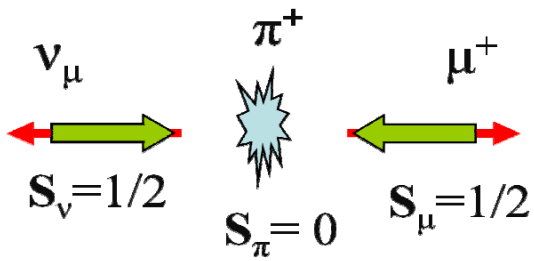

Figure 4.5: Schetch of the pion decay. The emitted muon and neutrinos have opposite momenta and negative helicity.

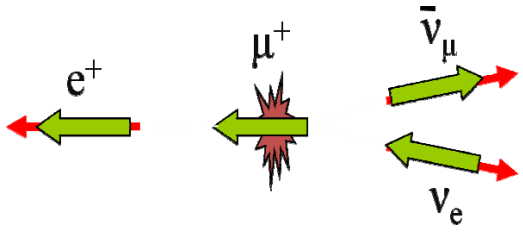

Figure 4.6: Schetch of the muon decay. The resulting positron has maximum energy when emitted in the opposite direction with respect to the two neutrinos.

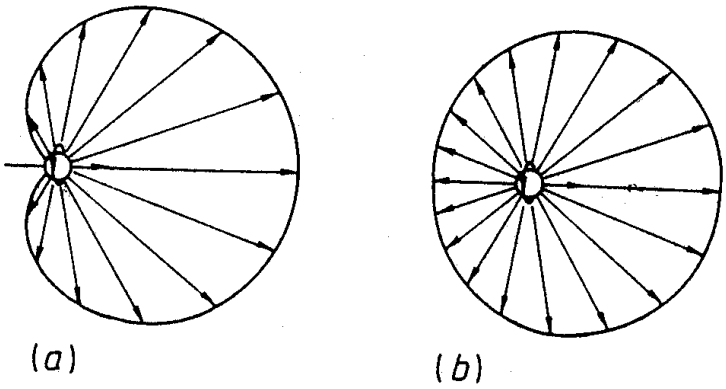

Figure 4.7: Angular distribution of positrons emitted during the muon decay for (a) $\epsilon = 1$ and (b) the case where positrons with all possible energies are revealed.

where $\epsilon = E/E_{max}$ is the ratio between the positron energy E and its maximum energy $E_{max} \simeq 52$ MeV and A^+ is the *asymmetry factor*, given by

$$A^+(\epsilon) = \frac{2\epsilon - 1}{3 - 2\epsilon} \quad , \tag{4.61}$$

This effect allows to follow the polarization of an ensamble of precessing muons with arbitrary accuracy, depending on the number of events one decides to acquire, by detecting the emitted positrons. The analysis of the time evolution of the muon polarization in a material allows to derive information about the distribution of local static fields or about the dynamics associated with fluctuating fields.
At ISIS, μ^+ are produced in packages of 10^4-10^5 unities and about 80 ns duration, with a 50 Hz rate. The periodic trigger of the pulses is in this case used as a clock and the relaxation processes are recorded in the time between two pulses. The time limit of an acquisition is limited by the length of muon pulses. On the contrary in a continuous source facility like PSI, the muons arrive to the sample intermittently. When a muon enter in the experiment

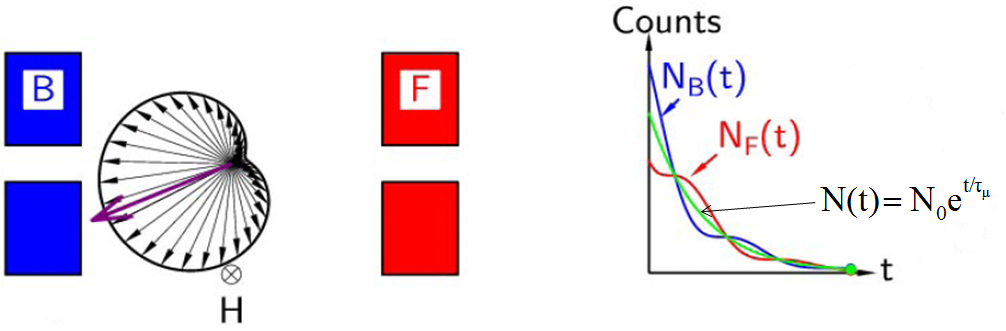

Figure 4.8: Schematic illustration of a μSR experiment. On the left, a spin-polarized beam of muons is implanted in a sample. Following decay, positrons are detected in either a forward detector F or a backward detector B. If a transverse magnetic field H is applied to the sample then the muons will precess. On the right, the number of positrons detected in the forward and backward detectors together with the exponential muon decay.

area, it must be detected by starting a clock, which is stopped when the the emitted positron is revealed by any detector. If a second muon arrives before the first one has decayed, this event must be disregarded since there is no way to distinguish between the two. The advantage of a continuous source of muons is the very high time resolution, of the order of few ns, which is limited only by the electronic of the detectors.

4.2.2 Muon Spin Relaxation Functions in Static Fields

Let us consider the detector configuration schematically depicted in Fig. (4.8): two groups of detectors are positioned in front (*forward detectors*) and in the back (*backward detectors*) of the sample. The time evolution of the number of positrons detected by the forward and backward detector is described by the functions $N_F(t)$ and $N_B(t)$ respectively. Since the muon decay is a radioactive process, these two terms sum to an exponential decay $N(t) = N(0)exp(t/\tau_\mu)$. The μSR signal is given by the *asymmetry function* defined as follows [125]

$$A(t) = |\mathbf{P}|G_\parallel(t) = \frac{N_B(t) - \alpha N_F(t)}{N_B(t) + \alpha N_F(t)} \quad , \tag{4.62}$$

where $|\mathbf{P}| = A\mathbf{P}_\mu(0)$ comprises an averaged asymmetry parameter A, including the detectors efficiency function, and the initial muon polarization $\mathbf{P}_\mu(0)$, $G_\parallel(t)$ is the *depolarization* or *relaxation function* describing the evolution of the muon polarization due to local interactions and α takes into account the different sensibility of the two groups B and F. If the sample possesses internal magnetic fields, it is not necessary to apply an external field to observe the muon precession. In the presence of a transverse field $\mathbf{H}$, instead, the muon precesses at angular frequency $\omega_\mu = \gamma_\mu H$, where $\gamma_\mu \simeq 85.1$ kHz G^{-1} is the

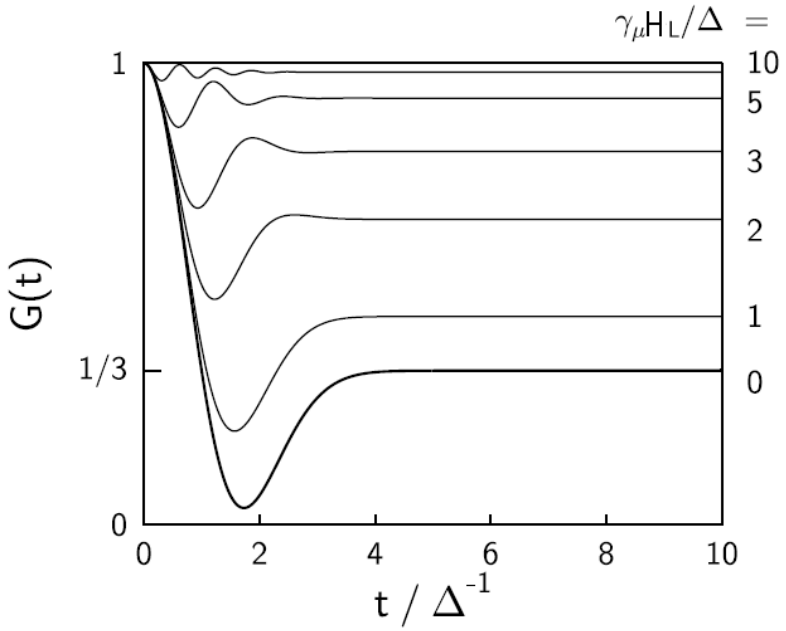

Figure 4.9: The Kubo-Toyabe relaxation function calculated for zero-applied field and for different values of the longitudinal field H_L.

muon gyromagnetic ratio. The presence of an inhomogeneous internal field distribution or of spin-spin interactions provokes a dephasing in the observed oscillations. On the other hand, an applied longitudinal field leads to the splitting of the muon Zeeman levels and to spin relaxation processes, which can be due to inhomogeneous field distribution or spin-lattice relaxation processes, in analogy with NMR experiments.

In zero- and longitudinal-field experiments the muon relaxation can be described by the *Kubo-Toyabe* function, shown in Fig. (4.9). The local internal field responsible for the muon spin precession at each muon site originates from a dipolar interaction with surrounding nuclear or electronic spins. Let us suppose that the local magnetic field at the muon site is at an angle of θ to the initial spin direction $\hat{\mathbf{z}}$. Then, the z-component of the muon spin polarization $G_\parallel(t)$ has a time-independent component proportional to $cos^2\theta$ and a $sin^2\theta$ component precessing at frequency $\omega_\mu = \gamma_\mu B$ [126]:

$$G_\parallel(t) = cos^2\theta + sin^2\theta cos\omega_\mu t \quad . \tag{4.63}$$

For a system of randomly oriented static nuclear dipoles, the probability distributions of the x, y and z components of resultant internal fields are Gaussian of width Δ/γ_μ, centered around zero. By assuming that at t=0 all muons are polarized along the z direction, then on average 1/3 will sense a net field directed along the x-, the y- and the z-directions. The 1/3 sensing a field along the z-direction will not precess. By averaging over the three directions and over the gaussian distributions one obtains the so-called *Kubo-Toyabe relaxation*

function [127]

$$G_{\parallel}^{KT}(t) = \frac{1}{3} + \frac{2}{3}\Big(1 - \Delta^2 t^2\Big)\, \exp\,(-\frac{1}{2}\Delta^2 t^2\,) \quad . \tag{4.64}$$

It can be notice from Fig. (4.9) that for short times the K-B function has a gaussian shape, while for longer times it recovers the one-third of average angular polarization present along the z direction. If an external longitudinal magnetic field H_L is applied, $B_{i=z}$ should be replaced by $B_z + H_L$ before the statistical average is taken. By assuming that the external field does not reorient the dipoles which give rise to the internal fields at the muon sites, the following expression can thus be obtained [127]

$$\begin{aligned} G_{\parallel}^{KT}(t,\omega_\mu) = \quad & 1 - \tfrac{2\Delta^2}{\omega_\mu^2}\left[1 - cos(\omega_\mu t) exp(-\tfrac{1}{2}\Delta^2 t^2)\right] + \\ & + \tfrac{2\Delta^4}{\omega_\mu^3}\int_0^t sin(\omega_\mu \tau) exp(-\tfrac{1}{2}\Delta^2 t^2) dt \quad . \end{aligned} \tag{4.65}$$

The effect of the external field is to cause the "1/3 tail" to increase. Since the magnetic field H_L is applied along the initial muon-spin direction, then in the limit of large H_L the muon-spin is held constant and does not relax from a value near unity.

4.2.3 Dynamic Muon Spin Relaxation Functions

Internal field dynamics, resulting either from the muon hopping from site to site or from the internal fields themselves fluctuating, can be accounted for within the so-called strong collision approximation. Within this approximation, it is assumed that the local field changes its direction at a time t according to a probability distribution $p(t) = exp(-\nu t)$, where ν represents the frequency of field fluctuations. Moreover, after such a "collision" the field is chosen randomly from its distribution $P(B_i)$, which is a gaussian in most cases, and is entirely uncorrelated with the field before the collision. The resulting *dynamic Kubo-Toyabe relaxation function* is plotted in Fig. (4.70) for different values of the ratio $R = \nu/\Delta$. For a gaussian field distribution in the fast fluctuation limit $R \gg 1$, in zero-field, the approximate form for $G^{DKT}(t)$ can be used [126]:

$$G_{\parallel}^{DKT}(t,\nu) \simeq exp(-2\Delta^2 t/\nu) = exp(-\lambda t) \quad , \tag{4.66}$$

where the 1/3 tail completely disappears. On the contrary, the typical exponential trend is found, in analogy with the nuclear relaxation behaviour in the motional narrowing regime. In the intermediate fluctuation limit $R > 1$, in zero field we have the so-called Abragam form [115]

$$G_{\parallel}^{DKT}(t,\nu) \simeq exp\left\{-\frac{2\gamma_\mu^2 \langle \Delta h_\perp^2 \rangle_\mu t}{\nu^2}(exp(-\nu t) - 1 + \nu t)\right\} \quad , \tag{4.67}$$

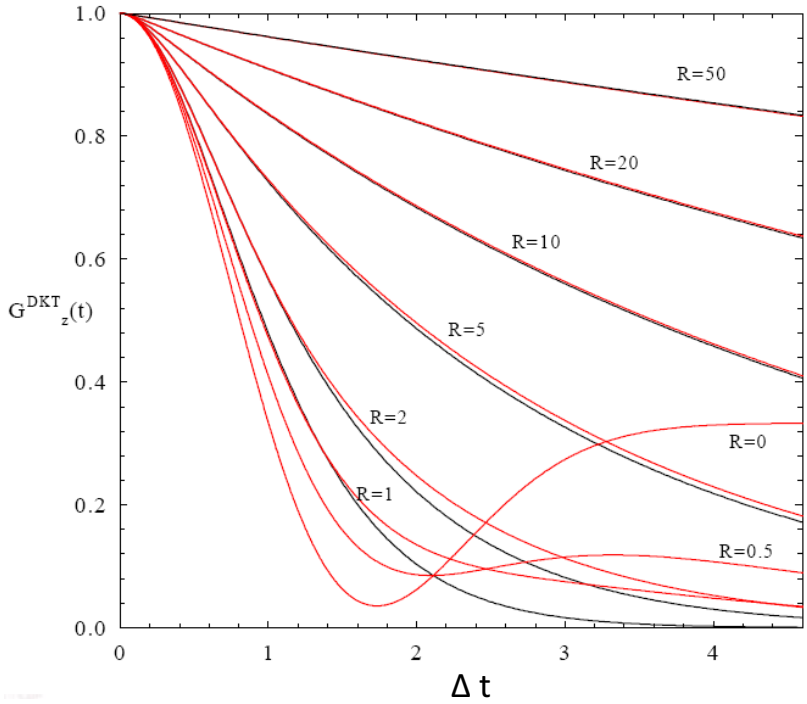

Figure 4.10: The dynamic Kubo-Toyabe function plotted as a function of the dimensionless parameters Δt and $R = \nu/\Delta$.

while for very slow fluctuations $R < 1$ only the 1/3 Kubo-Toyabe tail is affected. The simplified form of this tail thus becomes

$$G_{\parallel}^{DKT}(t,\nu) \simeq \frac{1}{3} exp(-(2/3)\nu t) \quad . \tag{4.68}$$

If an external magnetic field is applied along the z-direction, in the fast fluctuating limit the exponential decay $G_{\parallel}^{DKT}(t,\nu) \simeq exp(-\lambda t)$ still holds, but the muon relaxation mechanism is different. In fact, in analogy with NMR T_1-processes, the relaxation is due to spin transitions between muon hyperfine levels, induced by fluctuations in the transversal component of the local magnetic fields. Therefore Eqs. (4.46-4.48) can be rewritten for the muon relaxation time λ

$$\lambda = \frac{\gamma_\mu^2}{2} \int_{-\infty}^{\infty} e^{i\omega_\mu \tau} \langle h_+(\tau) h_-(0) \rangle d\tau = \frac{\gamma^2}{2} J(\omega_\mu) \quad , \tag{4.69}$$

$$\lambda = \frac{\Delta^2 \tau_c}{1 + \omega_\mu^2 \tau_c^2} \quad , \tag{4.70}$$

and the same consideration are still valid. On the other hand, if a longitudinal field is applied in the slow fluctuation limit, again only the tail of the dynamic K-T function is affected by the dynamics, but it is now shifted at higher values, depending on the value of the external field.

Chapter 5

Microscopic Properties of Pc_2Ln Molecular Magnets

In this Chapter, the investigation of the spin dynamics of Pc_2Ln molecular magnets by means of solid-state ^{1}H NMR and μSR experiments will be presented. The analysis of protons and muons spin-lattice relaxation rates ($1/T_1$ and λ, respectively) allowed to derive the temperature dependence of the correlation time τ_c associated with the spin fluctuations for a series of Pc_2Ln-based compounds. Estimates for the crystal field anisotropy barriers ΔE to spin reversal were also deduced for all the compounds under investigation. The results were compared with those obtained from magnetization measurements, reported in Chapter 3 and with the results previously derived by Ishikawa and collaborators in similar compounds.

^{1}H NMR measurements were performed first on a series of diluted compounds, $[Pc_2\text{Tb}]^-[\text{TBA}]^+_N$, characterized by different concentrations N of TBA molecules. It was demonstrated that the spin-lattice relaxation rates crucially depend on the magneto-thermic history in the diluted complexes only ($N > 1$), due to the high temperature molecular motions associated with the diamagnetic matrixes. Moreover, the anisotropy barrier and the correlation times behaviour with temperature were found to be strongly influenced by the degree of dilution with TBA organic groups. In fact, the arrangement of TBA molecules determines the symmetry of the crystal field on the Tb^{3+} ion and therefore can induce an enhancement of the degree of mixing between the crystal field levels, thus reducing the spin correlation times at low temperatures.

In the neutral $[Pc_2\text{Ln}]^0$ (Ln = Tb, Dy) both NMR and μSR measurements were performed, since the proton relaxation rate becomes too fast to be detected by means of NMR over a large region of the explored temperature range. The estimated high temperature correlation time behaviours and the corresponding estimates for the anisotropy barriers were found to be in good agreement with respect to the results obtained from DC and AC susceptibility measurements in the same high temperature range. On the other hand, macroscopic and microscopic techniques seem to probe different dynamics at low

temperatures, yielding different correlation times within the tunneling region. This result suggests the presence of electronic spin flip-flop like fluctuations, probably yielded by correlations between magnetic moments, that cannot be probed by means of a macroscopic technique.

From the analysis of the ^{1}H NMR spectra, reported in the following section, preliminary information about the TBA molecular dynamics in diluted compounds were derived. The large broadening of the NMR line for all the compounds under study provides evidence of the freezing of the magnetization along the anisotropy axis on cooling, confirming the presence of high barriers to the spin reversal.

5.1 ^{1}H NMR Spectra

In order to explore the influence of the molecular surrounding on the spin dynamic of the Tb^{3+} metal ion, solid-state ^{1}H NMR measurements were performed on a series of batches made by differently diamagnetically diluted samples, $[Pc_2Tb]^-[TBA]^+$ (**1**), $[Pc_2Tb]^-[TBA]^+ \times 9$[TBA]Br (**2**), and $[Pc_2Tb]^-[TBA]^+ \times 143$[TBA]Br (**3**).

The ^{1}H NMR spectra for the diluted samples **2** and **3** were obtained from the Fourier transform of half of the echo, since the full NMR line could be irradiated in the whole investigated temperature range. The spectra exhibit a progressive line broadening upon cooling, featuring a Gaussian line-shape below 200 K (Fig. 5.1). Above room temperature, however, the line changes to lorentzian-like and a narrow component grows on top of a broader one with intensity increasing upon increasing the sample temperature (Fig. 5.2). The temperature dependence of the line-width shows the same behavior expected for static susceptibility, till T = 200 K, while a clear narrowing is evident at higher temperatures, as shown in Fig. (5.3), suggesting the onset of molecular motions. The correlation time associated with the molecular dynamics cannot be easily derived. In fact, the presence of two lorentzian components in the spectra at high T indicates that the TBA molecules gradually freezes on cooling and they are probably characterized by a distribution of correlation times. Instead, from the line-width analysis below 200 K it is possible to estimate the strength of the hyperfine coupling constant in the diluted samples (see discussion).

A very different behavior characterizes the non-diluted sample $[Pc_2Tb]^-[TBA]^+$ (**1**). Here, the ^{1}H NMR spectra could be recorded only over a limited temperature range, precisely only below 40 K and over 100 K, because the fast proton relaxation occurring in the range 40 K $<$ T $<$ 100 K prevented observation of the NMR signals. Above 100 K and up to room temperature, the signal line-shape remains Gaussian and no motional narrowing effect was evidenced. On the contrary, upon decreasing the temperature to cryogenic one, the ^{1}H NMR spectrum in **1** becomes very broad and the NMR line could be only partially irradiated. Therefore, the spectrum could be derived from the envelope of

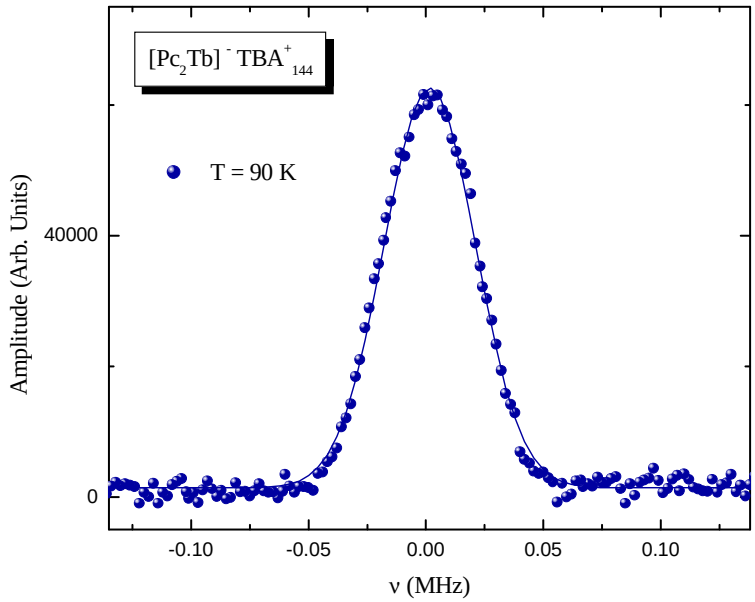

Figure 5.1: ^{1}H NMR spectrum of $[Pc_2\mathrm{Tb}]^-[\mathrm{TBA}]^+ \times 143[\mathrm{TBA}]\mathrm{Br}$ recorded at T = 90 K, in the applied field H = 1 T. The solid line shows the Gaussian shape with FWHM $\Delta\nu \simeq 50$ kHz.

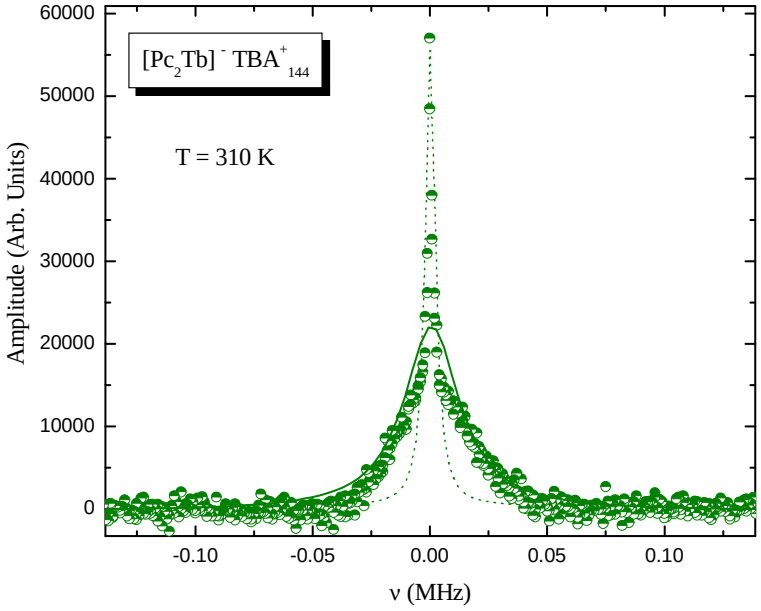

Figure 5.2: ^{1}H NMR spectrum of $[Pc_2\mathrm{Tb}]^-[\mathrm{TBA}]^+ \times 143[\mathrm{TBA}]\mathrm{Br}$ recorded at T = 309 K, in the applied field H = 1 T (circles). The solid and dotted lines represent the two lorentzian components with FWHM $\Delta\nu \simeq 25$ kHz and $\Delta\nu \simeq 7$ kHz, respectively.

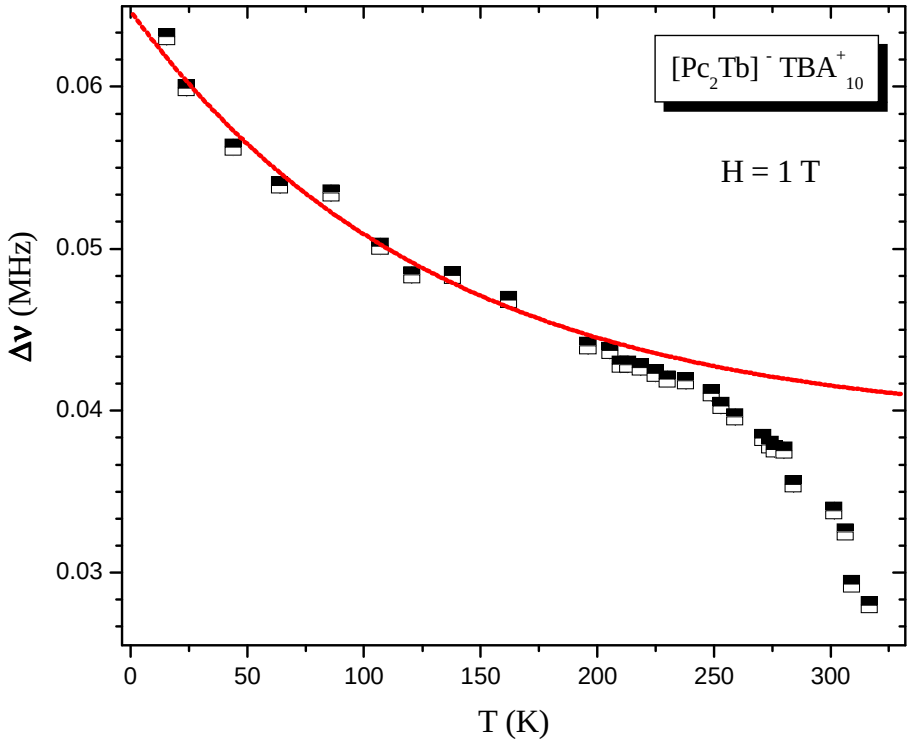

Figure 5.3: Temperature dependence of ^{1}H NMR line-width in $[Pc_2\text{Tb}]^-[\text{TBA}]^+ \times 9[\text{TBA}]\text{Br}$ (**2**). The solid line shows the behaviour expected from the temperature dependence of the susceptibility (χ_{mol}) as reported in Eq. (5.7). A clear narrowing is evident above 200 K.

the echo amplitude upon varying the irradiation frequency (Fig. 5.4). Such a broadening of the line indicates that in $[Pc_2\text{Tb}]^-[\text{TBA}]^+$ the average hyperfine coupling with the protons is much larger than in the more diluted samples **2** and **3**. Moreover, the broad spectrum provides direct evidence that the Tb^{3+} magnetic moments are frozen already at 20 K and fluctuate at frequencies well below the MHz range.

Even in the neutral $[Pc_2\text{Ln}]^0$ (Ln = Tb, Dy) complexes the too fast proton relaxation prevents the detection of the NMR signal in the 40 - 100 K temperature range. The $[Pc_2\text{Tb}]^0$ compound shows very similar ^{1}H NMR spectra to those of $[Pc_2\text{Tb}]^-[\text{TBA}]^+$. In fact, at high temperatures the line-shape remains gaussian, indicating that the molecular packing does not allow for molecular dynamics. On the other hand, the large broadening of the line at low temperatures is again a proof of the slowing down of the spin dynamics on cooling and of the strong hyperfine coupling with nuclei. On the contrary, in $[Pc_2\text{Dy}]^0$ compound the broadening of the line, though still present, is considerably reduced (Fig. 5.5). This result indicates that the hyperfine coupling with protons could be quite smaller in this compound. Moreover, as it will be shown later on, the Dy-based complex is characterized by slower spin dynamics. Therefore, due to the shorter correlation time of the spin fluctuation, at T = 20 K we are

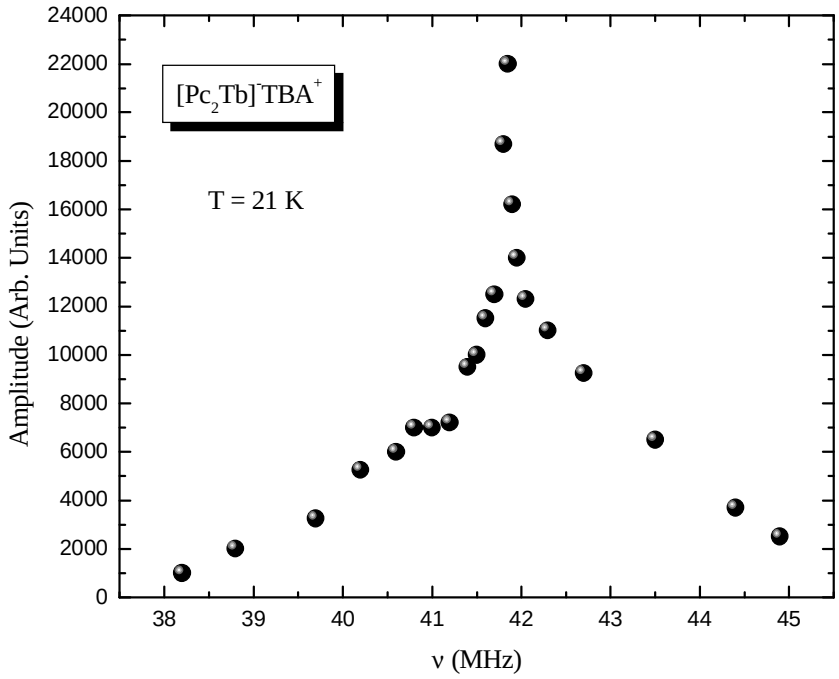

Figure 5.4: ^{1}H NMR spectrum of $[Pc_2\mathrm{Tb}]^-[\mathrm{TBA}]^+$ (**1**) recorded at T = 21 K, showing the very broad line width $\Delta\nu \simeq 4$ MHz.

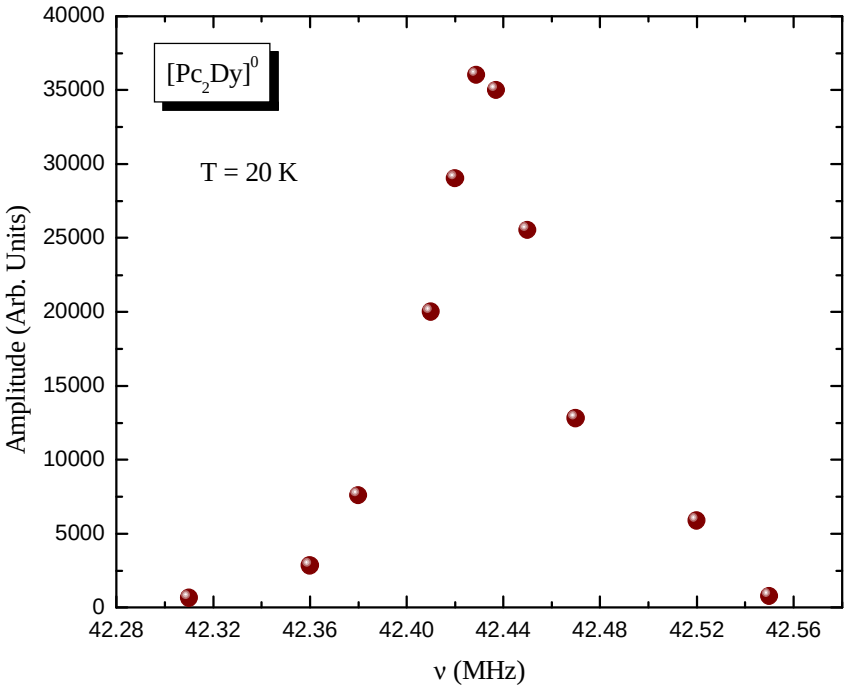

Figure 5.5: ^{1}H NMR spectrum of $[Pc_2\mathrm{Dy}]^0$ recorded at T = 20 K. The line-width is about $\Delta\nu \simeq 80$ kHz.

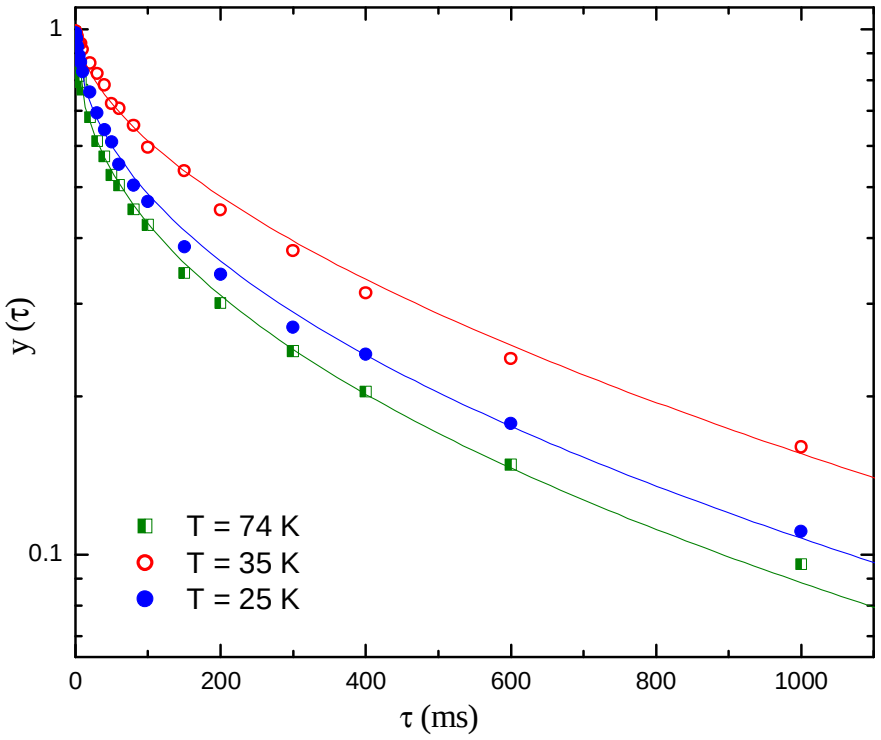

Figure 5.6: Recovery of the nuclear magnetization as a function of the delay τ in the standard spin-echo sequence, recorded at three selected temperatures, for $[Pc_2\mathrm{Tb}]^-[\mathrm{TBA}]^+\times$ 143 [TBA]Br (**3**) powders. The stretched character of the recovery laws indicates a distribution of $1/\mathrm{T}_1$.

still in the regime of fast fluctuation, which yield a narrowing of the NMR line. These results will be confirmed by means of the analysis of protons and muons spin-lattice relaxation rates, which allows for an accurate estimate of the correlation time temperature dependence and of the static distribution of fields on the protons (muons) sites.

5.2 Spin-lattice Relaxation Times in Pc_2Ln

5.2.1 ^{1}H NMR in $[Pc_2\mathrm{Tb}]^-[\mathrm{TBA}]^+_N$

The nuclear spin-lattice relaxation rates were extracted for **1**, **2** and **3** from the recovery of nuclear magnetization $m(\tau)$, after a saturation recovery pulse sequence. Below 200 K the recovery law $y(\tau) = 1 - m(\tau)/m(\tau \to \infty)$ is a stretched exponential function, given by the following expression:

$$y(\tau) = exp(-(\tau/T_1))^{\beta} \quad . \tag{5.1}$$

In **2** and **3** the values of the exponent β were found to be $\beta \simeq 0.5$, irrespective of the diamagnetic [TBA]Br dilution, and almost temperature independent.

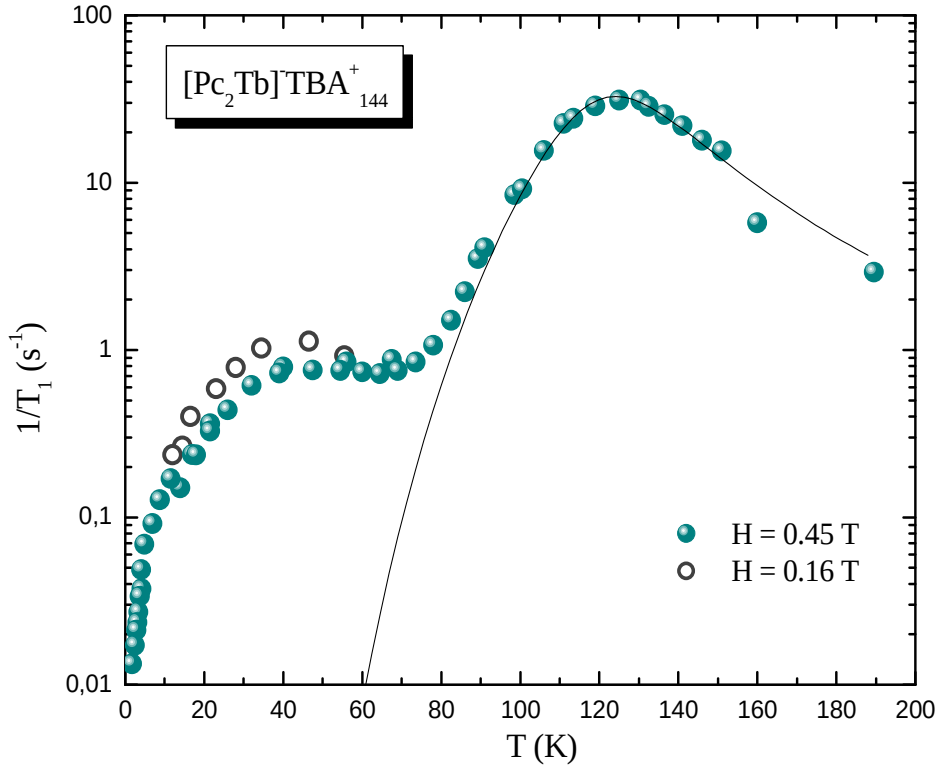

Figure 5.7: Temperature dependence of $1/T_1$ in $[Pc_2Tb]^-[TBA]^+ \times$ 143 [TBA]Br (**3**) powders. The solid circles are experimental data for H = 0.45 T, while the open circles are data taken in H = 0.16 T. The solid line represents the best fit in the high-temperature range according to Eq. (5.12) (see text).

Such an expression for the recovery law mirrors the presence of a distribution in relaxation rates for different ^{1}H nuclei, arising from the different hyperfine couplings between the protons and the Tb^{3+} ions. In fact, in the presence of a continuous spin-lattice relaxation times distribution, $f(1/T_1)$, the spin-lattice relaxation rate $1/T_1$ obtained by fitting the recovery with Eq. (5.1) provides an averaged value over the whole distribution. Especially, when $\beta = 0.5$ the distribution $f(1/T_1)$ is given by [128]

$$f(1/T_1) = \frac{\sqrt{1/\overline{T}_1}}{2\sqrt{\pi(1/T_1)^3}} \exp\left(\frac{-(T_1)}{4\overline{T}_1}\right) \quad , \tag{5.2}$$

where $\overline{T}_1$ is the expectation value of T_1. In the undiluted $[Pc_2Tb]^-[TBA]^+$ the value of the stretching factor was found to be quite larger, $\beta \simeq 0.7$. Indeed, in the absence of dilution with TBA molecules, the distribution of proton sites becomes narrower, yielding a β value closer to unity. The observed temperature dependence of $1/T_1$ for **2** and **3** initially showed poor reproducibility. In fact, the relaxation rates were found to depend both on the cooling rate and on the intensity of the magnetic field applied during the cooling procedures. These

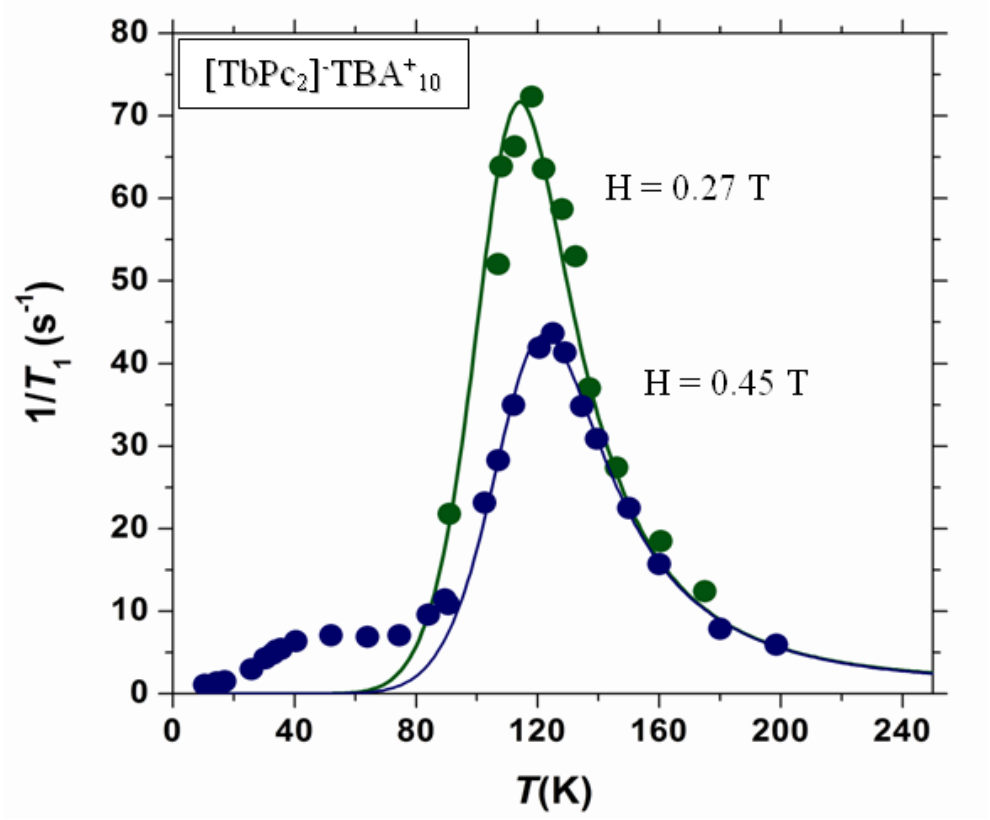

Figure 5.8: Field and temperature dependence of $1/T_1$ in $[Pc_2Tb]^-[TBA]^+ \times 9$ [TBA]Br (**2**) powders for H = 0.45 T (blue circles) and H = 0.27 T (green circles). The solid lines show the best fit according to Eq. (5.12) (see text).

results had been already foreseen from static susceptibility measurements, reported in Chapter 3, and will be confirmed later on through the ^{1}H NMR spectra analysis (Par. 5.3.1). They give a further evidence that the excess of $[TBA]^+$ and its molecular arrangement around $[Pc_2Tb]^-$ can significantly affect $1/T_1$. Therefore, trials were made in order to optimize the experimental conditions which granted reproducibility later on. These conditions were obtained by annealing the diluted samples for 30 minutes at 320 K and then cooling down to 200 K at a rate of 1 K/min, or less, under 1 T of applied magnetic field. The $1/T_1$ temperature dependence results for **2** and **3**, recorded below T = 200 K after employment of such annealing and cooling procedures, are depicted in Fig. (5.7-5.8). Both samples evidenced the presence of a peak in $1/T_1$ around T = 130 K, while at lower temperatures the $1/T_1$ trends versus T produced a strained shoulder. Furthermore, the intensities of the high temperature peaks were found inversely proportional to the field intensity (Fig. 5.8). These properties highlight the presence of fluctuations at a frequency ν close to the nuclear Larmor frequency (ν_0) around T = 130 K. In fact, such fluctuations, which are associated with the Tb^{3+} ion spin finite lifetime (see discussion), slow down on cooling, yielding a maximum in the proton relax-

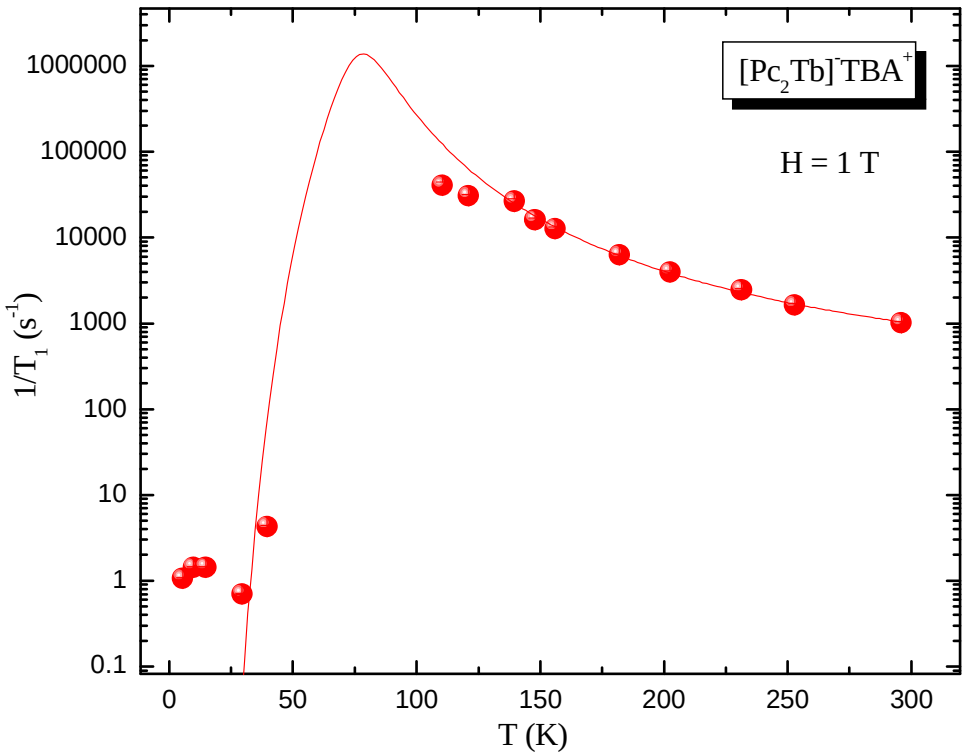

Figure 5.9: Temperature dependence of $1/T_1$ in $[Pc_2Tb]^-[TBA]^+$ (**1**) powders for H = 1 T. In the temperature range 40 K < T < 140 K, the proton relaxation rate is too fast to be detected. The solid line shows the best fit according to Eq. (5.12) (see text).

ation rate trend with temperature when their characteristic frequency matches the Larmor frequency.

As expected, in $[Pc_2Tb]^-[TBA]^+$ the $1/T_1$ was unaffected by the cooling rate and the intensity of the magnetic field applied while cooling, which evidenced no history dependence. Indeed, as it was deduced from the ^{1}H NMR spectra measurements, the absence of molecular dynamics warrants a fixed configuration of TBA groups in the proximity of $[Pc_2Tb]^-$ molecules. Moreover, it should be noticed that in the non-diluted sample **1**, $1/T_1$ is more than 2 orders of magnitude larger than in **2** and **3**, as shown in Fig. (5.9), and below 100 K the relaxation is so fast that makes impossible to detect the proton signal, which is recovered only below 40 K when also the transverse relaxation time becomes again long enough. The detailed analysis of the ^{1}H NMR line-width ($\Delta\nu$) and $1/T_1$ (see Par. 5.3) can provide further insight on the rotational dynamics of $[TBA]^+$ and its potential effect on tuning the relaxation barrier of $[Pc_2Tb]^-$.

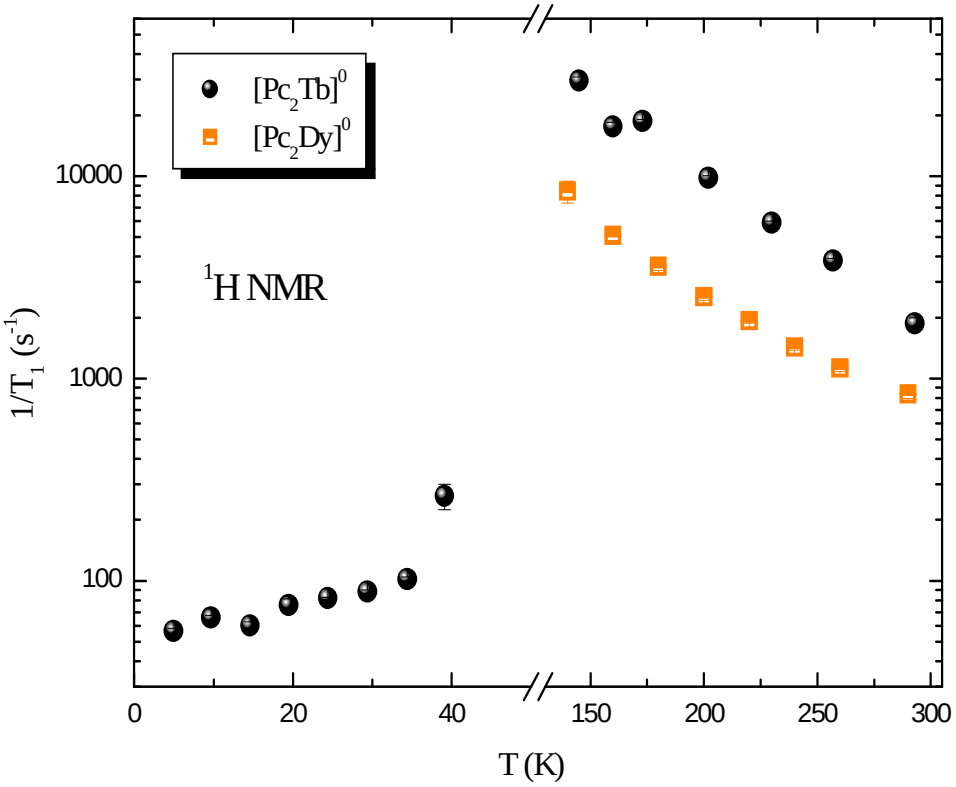

Figure 5.10: Temperature dependence of ^{1}H $1/T_1$ for $[Pc_2Tb]^0$ (circles) and $[Pc_2Dy]^0$ (squares), measured for H = 1 T. The T region in which the proton relaxation time cannot be detected is not shown in the T axis.

5.2.2 ^{1}H NMR and μSR in the Neutral $[Pc_2Tb]^0$ and $[Pc_2Dy]^0$

The ^1H spin-lattice relaxation times were estimated for the neutral $[Pc_2Tb]^0$ and $[Pc_2Dy]^0$ compounds from the recovery of the nuclear magnetization after a saturating rf pulse sequence. As in the diluted samples, the recovery was found to be a stretched exponential, but with a quite larger stretched parameter $\beta \simeq 0.8$. In fact, in the absence of TBA groups, the distribution of relaxation rates for the ^{1}H nuclei must be related solely to the differences in the hyperfine coupling between the Ln^{3+} ion and the 16 protons in each Pc molecule. The T dependence of $1/T_1$ evidences a progressive increase upon cooling from room temperature down to T$\simeq$ 140 K, while for T $\leq$ 40 K $1/T_1$ is found to progressively decrease. In the intermediate T range 40 K $\leq$ T $\leq$ 140 K, the observation of ^{1}H NMR signal is prevented by the short relaxation times, as it happened for the $[Pc_2Tb]^-TBA^+$ compound. In order to explore the proton relaxation times in these intermediate T ranges, μSR experiments were performed in the neutral compounds. Indeed, one of the advantages of this technique is the possibility to perform measurements of much faster relaxation rates. In addition, μSR allows to work at low fields, thus perturbing

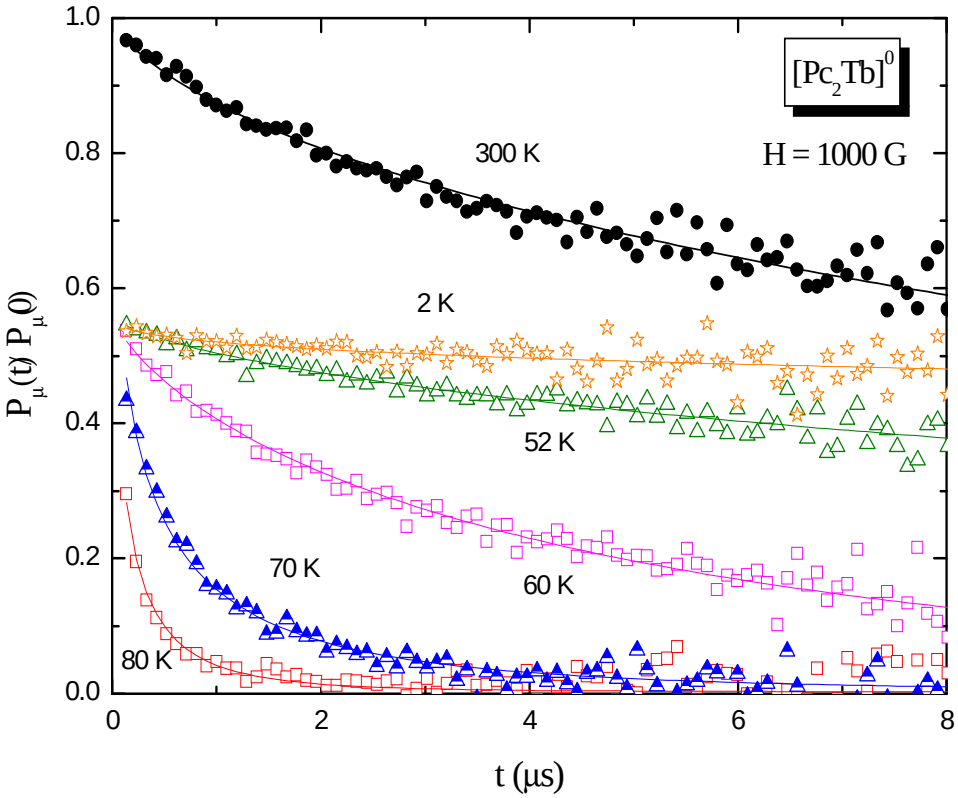

Figure 5.11: Time evolution of the muon polarization in $[Pc_2\text{Tb}]^0$ sample normalized to its value for t→0 at six selected temperatures.

the SMM only to a minor extent. Zero-field (ZF) and longitudinal field (LF) μSR experiments in the 50 mK-300 K temperature range were carried out at ISIS pulsed muon facility on μSR beam line first and at the PSI (Paul Scherrer Institute) in a second run. Thanks to the better short-time resolution of the PSI spectrometer, associated with the continuous muon beam, the muon depolarization could be detected even in the sub-100 ns time regime.
In Fig. (5.11), the time evolution of the muon polarization in $[Pc_2\text{Tb}]^0$ sample, detected at ISIS facility, is shown. Similar polarization curves were also obtained for $[Pc_2\text{Dy}]^0$ sample. The curves have been normalized to the value $P_\mu(t \to 0) = 30$ %, corresponding to the maximum initial asymmetry. The background asymmetry contribution was found to be around 10 % out of the 30 % total initial asymmetry for both samples. The time decay of the muon polarization $P_\mu(t)$ shows a different behavior for temperatures above and below T* $\simeq$ 90 K for $[Pc_2\text{Tb}]^0$ and T*$\simeq$ 60 K for $[Pc_2\text{Dy}]^0$. Indeed, above T* the decay follows a stretched exponential behavior

$$P_\mu(t) = Aexp(-(\lambda t)^\beta) \quad , \tag{5.3}$$

with an exponent of $\beta \simeq 0.5$ and an amplitude of A$\simeq$ 20%. Above T*, the muon relaxation rate λ is thus derived by fitting the experimental data to Eq. (5.3).
On the other hand, below T* a marked decrease in the initial asymmetry is

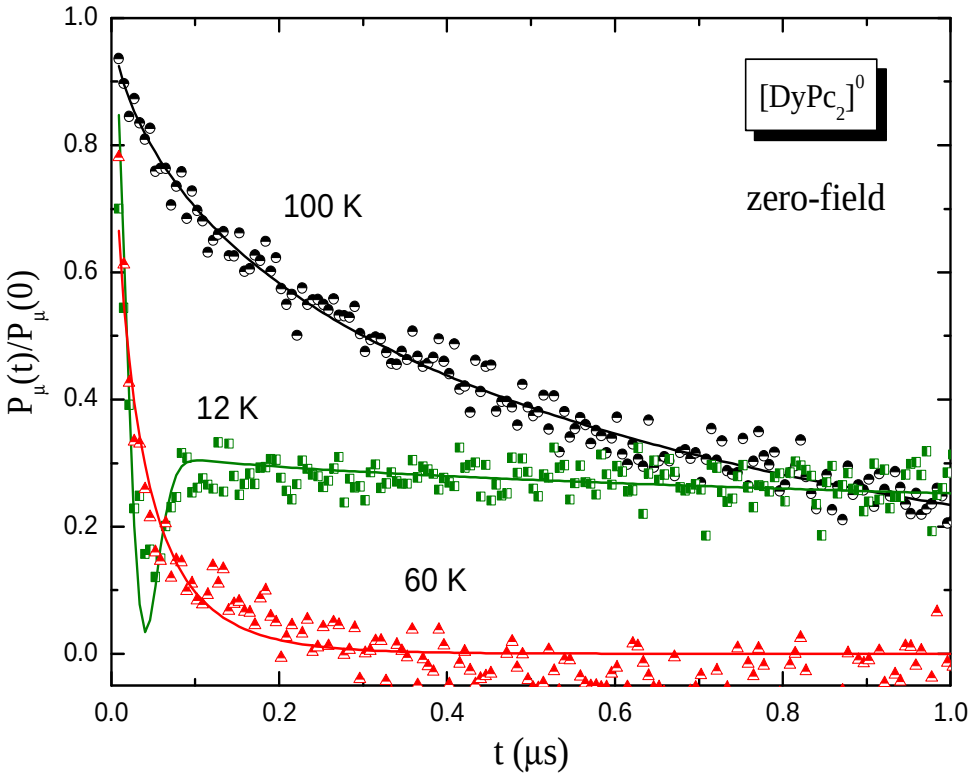

Figure 5.12: Time evolution of the muon polarization in zero-field in $[Pc_2\mathrm{Dy}]^0$ sample normalized to its value for t→0 at three selected temperatures.

found (see Fig. 5.11). This decrease has to be associated with the onset of very low frequency fluctuations. In particular, if the hyperfine field at the muon fluctuates with a characteristic correlation time $\tau_c \gg 1/(\gamma_\mu \sqrt{\langle \Delta h_\perp^2 \rangle_\mu})$, with γ_μ as the muon gyromagnetic ratio and $\sqrt{\langle \Delta h_\perp^2 \rangle_\mu}$ as the root-mean-squared static field distribution probed by the muons, the decay of $P_\mu(t)$ is given by the static Kubo-Toyabe (KT) function (see Chapter 4). In fact, in zero field the KT trend is characterized by a very fast initial decay and by the subsequent recovery of the muon polarization to A/3, while at longitudinal fields $H \sim \langle \Delta h_\perp^2 \rangle$ an increase $\alpha(H)$ in the tail amplitude of the Kubo-Toyabe relaxation is expected. However, at ISIS the initial fast decay cannot be detected, owing to the pulsed nature of the muon source. Accordingly, a loss in the initial polarization is observed and only the long-time tail is detected. Thus, since in the slow fluctuations regime only the tail of the KT depolarization function is affected by fluctuations, the recorded time evolution of the muon polarization is subjected to an exponential decay $P_\mu(t) = \alpha(H) exp(-(\lambda t)^\beta)$.

On the contrary, the presumed Kubo-Toyabe relaxation could be observed in μSR experiments performed at PSI facility, on GPS (General Purpose Surface-Muon Instrument). In fact, in contrast to the ISIS measurements, the continuous beam muon production at PSI allowed for a more accurate determination of the short-time relaxation. In Fig. (5.12) zero-field (ZF) de-

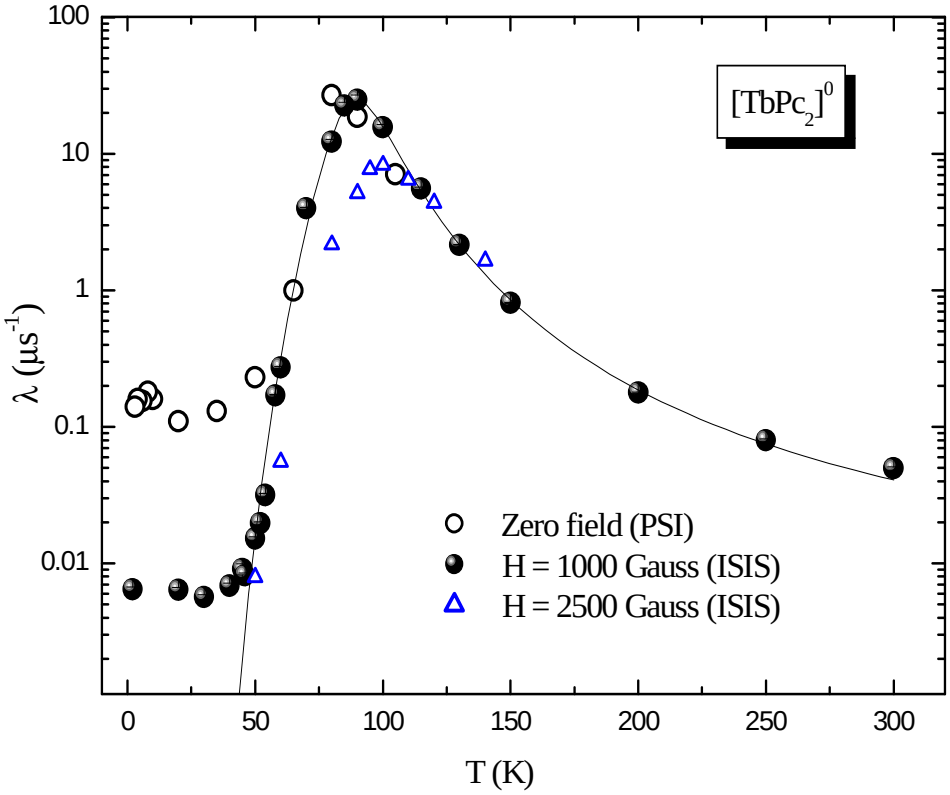

Figure 5.13: Temperature dependence of the muon longitudinal relaxation rate in $[Pc_2\text{Tb}]^0$ for zero-field (open circles), for H = 1000 Gauss (solid circles) and H = 2500 Gauss (triangles).

polarization curves at a few selected temperatures are shown for $[Pc_2\text{Dy}]^0$. Now, a Kubo-Toyabe relaxation is clearly observed below T*$\simeq$ 60 K, confirming the presence of very slow fluctuations below that temperature. In zero field, in the low temperature limit, the 1/3 tail of the KT depolarization function decays in the presence of slow fluctuations, according to

$$P_\mu(t) = \frac{1}{3} exp(-(2/3)\nu t)^\beta = \frac{1}{3} exp(-\lambda t)^\beta \quad , \tag{5.4}$$

with $\nu = 1/\tau_c$ being the characteristic frequency of the spin fluctuations and $\beta \simeq 0.5$. On the other hand, for T $\gg$ T*, the fast fluctuations limit is attained. In this limit the decay of the polarization in zero or in a longitudinal field is given by

$$P_\mu(t) = exp(-2\gamma_\mu^2 \langle \Delta h_\perp^2 \rangle_\mu t/\nu)^\beta = exp(-\lambda t)^\beta \quad , \tag{5.5}$$

where the exponent β is again $\simeq$ 0.5. In the intermediate fluctuation limit (T$\simeq$T*) it results $\nu/\gamma_\mu \sqrt{\langle \Delta h_\perp^2 \rangle_\mu} \geq 1$ and λ starts to decrease according to the

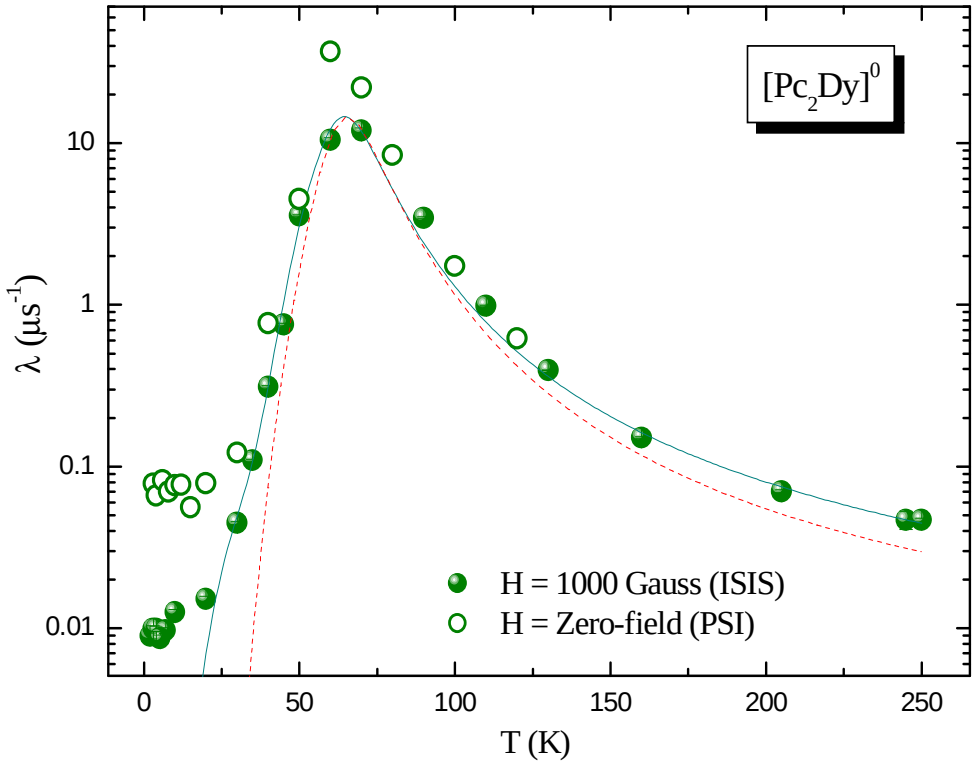

Figure 5.14: Temperature dependence of the muon longitudinal relaxation rate in $[Pc_2\mathrm{Dy}]^0$ for H = 1000 Gauss (solid circles) and for zero-field (open circles). The solid line is the best fit according to Eqs. (5.12-5.11), by using three different coupling constant, while the dashed line represents the fit according to Eqs (5.12-5.13).

so-called Abragam form [115]

$$P_\mu(t) = exp\left\{-\frac{2\gamma_\mu^2\langle\Delta h_\perp^2\rangle_\mu t}{\nu^2}(exp(-\nu t) - 1 + \nu t)\right\} \quad . \tag{5.6}$$

By using the aforementioned expressions for the decay of the polarization in the fast and slow fluctuations regimes it was possible to derive the T-dependence of λ in zero-field for both samples, which was compared with the one derived at ISIS for a 1000 G longitudinal field (Fig. 5.13-5.14). Looking at Fig. (5.13-5.14), one notices a peak around T = 90 K for $[Pc_2\mathrm{Tb}]^0$ and around T = 60 K for $[Pc_2\mathrm{Dy}]^0$, in agreement with the NMR findings. As expected, the intensity of the peak is observed to scale with the inverse of the field intensity, a situation found when the frequency of the fluctuations is close to Larmor frequency ν_0. At low temperatures a shoulder is present in both samples. This behaviour must be associated to the tunneling of the magnetization between the lowest states, as will be discussed in Par. 5.3.3.

5.3 Analysis of Results and Discussion

5.3.1 ^{1}H NMR Line-width Analysis in Diluted Compounds

From the observed line-width data in $[Pc_2\mathrm{Tb}]^-[\mathrm{TBA}]^+_N$ complexes, it is possible to give an estimate of the order of magnitude of the hyperfine coupling A. In diluted samples (**2**) and (**3**), below T = 200 K the line-width progressively increases upon cooling in a way proportional to the spin susceptibility χ_{mol}, as shown in Fig. (5.3). In fact, the paramagnetic shift K is related with the hyperfine constant A and with the susceptibility through the following relation:

$$K = \frac{A\chi_{mol}}{2\mu_B N_A} \quad . \tag{5.7}$$

K represents the shift in the Larmor frequency ν_0 due to the local field at the nuclei produced by the electronic spins. However, since in each unit cell of both sample several protons are present, each of them is characterized by a different hyperfine coupling with Tb^{3+} ions. Any distribution in A would therefore cause a spread of paramagnetic shifts, ΔK, and a line broadening $\Delta\nu/\nu_0 \propto \Delta K$ proportional to the magnetic susceptibility χ_{mol}. Moreover, in a powder sample, depending on the orientation of each crystallite with respect to the magnetic field, different components of the paramagnetic shift tensor are sensed simultaneously. Hence, the spectra for (**2**) and (**3**) are characterized by broadening associated also with the angular distribution of the paramagnetic shifts. In addition to that, it has been found that the proportionality factor relating $\Delta\nu$ with ΔK includes several terms such as the angular and site dependence of the hyperfine couplings and the anisotropy of the susceptibility itself. Therefore, from the slope extracted in the $\Delta\nu$ vs χ_{mol} plot (Fig. 5.15), it is possible to give only a rough estimate of the hyperfine coupling, which falls in the range of a few tens of Gauss. Such estimate is consistent with a hyperfine coupling dominated by the dipolar term. In fact, it should be remarked that in (**2**) and (**3**) most of the ^{1}H nuclei belong to the TBA molecules, and thus they are located rather apart from the the Tb^{3+} metal ions. On the contrary, at high temperatures $\Delta\nu/\nu_0$ is no longer proportional to χ_{mol} in (**2**) and (**3**) (Fig. 5.3). The observed breakdown of the linear trend originates from the onset of the molecular motions, which tend to average to zero the hyperfine fields at the nuclei. The narrowing of the line can be indeed associated with the fast rotational dynamics of $[\mathrm{TBA}]^+$ molecules at a frequency ν larger than the rigid lattice line-width measured at lower temperatures. Moreover, above room temperature, the onset of a narrow component in the ^{1}H NMR spectrum can be observed together with the progressive disappearance of the broader part of the spectrum (Fig. 5.2). The insurgence of a narrow component on top of a broader one for both diluted samples (**2**) and (**3**) indicates that the molecular dynamics are not characterized by a single correlation time but rather by a distribution of them. As the temperatures were raised, more

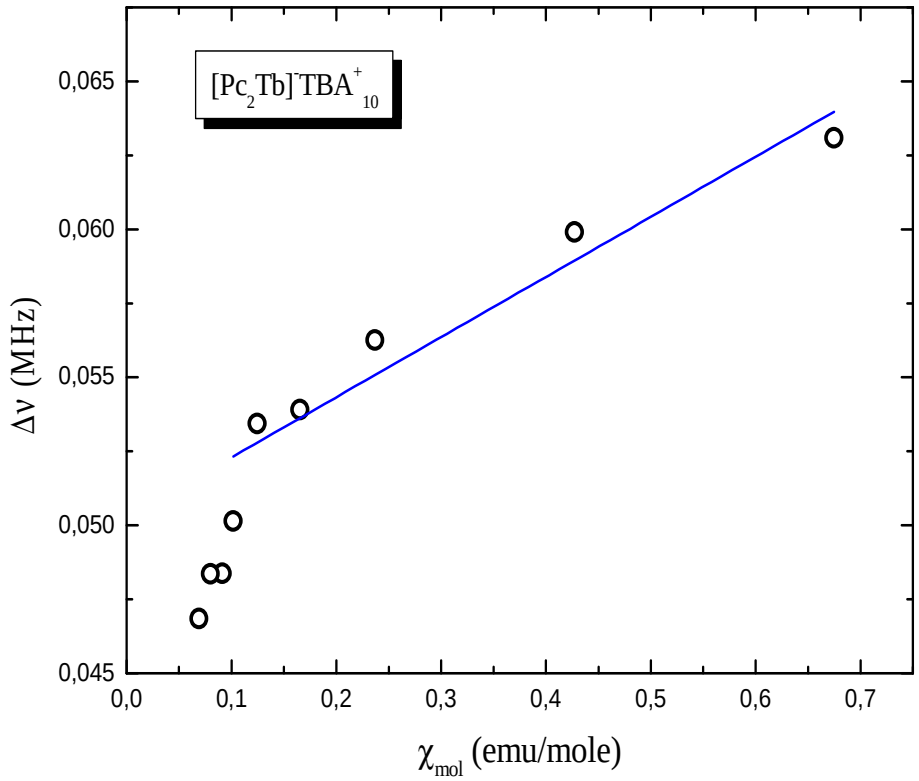

Figure 5.15: The line-width $\Delta\nu$ plotted as a function of the static molar susceptibility χ_{mol} for the $[Pc_2\text{Tb}]^-[\text{TBA}]^+_{10}$ compound. The linear relation $\Delta\nu \propto \chi_{mol}$ is no more valid for T $>$ 200 K.

and more molecules reach the motional narrowing condition, and the intensity of the narrow component in the NMR spectra increases. The line-width analysis indicates that all these processes are frozen below 200 K and therefore irrelevant in the analysis of the spin-lattice relaxation times data. However, the different configuration in which the $[\text{TBA}]^+$ cation freezes below 200 K is expected to affect the crystal field and accordingly the spin dynamics of these systems.

5.3.2 ^{1}H NMR Line-width Analysis in Non-diluted Compounds

In non-diluted $[Pc_2\text{Tb}]^-[\text{TBA}]^+$ (**1**) and in the neutral $[Pc_2\text{Tb}]^0$, most of the NMR signal comes from ^{1}H nuclei within Pc molecules. Then, a much larger average hyperfine coupling was expected. In fact, at low temperature a significant broadening of the line emerges (Fig. 5.4), consistent with a hyperfine field of about 500 Gauss. Moreover, as it will be shown later on, in the non-diluted compounds the low temperature correlation times for spin fluctuations are some order of magnitude larger with respect to the diluted samples. Thus, the

narrowing of the line associated with fluctuations of local fields is prevented. In the neutral $[Pc_2\mathrm{Dy}]^0$, the line-with at T = 20 K is much less broad with respect to the Tb-based compounds (Fig. 5.5). This result indicates that the magnetization is not yet frozen at 20 K, as happens in the other compounds, due to the slower spin dynamics associated with a smaller energy barrier to the spin reversal. The analysis of Kubo-Toyabe relaxation in the neutral compounds will give an accurate estimate of the distribution of static field at the muon sites, which was found to be in good agreement with previous evaluations.

5.3.3 Spin Dynamics in Pc_2Ln Derived from Nuclear and Muon Spin-Lattice Relaxation Rates

By means of ^{1}H nuclear and muon spin-lattice relaxation rate ($1/\mathrm{T}_1$ and λ) it is possible to probe the low frequency fluctuations of Tb^{3+} moments at the microscopic level, caused by the transitions among the different crystal field (CF) states. In the framework of the weak collision approximation, the relationship between the relaxation rate and the spectral density of the spin fluctuations can be obtained by a time dependent perturbation approach. This approximation requires that the time dependent perturbation is small with respect to the Zeeman Hamiltonian, so that many fluctuation events are needed to generate a nuclear (muon) spin relaxation transition. However, it must be remarked that, in view of the energy difference between the hyperfine levels and the m levels of Tb^{3+}, the direct nuclear relaxation process involving a spin excitation is forbidden. On the contrary, the effective relaxation processes are indirect ones, thus involving a nuclear spin flip without change in m. This is possible as the dipolar hyperfine Hamiltonian contains terms coupling $h_{x,y}$ to J_z. Indeed, the proton (muon) relaxation is driven by the electronic spin fluctuations within each crystal field level at frequency close to the Larmor frequency. The broadening of the CF levels and thus the spectral density of the spin excitations depend on the spin-phonon thermal interactions, which yield the finite life-time of the spin states. Therefore, the spin-lattice relaxation rates can be expressed in analogy with Eq. (4.46) of Chapter 4, but with the caveat that the spectral density $J(\omega)$ must be centered at the frequency ω_m corresponding to the energy of the level m. Moreover, the contribution of all the CF levels should be in principle considered. The expression for the relaxation rate thus becomes

$$\frac{1}{T_1} \text{ or } \lambda = \frac{\gamma^2}{2} \sum_m \int e^{i(\omega_m \pm \omega_0)t} \langle h_+(t) h_-(0) \rangle dt = \frac{\gamma^2}{2} \sum_m J(\omega_m \pm \omega_0) \quad , \quad (5.8)$$

where γ indicates the proton or muon gyromagnetic ratio and $h_\pm$ are the components of the hyperfine field at the nucleus (muon) perpendicular to the external magnetic field orientation. Upon taking a Lorentzian broadening of the sublevels, characterized by a finite lifetime (τ_m) due to spin-phonon scattering

processes, $1/T_1$ (λ) can be written as [116]

$$\frac{1}{T_1} \text{ or } \lambda = \frac{\gamma^2 \langle \Delta h_\perp^2 \rangle}{Z} \sum_{m=-J}^{+J} \frac{\tau_m e^{-E_m/kT}}{1+\omega_0^2 \tau_m^2} \quad , \tag{5.9}$$

where the term $\langle \Delta h_\perp^2 \rangle$ indicates the mean-square amplitude of the hyperfine field fluctuations, E_m the eigenvalues of the crystal field levels, and Z the corresponding partition function. The lifetime for the m sublevels can on the other hand be written in terms of the transition probability $p_{m,m\pm1}$ between m and $m \pm 1$ states:

$$\frac{1}{\tau_m} = p_{m,m-1} + p_{m,m+1} \quad . \tag{5.10}$$

Since the life-times are mainly determined by spin-phonon scattering processes, $p_{m,m\pm1}$ can be expressed in terms of eigenvalues of the crystal field levels, according to the following expressions [116]

$$P_{m,m-1} = C \frac{(E_{m-1}-E_m)^3}{e^{\frac{E_{m-1}-E_m}{k_B T}} - 1} \quad \text{and} \quad P_{m,m+1} = C \frac{(E_m - E_{m+1})^3}{1 - e^{-\frac{E_m - E_{m+1}}{k_B T}}} \quad . \tag{5.11}$$

The constant C (named R_{Or} in Par. 2.5) represents the spin-phonon coupling term and it is related to the matrix elements of the spin-lattice interaction potential V between the crystal field states.

5.3.4 Analysis of $1/T_1$ in $[Pc_2Tb]^-[TBA]_N^+$

The expected temperature dependence of $1/T_1$ derived from Eq. (5.9) by using the sublevel structure scheme proposed earlier by Ishikawa and collaborators [31] was compared to the measured $1/T_1$ in $[Pc_2Tb]^-[TBA]_N^+$ (N = 10 and 144). The value for $\langle \Delta h_\perp^2 \rangle$ was fixed by the maximum value of $1/T_1$ ($(1/T_1)_{max} = \gamma^2 \langle \Delta h_\perp^2 \rangle / (2\omega_0)$). As shown in Fig. (5.16), the observed $1/T_1$ behaviour against T is not well reproduced, for any choice of the adjustable parameter C. On the other hand, the high temperature peak in $1/T_1$ could be nicely reproduced by considering that the correlation function for the hyperfine field fluctuations is described by a single correlation time. This would imply that, within the explored temperature range and below 200 K, actually just the lowest levels are occupied. In this case, by considering that in the range $100 \leq T \leq 200$ K the thermal energy is much larger than the Zeeman splitting between the $m = \pm 6$ levels, these last can be considered degenerate, and Eq. (5.9) becomes

$$\frac{1}{T_1} = \gamma^2 \langle \Delta h_\perp^2 \rangle \frac{\tau_c}{1+\omega_0^2 \tau_c^2} \quad . \tag{5.12}$$

The correlation time τ_c follows the activated trend

$$\tau_c = \tau_0 exp(\Delta E/T) \quad , \tag{5.13}$$

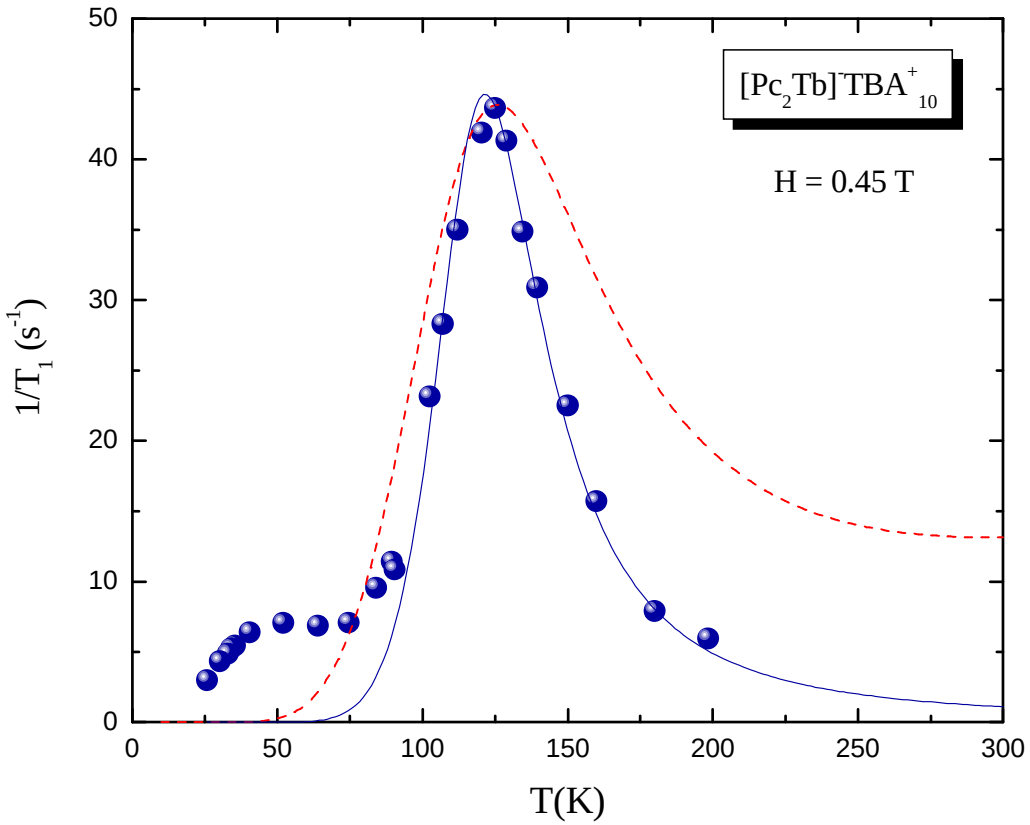

Figure 5.16: Temperature dependence of $1/T_1$ in $[Pc_2Tb]^-[TBA]^+ \times$ 9 [TBA]Br (**2**) powders for H = 0.45 T of applied field (circle). The dashed line shows the behavior expected according to Eq. (5.9) and assuming the sublevel scheme proposed by Ishikawa et al. (see text), while the solid line represents the fit of the experimental data to Eq. (5.12).

where $\tau_0 = (C\Delta E^3)^{-1}$ and ΔE is the energy difference between the $m = \pm 6$ and $m = \pm 5$ doublets. The best fit of the experimental data by using Eqs (5.12) and (5.13) yields C about 290 Hz/K^3 and a splitting $\Delta E \simeq 923$ K (e.g., $\Delta E \simeq 641$ cm^{-1}) for the most diluted compound $[Pc_2Tb]^-[TBA]^+_{144}$. In $[Pc_2Tb]^-[TBA]^+_{10}$ a similar value for the spin-phonon coupling constant was found, C $\simeq$ 206 Hz/K^3, and a quite smaller barrier, $\Delta E \simeq 833$ K (e.g., $\Delta E \simeq$ 578 cm^{-1}). These splittings are much larger than the one derived by Ishikawa et al. in the non-diluted compound $[Pc_2Tb]^-[TBA]^+$ [32][47] and significantly larger than the anisotropy barrier of any other known single molecule magnet. It should be noticed that in these systems the coupling constant C is about 2 orders of magnitude smaller than the one of Mn_{12} [116].
In the case of $[Pc_2Tb]^-[TBA]^+$ (**1**), the $1/T_1$ could not be measured close to the expected peak position, around T = 80 K, owing to the extremely fast nuclear spin-relaxation rates. Thus, the mean-squared amplitude of the hyperfine field fluctuations was fixed to the value $\langle \Delta h_\perp^2 \rangle \simeq (500)^2$ Gauss^2, as estimated from the low-temperature NMR spectra. The experimental data were nicely

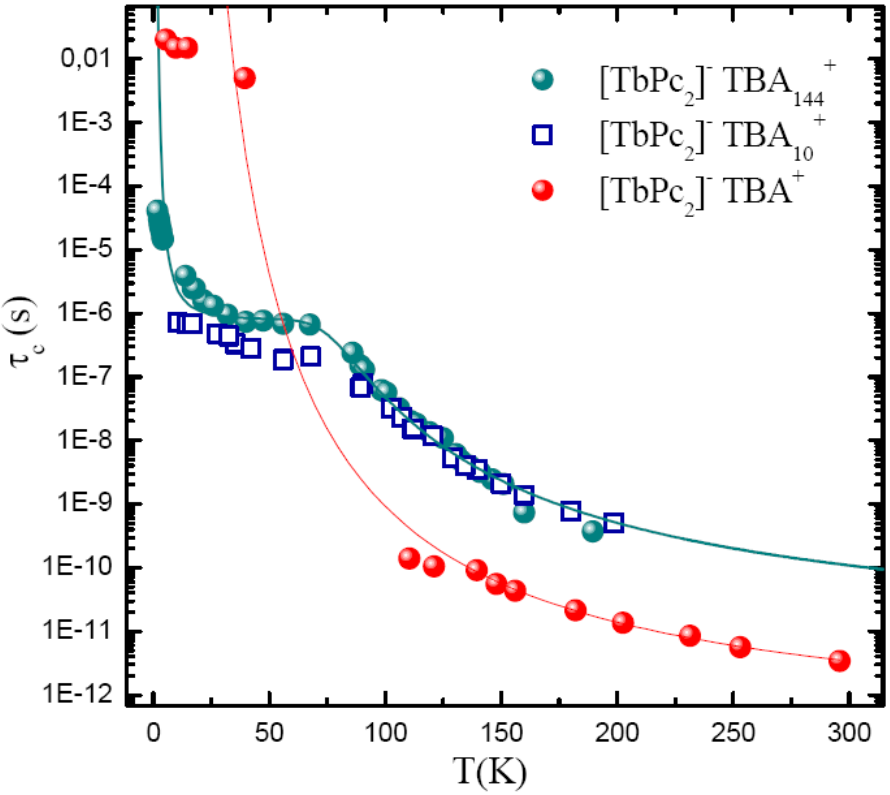

Figure 5.17: Temperature dependence of the characteristic fluctuation times for $[Pc_2\mathrm{Tb}]^-$ magnetic moment as derived from $1/\mathrm{T}_1$ data. The blue circles represent experimental data for $[Pc_2\mathrm{Tb}]^-[\mathrm{TBA}]^+\times$ 143[TBA]Br (**3**), while the open squares those for $[Pc_2\mathrm{Tb}]^-[\mathrm{TBA}]^+\times$ 9 [TBA]Br (**2**). The solid blue line shows the best fit to Eqs (5.14-5.15) of the data of sample (**2**) (see text). The red circles show the $[Pc_2\mathrm{Tb}]^-[\mathrm{TBA}]^+$ (**1**) experimental data, while the red line represents the corresponding activated high-temperature contribution to the relaxation time.

reproduced with $\Delta E = 840$ K (e.g., $\Delta E = 584$ cm^{-1}) and a constant C = 5000 Hz/K^3 (Fig. 5.9). These results indicate that in the high temperature range in (**1**) the spin-phonon coupling is very large and yields to a very short lifetime of crystal field levels, i.e. the system has a faster dynamics with respect to diluted samples. In Table (5.1) the estimates of ΔE, C and τ_0 for the three compounds are resumed.
Below 80 K, a clear departure from the behavior expected on the basis of an activated form for τ_c is observed in the three compounds. The temperature dependence of the correlation time describing the Tb^{3+} moments fluctuations was derived starting from Eq. (5.12) and using the experimentally determined $1/\mathrm{T}_1$. The temperature dependence of τ_c for undiluted **1** and diluted molecules **2** and **3**, are reported in Fig. (5.17). In the case of **2** and **3**, τ_c shows at high temperatures practically the same T dependency, irrespective of their different

	$\Delta E(K)$	$\tau_0(ps)$	$C\ (Hz/K^3)$
$[Pc_2Tb]^-TBA^+_{144}$	923 ±12	4.4 ± 0.2	~290
$[Pc_2Tb]^-TBA^+_{10}$	833 ± 48	8.4± 0.4	~206
$[Pc_2Tb]^-TBA^+$	840 ± 50	0.30 ± 0.09	~5600

Table 5.1: The table summarizes the most important parameters derived in $[Pc_2\mathrm{Tb}]^-[\mathrm{TBA}]^+_N$ compounds from the analysis of the temperature dependence of proton spin-lattice relaxation rate $1/\mathrm{T}_1$.

diamagnetic dilution, with the activated trend described by Eq. (5.13). As regard **1**, on the other hand, the τ was much shorter in the activated range. This effect is due to the smaller energy barrier characterizing **1** and to the larger spin-phonon coupling constant. Below 80 K a plateau can be observed. In this region, the lifetime of the ground-state doublet is determined only by the transitions among the $m = \pm 6$ states, yielding a nearly temperature-independent $1/\mathrm{T}_1$ between 80 and 30 K. Moreover, the estimated value for τ_c is remarkably different in the three compounds. In fact, since the transition probability is determined by the mixing of the $|m\rangle$ states, this variation should be ascribed to the different tunneling rate characterizing the systems, which can be associated with a different symmetry of the crystal field around $[Pc_2\mathrm{Tb}]^-$ and to a different state mixing in the two differently magnetically diluted samples. At lower temperatures, when $\mathrm{k}_B T \leq 12 g\mu_B H_0$, the Zeeman splitting among the $m = \pm 6$ levels prevents the tunneling processes and the mechanism becomes activated again with an energy gap Δ_H related to the Zeeman splitting. Thus, the total correlation time for the hyperfine field fluctuations can be expressed in terms of both the high-temperature activated contribution (Eqs 5.12-5.13) and the tunneling processes among ± 6 states:

$$\frac{1}{\tau_c} = \left(\frac{1}{\tau_c}\right)_{act} + \left(\frac{1}{\tau_c}\right)_{tun} \quad , \tag{5.14}$$

where $(1/\tau_c)_{tun}$ is practically temperature independent when $k_B T > 12 g\mu_B H_0$. Moreover, it should be noticed that in a powder sample the Zeeman splitting would depend on the orientation of the magnetic field with respect to the anisotropy axes $\hat{z}$. In fact, one can write $\Delta_H = 12 g\mu_B H_0 cos\theta$, with θ the angle between H_0 and $\hat{z}$. Accordingly, the correlation time estimated in the low-temperature range corresponds to an average over all possible orientations

and thus it is possible to write

$$\begin{aligned}(\tau_c)_{tun}(T) &= (\tau_c)_{tun}(\infty)\int_0^{\pi} sin\theta \times exp(12g\mu_B H_0 cos\theta/k_B T)d\theta = \\ &= (\tau_c)_{tun}(\infty) sinh\left(\frac{12g\mu_B H_0 cos\theta}{k_B T}\right) / \left(\frac{12g\mu_B H_0 cos\theta}{k_B T}\right).\end{aligned} \tag{5.15}$$

Here, $(\tau_c)_{tun}(\infty)$ represents the correlation time at temperatures T $\gg \Delta_H/k_B$. The experimentally determined τ_c values reported in Fig. (5.17) were modeled through Eq. (5.14) taking for $(\tau_c)_{tun}$ the expression given in Eq. (5.15).

5.3.5 Analysis of $1/T_1$ and λ in Neutral $[Pc_2Ln]^0$

From the analysis of the time evolution of the muon polarization in the regime of slow fluctuations it is possible to derive an estimate of the distribution of static field at the muons ($\sqrt{\langle \Delta h_\perp^2 \rangle_\mu}$). In fact, the increase in the tail amplitude of the Kubo-Toyabe relaxation at low T is expected to depend on both the applied longitudinal field and the internal local fields at the muons, as shown in Fig. (5.18) for the $[Pc_2Dy]^0$ compound (see Chapter 4, Eq. 4.65). In Fig. (5.19) the amplitude of the tail as a function of the external field is reported for both compounds at T = 30 K and T = 12 K respectively. At these temperatures, the electronic spin correlation time verifies the condition of slow dynamics $\tau_c \gg 1/(\gamma_\mu \sqrt{\langle \Delta h_\perp^2 \rangle_\mu})$, as it will be discussed later on. From the "repolarization" plot one can estimate $\sqrt{\langle \Delta h_\perp^2 \rangle_\mu} \simeq 590$ G and $\sqrt{\langle \Delta h_\perp^2 \rangle_\mu} \simeq 400$, for $[Pc_2Tb]^0$ and $[Pc_2Dy]^0$ respectively [115]. Thus, one has to expect that below T* Ln^{3+} moments are frozen over a time scale $1/(\gamma_\mu \sqrt{\langle \Delta h_\perp^2 \rangle_\mu}) \sim 10$ ns. On the other hand, by fitting the low-temperature data with a KT function one can estimate more accurately the static field distribution probed by the muons. It was found around $\sqrt{\langle \Delta h_\perp^2 \rangle_\mu} = 550$ G and $\sqrt{\langle \Delta h_\perp^2 \rangle_\mu} = 490$ G for the Tb and Dy compounds, respectively. These results are also consistent with the broadening of the ^{1}H NMR line at low temperatures, which has been discussed in Par. (5.3.2).

In $[Pc_2Tb]^0$, the temperature dependence of the muon spin-lattice relaxation rate in H = 1 kG was fitted according to Eqs (5.12-5.13). The spin-phonon coupling constant was estimated to be $C \simeq 3000$ Hz/K^3, of the same order of magnitude of that found in $[Pc_2Tb]^-TBA^+$ compound. It is noticed that for T > 100 K, $\tau_c\omega_L \ll 1$ and from Eq. (5.12) one has λ (or $1/T_1$)$\propto exp(\Delta/T)$. In fact, by plotting either $1/T_1$ or λ vs 1/T in a semi-logarithmic scale (Fig. 5.20), one finds a nice linear behavior, consistent with $\Delta E \simeq 880$ K (e.g., $\Delta E \simeq 611$ cm^{-1}). This value for the anisotropy barrier is compatible with the value $\Delta E \simeq 870$ K estimated from the the field dependence of λ at T = 90 K (Fig. 5.21). On the other hand, this estimate for the energy barrier is significantly larger with respect to the value derived by Ishikawa et al. in the same nominal compound ($\Delta E \simeq 590$ K)[49]. On the basis of Eq. (5.12), in light of the data reported in Fig. (5.13) for H = 1 kG, it is possible to derive the T dependence of τ_c for the Tb^{3+} spin fluctuations (Fig. 5.22).

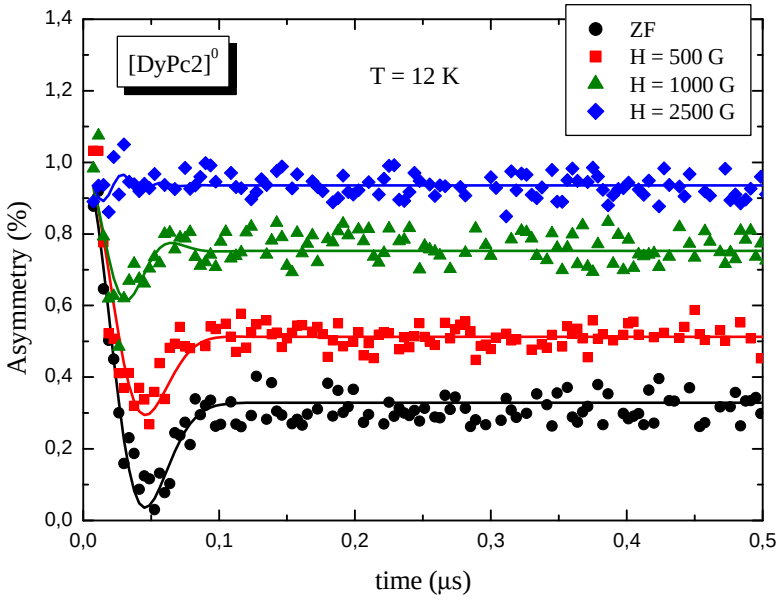

Figure 5.18: Time evolution of the muon polarization at T = 12 K and for different values of the applied longitudinal field in $[Pc_2\mathrm{Dy}]^0$ sample. The curves are normalized to the value measured for t→0. The solid lines represent the best fits to the KT function.

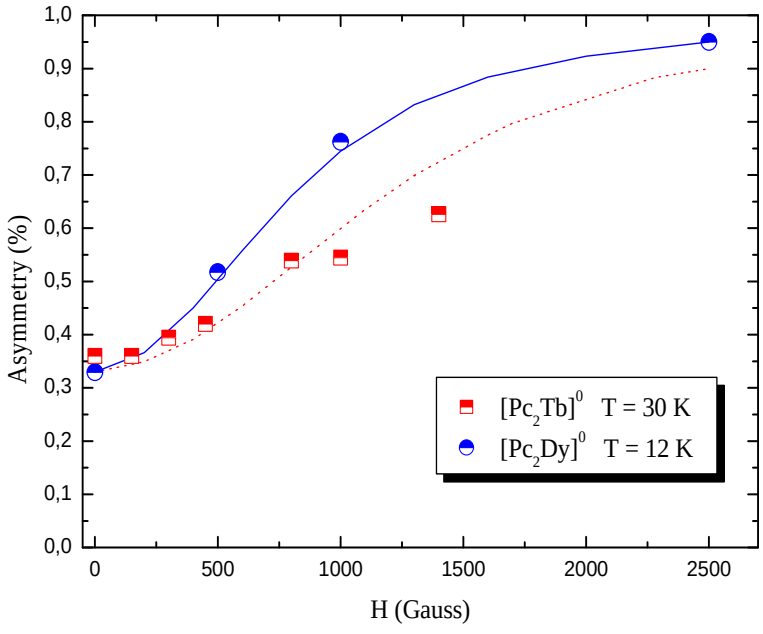

Figure 5.19: Field dependence of the Kubo-Toyabe long-time tail amplitude measured at T = 30 K and T = 12 K for $[Pc_2\mathrm{Tb}]^0$ (squares) and $[Pc_2\mathrm{Dy}]^0$ (circles) compounds. The experimental data are compatible with the theoretical behaviours calculated for $\sqrt{\langle \Delta h_\perp^2 \rangle_\mu}$ = 590 G and $\sqrt{\langle \Delta h_\perp^2 \rangle_\mu}$ = 400, respectively (dotted and solid lines).

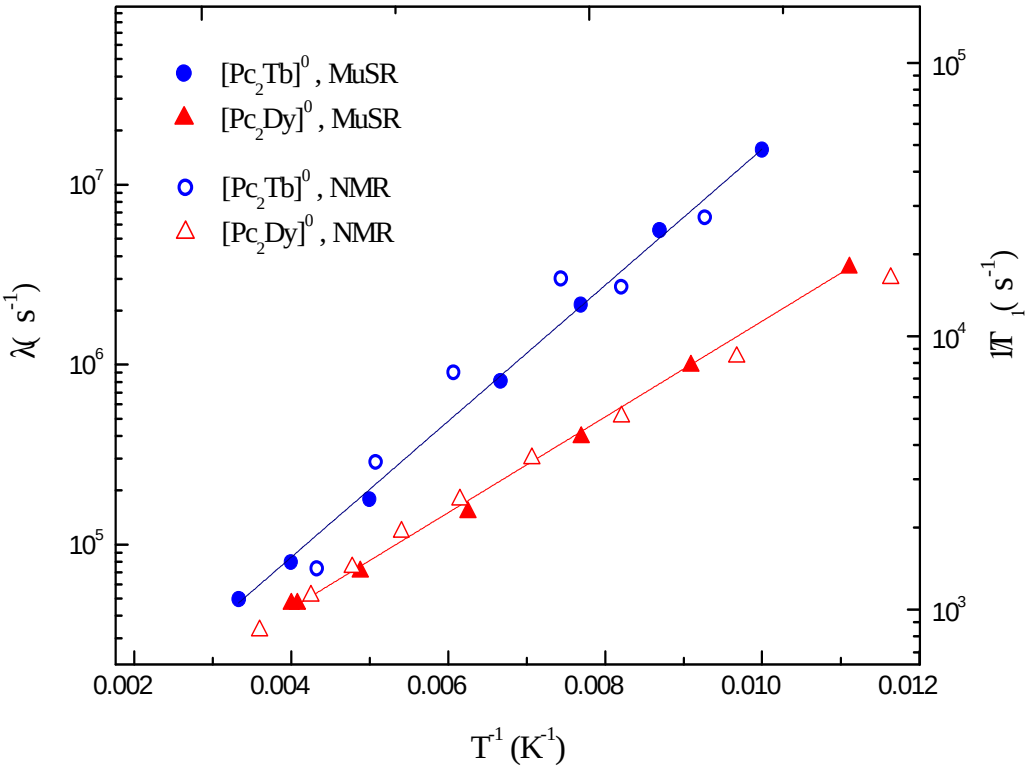

Figure 5.20: Muon and ^{1}H spin-lattice relaxation rates are reported as a function of inverse T in a semi-logarithmic plot in order to evidence the activated behavior for T > T*. The lines are the best fits yielding $\Delta E \simeq 881$ K for $[Pc_2\text{Tb}]^0$ and $\Delta E \simeq 610$ K for $[Pc_2\text{Dy}]^0$.

As happens in the diluted compounds, the correlation time shows two regimes. A high-T activated one and a low-T one, for T < 50 K, where the correlation time is constant. Again, the high-T behavior describes spin fluctuations among $m = \pm 6$ and $m = \pm 5$ levels, while the temperature independent trend at low T signals tunneling processes among $m = +6$ and $m = -6$ levels. The total fluctuation rate is given by the sum of the fluctuation rates associated with each process, according to Eq. (5.14). It is noticed that the tunneling rate is $(1/\tau_c)_{tunn} \simeq 11$ ms^{-1} already at T = 50 K, which is a record value for a molecular magnet. The correlation time behaviour with T was also deduced from experimental data taken in zero-field, by using Eqs (5.4-5.6) (Fig. 5.22). It is noticed that in the high T regime the τ_c derived in zero-field and in a 1000 Gauss longitudinal field are in satisfactory agreement and show an activated T-dependence. On the other hand, below 50 K, where tunneling processes become relevant, τ_c(T) is observed to flatten at values which differ by more than an order of magnitude upon increasing the field from zero to 1000 G. The increase of τ_c with the magnetic field intensity, also observed in the

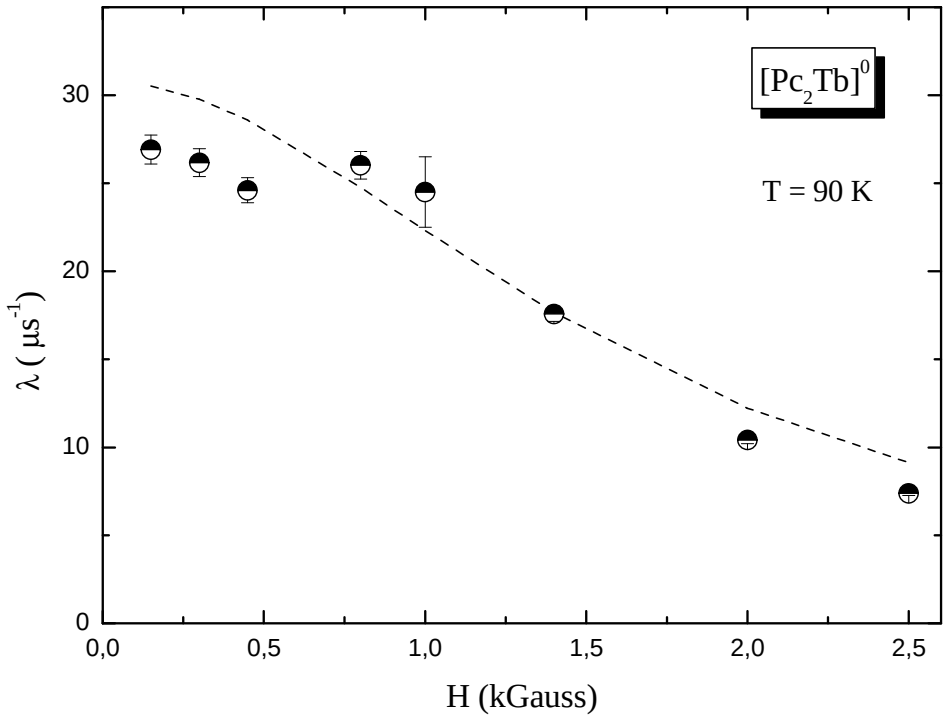

Figure 5.21: Field dependence of the muon spin-lattice relaxation rate λ measured at T = 90 K for $[Pc_2\mathrm{Tb}]^0$ compound. The dashed line represents the best fit to Eq. (5.12-5.13) for T = 90 K. The estimated energy barrier is $\Delta E \simeq$870 K.

AC-susceptibility measurements reported in Par. (3.4) of Chapter 3, should be ascribed to the removal of the ground-state degeneracy by the magnetic field, which progressively inhibits the tunneling processes. It is thus useful to compare NMR and μSR results in $[Pc_2\mathrm{Tb}]^0$ with AC susceptibility ones. As it is shown in Fig. (5.23), the T-dependence of τ_c derived by the two techniques at different magnetic fields overlaps rather well above 45 K and gives very similar values for the energy barrier. On the contrary, at lower temperatures the plateau associated with tunneling processes among the $|m = \pm 6\rangle$ low-energy levels lies at different values depending on the magnitude of the applied field and on the technique. Although the progressive increase of τ_c with magnetic field observed by each technique can be justified resorting to the removal of the ground state degeneracy by the external field, the significant difference in the τ_c values deduced by μSR (NMR) and AC susceptibility in the low-temperature tunneling regime cannot be explained in this way. In fact, the low-temperature tunneling dynamics probed at the microscopic or at the macroscopic level seem to be intrinsically different. This suggests that there are some correlations among the magnetic moments in the different molecular units which cause fluctuations which do not affect the total magnetization. This coupling should

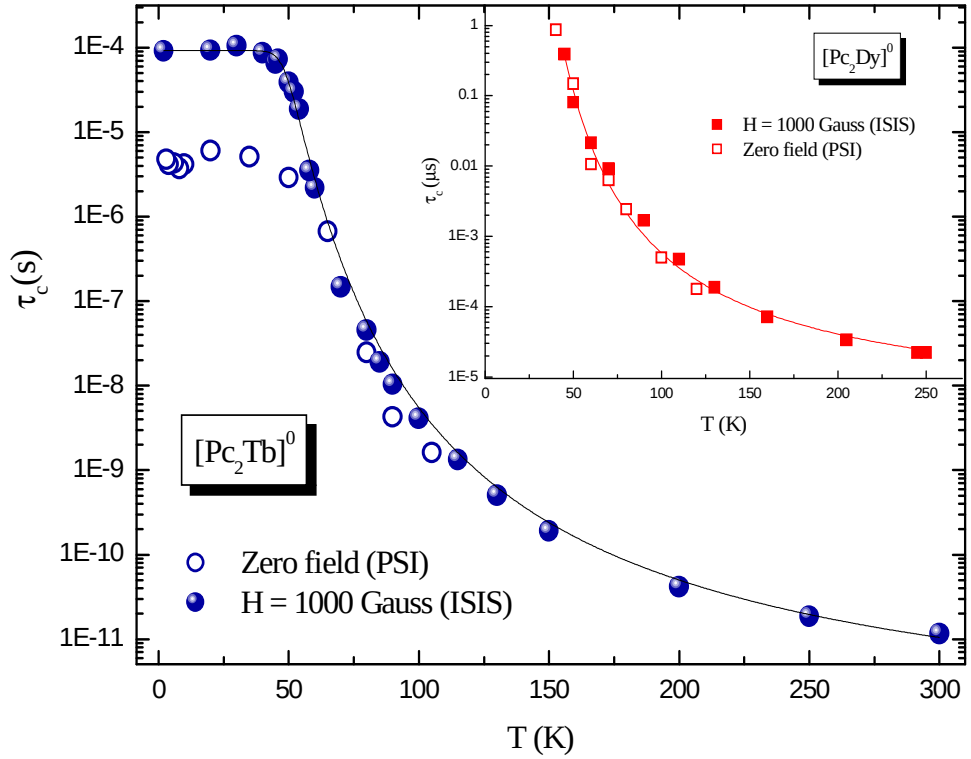

Figure 5.22: Temperature dependence of the correlation time for the spin fluctuations in $[Pc_2\mathrm{Tb}]^0$ and $[Pc_2\mathrm{Dy}]^0$ (in the inset, for T > T*) derived from λ data reported in Fig. (5.13) and (5.14) respectively.

lead to flip-flop like fluctuations [119] yielding a magnetic moment flip from $|m = +6\rangle$ to $|m = -6\rangle$ on one molecule and the opposite flip in the adjacent molecule. These processes, which cannot be accounted for by a direct dipolar coupling among Tb^{3+} spins since they produce a change $\Delta m = \pm 12$, do not yield a net variation in the total magnetization and, hence, do not contribute to the AC susceptibility. The precise nature of these fluctuations still has to be clarified.

As regard the temperature dependence in $[Pc_2\mathrm{Dy}]^0$, a maximum around T = 60 K can be observed (Fig. 5.14). If one tries to fit the data with Eqs (5.12-5.13), a good fit is found only for T > 40 K. Moreover, in the high-T regime the τ_c derived in zero-field and in 1000 Gauss longitudinal field are in satisfactory agreement and show an activated trend (Fig. 5.22, inset). The associated energy barrier for the spin fluctuations is estimated to be around 610 K, from both NMR and μSR high temperature data (Fig. 5.20), while the spin-phonon coupling constant C was found to be $\simeq 1780$ Hz/K^3. However, it can be noticed from Fig. (5.14) that for T<40 K the data are not so well reproduced. In fact, as derived from AC susceptibility data, in $[Pc_2\mathrm{Dy}]^0$ the two lowest doublets are separated by an energy barrier in the tens of K range, while the high barrier derived from λ(T) corresponds to the one between the first and second excited

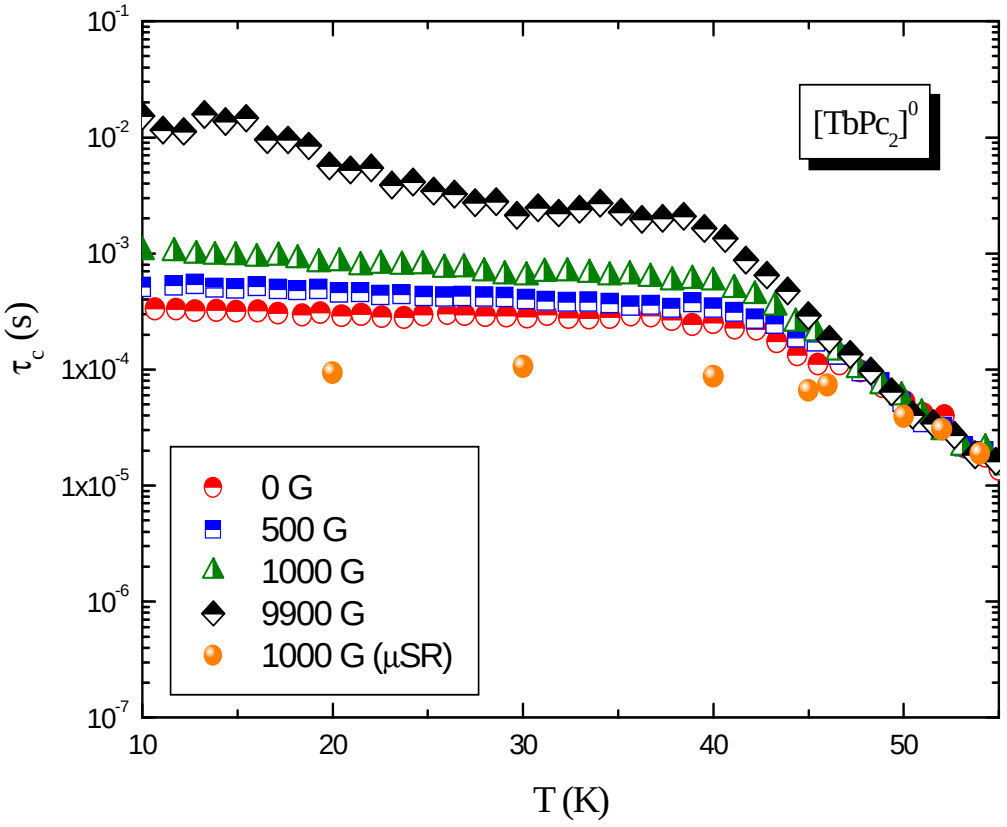

Figure 5.23: Temperature dependence of the correlation time τ_c for a static field of 0, 500, 1000, 4000 Gauss in $[Pc_2\mathrm{Tb}]^0$ compound, derived from AC susceptibility measurements. Solid circles correspond to τ_c temperature dependence as derived from μSR analysis for H = 1000 Gauss.

doublets. Hence, in order to appropriately fit the data one should resort to Eq. (5.9). However, even by allowing different possible values for the CF splitting a poor fit of the experimental data is obtained. On the contrary, the temperature dependent muon relaxation rate was correctly fit using Eqs. (5.9-5.11) by considering the CF level splitting previously estimated from χ_ST fit and by using three different spin-phonon constants (Fig. 5.14). In fact, it is likely that the spin-phonon coupling constant is not the same for the scattering processes yielding high and low-energy transitions. The values of the three spin-phonon couplings were estimated to be C_1, $C_2 \rightarrow 0$, while $C_3 \simeq 2000$ Hz/K^3 and should be associated with the transitions $|m = \pm 11/2\rangle \leftrightarrow |m = \pm 13/2\rangle$, $|m = \pm 9/2\rangle \leftrightarrow |m = \pm 11/2\rangle$ and $|m = \pm 15/2\rangle \leftrightarrow |m = \pm 13/2\rangle$, respectively. This suggests that the relevant processes driving the transitions preferentially involve high energy vibrational modes. In Fig.(5.14) it can noticed that the best fit according to Eq. (5.9) reproduces the muon relaxation data very well for T $>$ 25 K. Since in this model only the thermally activated spin excitations

	$\Delta E\,(K)$	$\tau_0\,(ps)$	$C\ (Hz/K^3)$
$[Pc_2Tb]^0$	880 ±15	0.49 ± 0.13	~3000
$[Pc_2Dy]^0$	610 ± 11	2.0 ± 0.9	~2000

Table 5.2: The table summarizes the most important parameters derived in neutral $[Pc_2\text{Ln}]^0$ compounds (Ln = Tb, Dy) from the analysis of the temperature dependence of muon spin-lattice relaxation rate λ.

are concerned, the behaviour of λ(T) below 25 K should be probably ascribed to different processes, for instance to the onset of intermolecular correlations. The estimates of ΔE, C and τ_c derived for the neutral compounds are summarized Table (5.2).

Chapter 6

Microscopic Properties of Neutral $[Pc_2\mathbf{Y}]^0\cdot\mathbf{CH_2Cl_2}$ System

Due to the closed shell electronic configuration of Yttrium(III) ion, the neutral $[Pc_2\mathrm{Y}]^0$ molecule does not belong to the class of molecular magnets and it thus requires a separate discussion. The microscopic properties of this system are mainly associated with the presence of an unpaired electron delocalized around the molecule, deriving from the one-electron oxidation of the $[Pc_2\mathrm{Y}]^-$ molecule. The two phthalocyanine rings of the neutral compound are in fact characterized by an open shell π configuration and the resulting 1/2-spin system is responsible of interesting phenomena such as the onset of antiferromagnetic (AF) correlations at low temperature and spin diffusion. In fact, as previously discussed in Chapter 3, the analysis of the static uniform susceptibility temperature dependence allowed to estimate an AF Curie-Waiss temperature $\theta = -5.37 \pm 0.04K$ and a Curie constant $C = 0.342$ ergK/G^2, very close to the value expected for a spin-1/2 AF. In addition, the magnetic properties were found to strongly depend on the degree of overlap between adjacent orbitals of the $[Pc_2\mathrm{Y}]^0$ molecules. Accordingly, it has been also shown in previous works that the spin diffusion in the yttrium bis-phthalocyanine compound depends on the stacking of the molecules [129], which is related with the crystalline structures of this material. In fact, depending on the preparation, two crystalline structures of this material are available, whether it is solvated or not. As it is shown in Fig. 6.1, the solvated system $[Pc_2\mathrm{Y}]\cdot\mathrm{CH_2Cl_2}$ shows a stacking of the molecules in parallel chains, while the unsolvated system $Pc_2\mathrm{Y}$ exhibits a stacking of parallel planes. In this chapter, ^{1}H NMR measurements in powders of the solvated, neutral $[Pc_2\mathrm{Y}]^0\cdot\mathrm{CH_2Cl_2}$ will be presented. The AF character of the spin-1/2 interactions arising at low temperature are confirmed by means of NMR paramagnetic shift analysis. Moreover, the temperature dependence of the ^{1}H spin-lattice relaxation rates ($1/\mathrm{T_1}$) allows to derive an estimate of the exchange energy which is compatible with the values previously determined and to verify the mono-dimensionality of the system under investigation.

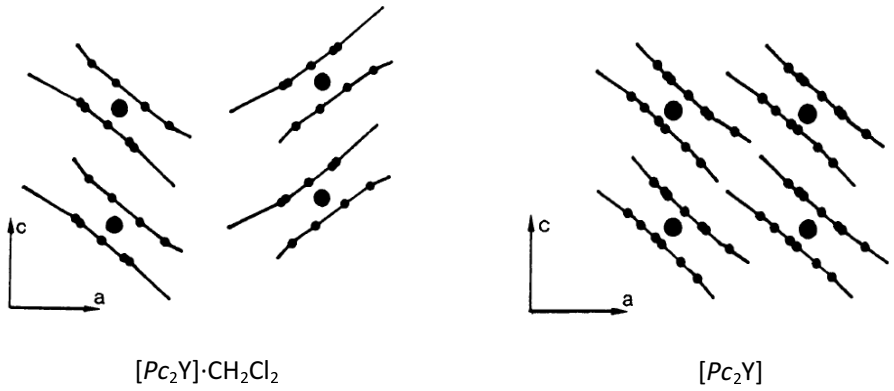

Figure 6.1: Schematic view of the crystal packing in the solvated $[Pc_2Y]\cdot CH_2Cl_2$ (left) and in the unsolvated Pc_2Y (right).

Finally, the $1/T_1$ field dependence is compatible with a 1D-spin diffusion and allows for the determination of the diffusion rate coefficient behaviour with temperature.

6.1 ^{1}H NMR in $[Pc_2Y]^0 \cdot CH_2Cl_2$ compound

6.1.1 ^{1}H NMR Spectra

The ^{1}H NMR spectra were obtained in the 10-300 K temperature range for the values H = 9 T, 1 T and 0.3 T of the applied field. The line-shape is gaussian in the whole investigated temperature range. The spectra were derived from the Fourier transform of half of the echo, if the full NMR line could be irradiated ($\Delta\nu < 60$ kHz), or from the envelope of the echo amplitude upon varying the irradiation frequency, in the opposite case. For H = 9 T and H = 1 T a line-broadening could be observed at low temperatures, which is more pronounced for the higher field intensity. On the other hand, for H = 0.3 K the line-width does not change significantly upon cooling (Fig. 6.2). This result indicates that the low temperature broadening of the spectra must be related to the presence of a strong field, rather than to the onset of a magnetic order at low temperatures. Moreover, the temperature dependence of the NMR paramagnetic shift $K = (\nu - \nu_0)/\nu_0$, due to the hyperfine interaction between the unpaired electron and protons, was detected for T = 9 T (Fig. 6.3). As expected, it was found to increase upon cooling, according to

$$K = \frac{A\chi_{mol}}{2\mu_B N_A} \quad , \tag{6.1}$$

namely the temperature dependence of ΔK should be the same of the macroscopic spin susceptibility. In fact, by plotting K as a function of χ_{mol} a linear trend is attained (Fig. 6.4). Then, the linear dependence of K vs χ_{mol} allows

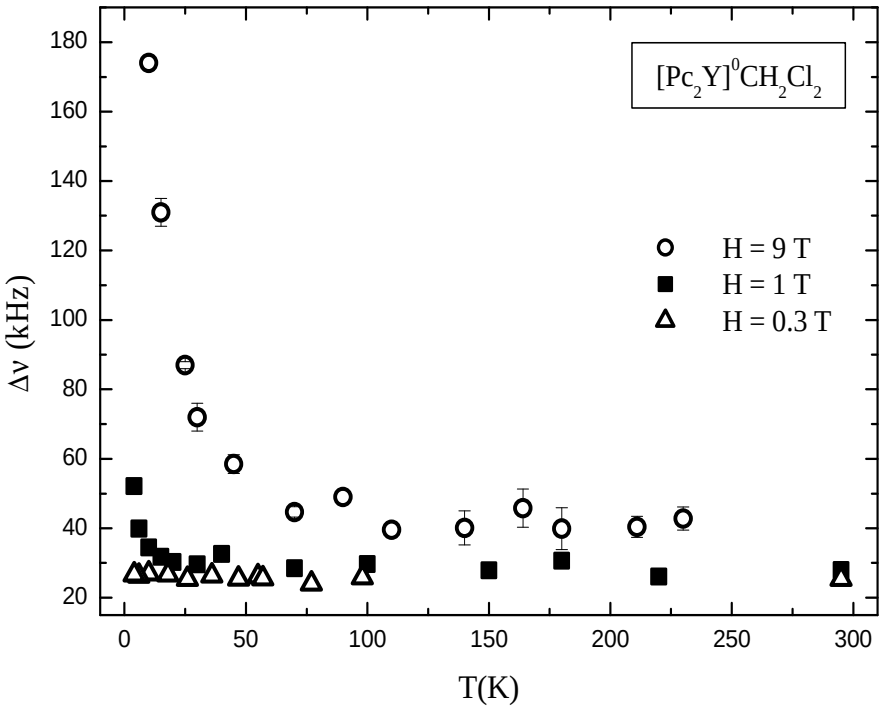

Figure 6.2: Line-width temperature dependence in powders of $[Pc_2Y]^0 \cdot CH_2Cl_2$, measured for different values of the applied field.

to estimate a hyperfine coupling constant $A \simeq 180$ Gauss, which in a powder sample must be interpreted as an average value of the different components of the hyperfine coupling tensor. In addition, by fitting the paramagnetic shift behaviour with temperature to the Curie-Waiss expression

$$K(T) = \frac{C_K}{(T-\theta)} \quad , \tag{6.2}$$

with $C_K = AC/(2\mu_B N_A)$, it is possible to derive an estimate of the Curie-Waiss temperature $\theta = -7.4$ K$\pm$0.3 K. This value is slightly smaller with respect to the one derived from the static susceptibility temperature dependence (θ = -5.37 K$\pm$0.04 K), discussed in Chapter 3, and it is a further confirmation of the onset of AF interactions at low temperatures. The small difference between those two type of measurements could be associated to a tiny amount of impurities which might affect the macroscopic susceptibility. Accordingly, the measurement of the microscopic susceptibility with paramagnetic shift measurements is expected to provide a more reliable estimate of the static uniform spin susceptibility and of the Curie-Weiss temperature.

6.1.2 ^{1}H NMR Spin-Lattice Relaxation Rate

The ^{1}H NMR spin-lattice relaxation rates $1/T_1$ were measured in powders of $[Pc_2Y]^0CH_2Cl_2$ in the 1.5 - 300 K temperature range and for different values of

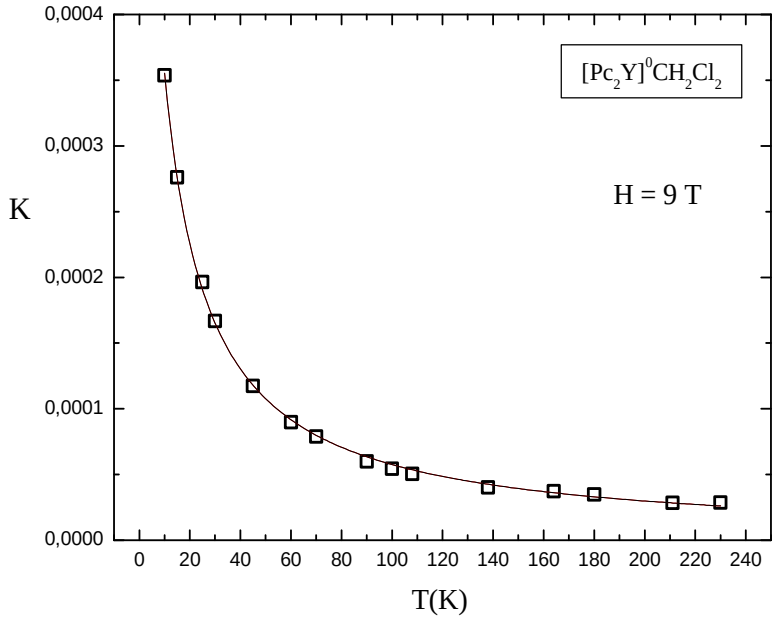

Figure 6.3: NMR paramagnetic shift K temperature dependence in $[Pc_2Y]^0 \cdot CH_2Cl_2$ compound, measured for H = 9 T. The solid line represents the best fit to equation $K(T) = C_K/(T - \theta)$, which gives the value for the Curie-Waiss temperature θ = -7.4 K ±0.3 K.

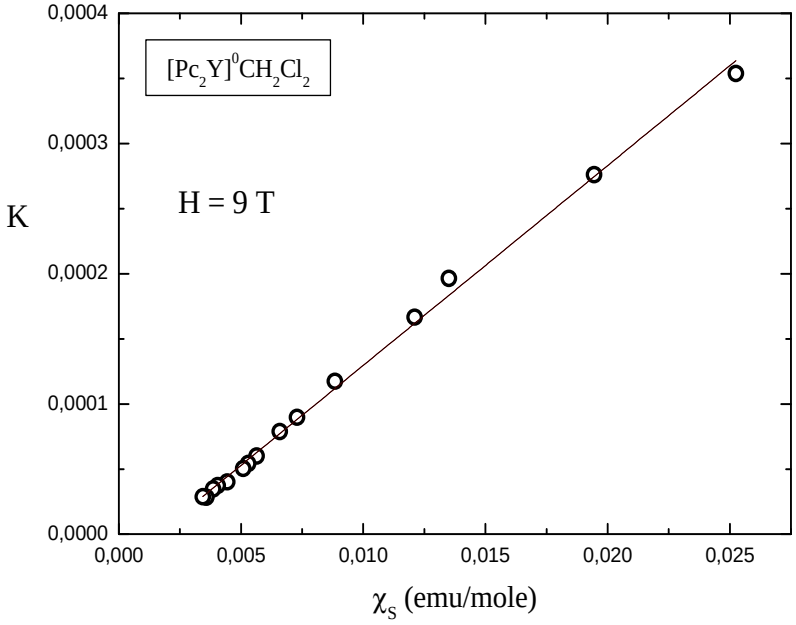

Figure 6.4: The paramagnetic shift K plotted as a function of the static susceptibility χ_S in $[Pc_2Y]^0 \cdot CH_2Cl_2$ sample. The solid line represents the best fit to Eq. (6.1). The estimated hyperfine constant is $A \simeq 180$ G.

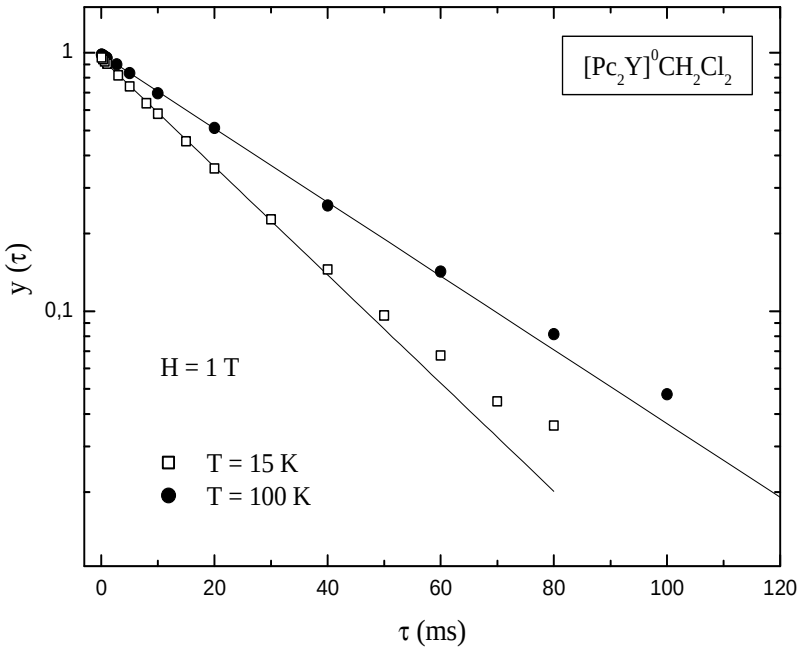

Figure 6.5: Recover of the nuclear magnetization as a function of the delay τ in the standard spin-echo sequence, recorded at two selected temperatures for $[Pc_2Y]^0 \cdot CH_2Cl_2$ compound. The recovery laws are fitted to a single exponential function (solid lines).

the external field. The $1/T_1$ were extracted from the recovery of nuclear magnetization after a saturation recovery pulse sequence ($y(\tau) = 1 - m(\tau)/m(\tau \rightarrow \infty)$). The recovery law was found to be a single exponential $exp(-\tau/T_1)$ in the whole explored temperature range (Fig. 6.5). This result is an evidence of the delocalized character of the unpaired electron around the molecule. In fact, since in the two phthalocyanine rings a large number of inequivalent proton sites is present, the single exponential behaviour of the recovery law suggests that the contact term of the hyperfine interaction must be dominant with respect to the dipolar one, yielding an almost isotropic hyperfine coupling tensor. Otherwise, a stretched exponential recovery of the magnetization should be expected. The temperature and field dependence of $1/T_1$ is shown in Fig. (6.6).

In the high temperature limit, e.g. when the thermal energy is much larger than the exchange energy ($T >> J_{ex} \equiv \theta$), the $1/T_1$ of a spin-1/2 paramagnet is temperature and field independent and it is given by Eq. (4.54) of Chapter 4, which is recalled below:

$$\frac{1}{T_1} = \frac{\gamma^2}{2}(A_x^2 + A_y^2)\frac{S(S+1)}{3}\frac{\sqrt{2}\pi}{\omega_{ex}} \tag{6.3}$$

By means of the measured $1/T_1$ at high temperature and by assuming $A_x^2 = A_y^2$, from Eq. (6.3) it is possible to derive an estimate of the exchange frequency $\omega_{ex} = (J_{ex}/\hbar)\sqrt{2zS(S+1)/3} \simeq 8.43 * 10^{11}$ s^{-1}rad, where $z = 2$ is the number

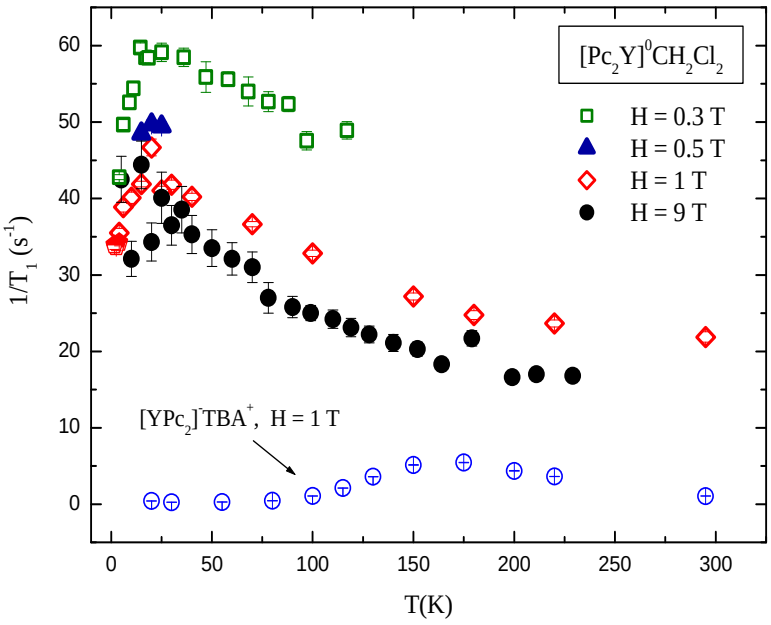

Figure 6.6: ^{1}H NMR spin-lattice relaxation rate temperature dependence for $[Pc_2Y]^0 \cdot CH_2Cl_2$ compound measured for different values of the applied field. The open circles represent the experimental data measured for the $[Pc_2Y]^-TBA^+$ sample in H = 1 T.

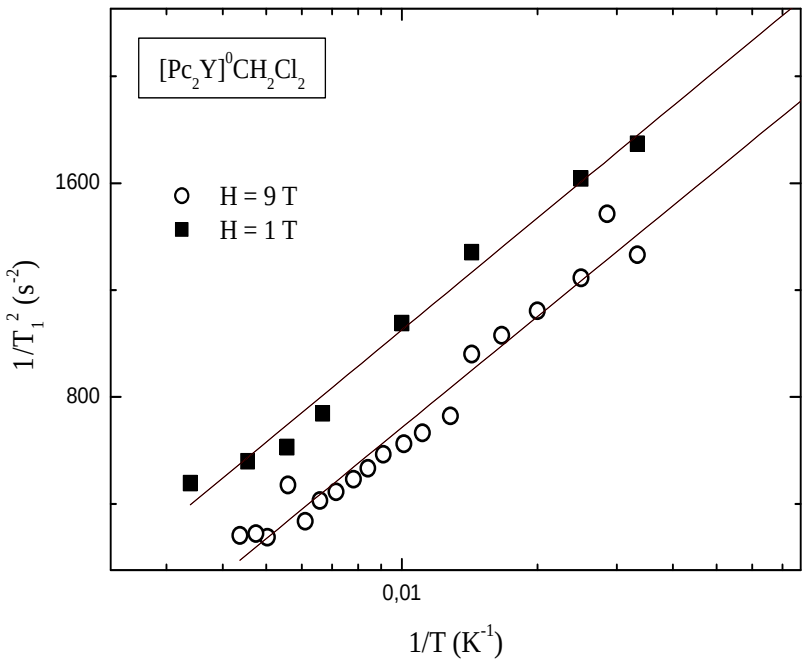

Figure 6.7: The $1/T_1$ squared is plotted as a function of T^{-1}, in a logarithmic scale for two values of the external field (H = 9 T, circles and H = 1 T, squares). The solid lines represent the best fits to Eq. (6.6)

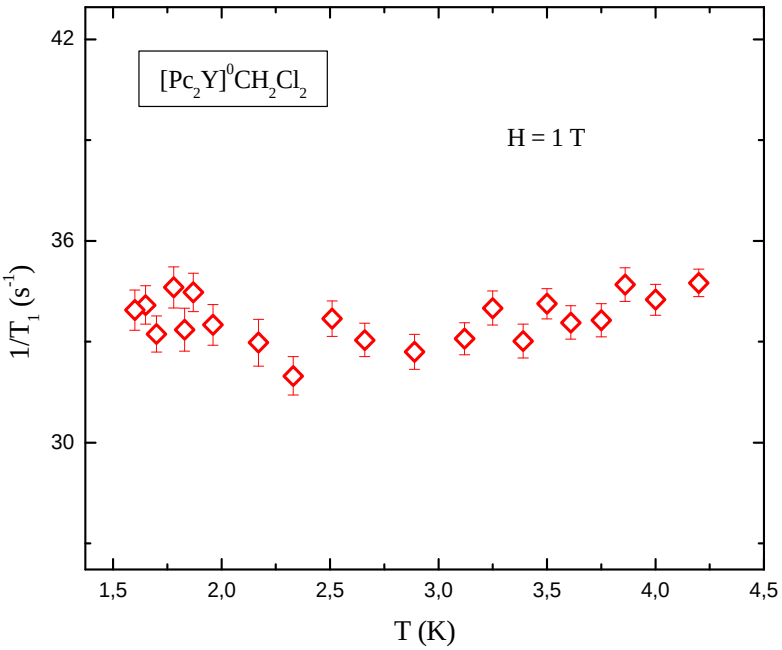

Figure 6.8: Spin-lattice relaxation rate temperature dependence measured in the 1.5 K-4.2 K range and for H = 1 T in $[Pc_2Y]^0 \cdot CH_2Cl_2$ compound.

of first neighbours. This value corresponds to an exchange constant $J_{ex} \simeq$ 6.4 K, which is compatible with the results obtained previously by means of different analysis.

On the other hand, when collective spin excitations are present and for a 1D chain, the $1/T_1$ follows the expression (see Eq. 4.56)

$$1/T_1 = \frac{\gamma^2}{2N} \sum_{q,\alpha} \left(|A_q|^2 \frac{\mathrm{Im}\chi_{\alpha\alpha}(q,\omega_0)}{\omega_0} \right)_{\perp} \qquad \alpha = x,y,z \quad , \tag{6.4}$$

where $\chi_{\alpha\alpha}(q,\omega)$ is the dynamic susceptibility per spin in units of $(g\mu_B)^2$ and $|A(q)|^2 = |\sum_i A^i_\alpha exp(iqr_i)|^2$ is the form factor giving the hyperfine coupling of the nuclei with the spin excitations at wave-vector q. An analytic result for $\chi(q,\omega)$ at finite temperatures was first obtained by Shultz [130] by using the bosonization technique to transform the spin-1/2 one-dimensional AF Heisemberg model

$$\mathcal{H} = J_{ex} \sum_i \mathbf{S_i} \cdot \mathbf{S_{i+1}} \quad , \tag{6.5}$$

to a free boson hamiltonian. However, this method furnishes a temperature independent $1/T_1$, which does not allow to correctly reproduce the experimental data below T = 200 K. The measured $1/T_1$ is instead well reproduced in the temperature range 30 K - 200 K by the expression [131]

$$1/T_1 \propto ln^{1/2}(T_0/T) \quad , \tag{6.6}$$

where T_0 is the high energy cutoff, which is expected to be of the order of J_{ex}. Eq. (6.6) was derived by considering the operator describing umklapping scattering processes in the original Heisemberg hamiltonian, which is neglected by the free boson theory [132]. In Fig. (6.7) the linear dependence of $(1/T_1)^2$ vs $ln(T_0/T)$ is shown for the two values of the applied field H = 9 T and H = 1 T. By modeling the experimental data with Eq. (6.6) the constant T_0 was estimated to be $\simeq 3$ K, in agreement with the theory.
At about 20 K a peak in the nuclear relaxation rate appears (Fig. 6.6), whose intensity decreases by increasing the external field. On the other hand, below T = 5 K, the $1/T_1$ is nearly temperature independent (Fig. 6.8). The maximum in $1/T_1$ could be associated with the presence of a form factor, which partially filters out the antiferromagnetic fluctuations as the system gets more and more correlated. In Fig. (6.6), the temperature dependence of the $1/T_1$ measured in the $[Pc_2Y]^-TBA^+$ compound for H = 1 T is also shown for comparison. As expected, in the anionic compound the absence of the 1/2-spin system associated with the unpaired electron yields much slower relaxation rates with respect to the neutral form. The broad peak in the $1/T_1$ at around T = 160 K must be probably related to weak molecular dynamics, whose frequency is close to Larmor frequency at the peak temperature.

In the presence of one-dimensional AF interactions, the electronic spin diffusion is the dominant process of the nuclear relaxation. Thus, in order to investigate the temperature dependence of the spin diffusion coefficient in $[Pc_2Y]^0 \cdot CH_2Cl_2$ compound, the field dependence of $1/T_1$ was measured for different selected temperatures (Fig. 6.9). The proton relaxation rate is indeed expected to depend on the spectral density $J(\omega)$ of the spin excitations according to the following equation [133]:

$$\frac{1}{T_1} = \frac{\gamma^2}{2} \frac{k_B T \chi_0}{(g\mu_B)^2} \left[\frac{3}{5} A_d^2 J(\omega_0, D) + \left(A_a^2 + \frac{7}{5} A_d^2 \right) J(\omega_e, D) \right] \quad , \tag{6.7}$$

where A_d and A_a are the dipolar and isotropic hyperfine coupling constants, respectively, χ_0 is the the static uniform susceptibility per spin and $\omega_e = \omega_0 \gamma_e / \gamma$ is the electronic resonance frequency. Moreover, in a one dimensional system, the spectral density is characterized by a low-frequency divergence given by the expression [111]

$$J(\omega, \omega_c, D) = \frac{1}{\sqrt{2D}} \left(\frac{\omega_c + \sqrt{\omega^2 + \omega_c^2}}{\omega^2 + \omega_c^2} \right)^{1/2} \quad , \tag{6.8}$$

where ω_c is a low-frequency cutoff accounting for the finite spin anisotropy and/or inter-chain coupling and D is the spin diffusion rate. Depending on the spectral width at which the electronic spin diffusion takes place and on the value of ω_c compared to that of ω_0 and ω_e, three different situations can occur for the frequency dependence of the spectral density, which therefore lead to three different frequency dependence of the proton relaxation rate. If $\omega_c < \omega_0 < D < \omega_e$, e.g. the $1/T_1$ probes the spectral density at ω_0 only,

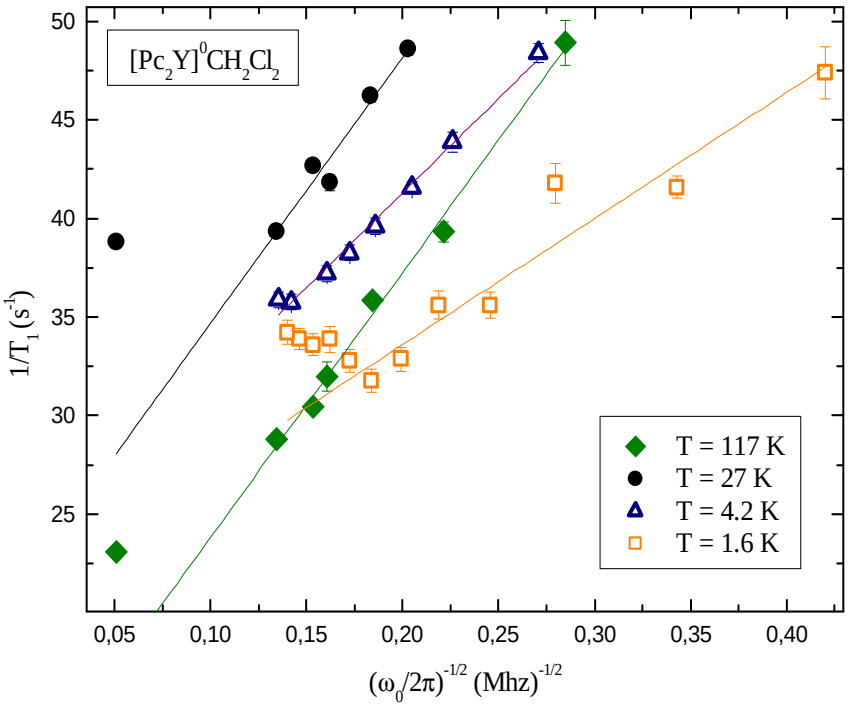

Figure 6.9: The ^{1}H spin-lattice relaxation time $1/T_1$ is plotted as a function of $\nu^{-1/2}$ for different selected temperatures in $[Pc_2Y]^0 \cdot CH_2Cl_2$ compound. From the slopes of the lines the temperature dependence of the diffusion rate was derived (see text).

or if $\omega_c < \omega_0 < \omega_e < D$, e.g. the $1/T_1$ depends on both $J(\omega_0)$ and $J(\omega_e)$, the relaxation rate is directly proportional to $J(\omega)$. On the other hand, if $\omega_0 < \omega_c < \omega_e < D$, the spectral density at ω_0 is temperature independent, leading to a non-zero extrapolation of the T_1^{-1} vs $\omega^{-1/2}$ plot. In Fig. (6.9), the $1/T_1$ is plotted as a function of $\nu_0^{-1/2}$. The observed linear trend further proves the mono-dimensionality of the AF interactions, which occur along the chains. Moreover, the non-zero intercept in the $1/T_1$ plot indicates that spin diffusion occurs in the electronic frequency range only. This means that during the nuclear relaxation process a simultaneous flip of the electron and nuclear spins occur, involving an energy exchange $\hbar(\omega_e \pm \omega_0)$, and $1/T_1$ thus probes the spin excitations at a frequency close to ω_e. Thus, from the slopes of the curves it is possible to deduce the spin diffusion coefficient at different temperatures (Fig. 6.10), assuming $J(\omega_0) \approx$ const, $A_d \simeq 0$, $A_a \simeq 180$ Gauss and neglecting $\omega_c << \omega_e$ in Eqs (6.7-6.8). At low temperatures, the estimated spin diffusion coefficient is of the order of the exchange frequency ω_{ex}, as one should expect, while it is found to progressively decrease with temperature and to become nearly constant above 20 K. This result should probably be related to the onset of inter-chain interaction, which break the mono-dimensionality of the AF correlations.

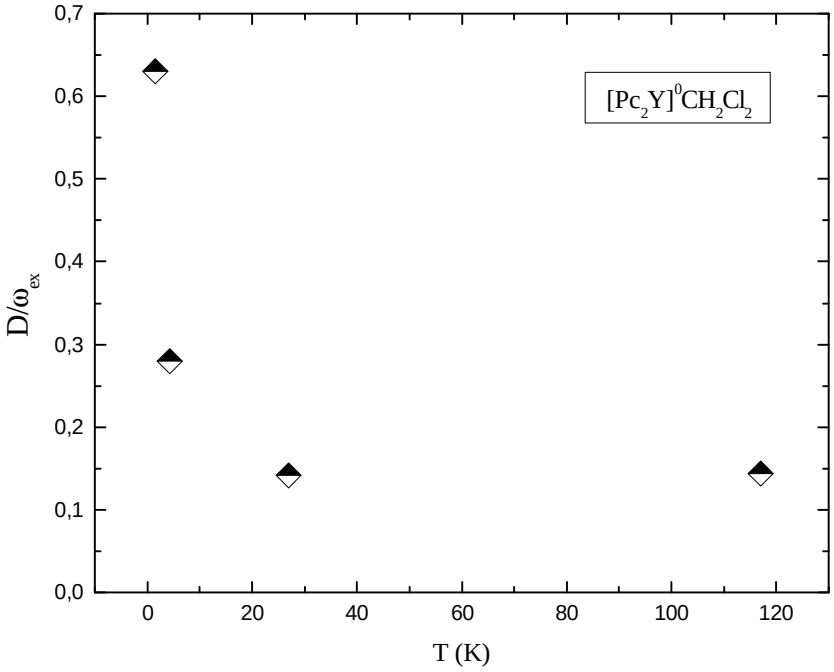

Figure 6.10: Temperature dependence of the ratio D/ω_{ex} between the spin diffusion coefficient D and the exchange frequency $\omega_{ex} = 9.4 \cdot 10^{11}$ s^{-1}rad in $[Pc_2Y]^0 \cdot CH_2Cl_2$ compound. The spin diffusion coefficient behaviour with T was derived from the slopes in the $1/T_1$ vs $\nu_0^{-1/2}$ plots (Fig. 6.9) and from Eq. (6.7) by assuming $J(\omega_0)$= const.

Chapter 7

Conclusions and future perspectives

In this work the magnetic properties of a series of bis-phthalocyaninato lanthanide (III) compounds Pc_2Ln have been discussed. These materials have been recently discovered to behave as Single Molecule Magnets (SMMs), showing the phenomena of slow relaxation and quantum tunneling of magnetization, which are two of the peculiar features of SMMs. Especially, the terbium and dysprosium complexes have been recognized as the most interesting materials belonging to the Single Ion Magnets (SIM) category, thanks to their extremely large magnetic anisotropy. The experimental investigation of Pc_2Ln-based (Ln = Tb, Dy) compounds has mainly focused on the study of the *f*-metal ion spin dynamics, which have been carried out by means of solid-state ^{1}H NMR and μSR microscopic techniques and of macroscopic DC and AC magnetization experiments. The final goal of this study has been the determination of the temperature dependence of the electronic spin correlation times of the compounds under investigation, in order to evaluate the effective applicability of these SIM units in operational magnetic device elements. The measurements have been carried out on three differently diamagnetically diluted samples, $[Pc_2\text{Tb}]^-[\text{TBA}]^+$ (**1**), $[Pc_2\text{Tb}]^-[\text{TBA}]^+ \times 9[\text{TBA}]\text{Br}$ (**2**), and $[Pc_2\text{Tb}]^-[\text{TBA}]^+ \times 143[\text{TBA}]\text{Br}$ (**3**) and on the neutral $[Pc_2\text{Tb}]^0$ and $[Pc_2\text{Dy}]^0$ compounds. In addition, ^{1}H NMR and static uniform susceptibility measurements in the solvated, neutral $[Pc_2\text{Y}]^0\text{CH}_2\text{Cl}_2$ have been performed, in order to probe the low temperature correlations arising among the electrons delocalized around the Pc_2Y molecules.

7.1 $[Pc_2\text{Tb}]^-[\text{TBA}]^+_N$ Molecular Magnets

By means of ^{1}H NMR, the energy barrier to spin reversal ΔE of the diluted compound (**2**) and (**3**) was found much larger ($\simeq$923 K and $\simeq$833 K) with respect to that previously estimated by Ishikawa and collaborators for the

undiluted $[Pc_2\mathrm{Tb}]^-[\mathrm{TBA}]^+$ system ($\simeq$628 K), by means of indirect measurements [47]. Moreover, it could be shown that the barrier height and tunneling rates depend on the magnetic dilution employed, indicating that the presence of TBA^+ molecules yields an increase in the crystal field at the rare-earth ion site and thus a much higher magnetic anisotropy. In addition, the spin dynamics of the diamagnetically diluted $[Pc_2\mathrm{Tb}]^-$ molecules in the samples (**2**) and (**3**) were affected by their magneto-thermal history, suggesting that even the diamagnetic matrix arrangement around (**2**) and (**3**) can perturb the splitting of the crystal field levels. It must be remarked that the most diluted compound (**3**) possesses the highest energy barrier ever achieved in a molecular magnet. However, as one can expect from the estimated value of τ_0 ($\sim 10^{-12}$ s), very high τ_c at low temperature are prevented by the large mixing between spin levels, which favors tunneling transition among the two lowest levels $|m = \pm 6\rangle$. This yields a shortening of the correlation time at low temperatures which is, below 4 K, several order of magnitude smaller than that measured in $\mathrm{Mn_6O_6}$ SMM. With this respect, $\mathrm{Mn_6O_6}$ is still the record SMM since its magnetization relaxation time reaches several month at about 2 K [29]. It is to notice that in all these compounds, the spin-phonon coupling constant was found to be about 2 order of magnitude smaller than the one of $\mathrm{Mn_{12}O_{12}}$ and one order of magnitude smaller with respect to $\mathrm{Mn_6O_6}$ [29] [30], indicating that in $[Pc_2\mathrm{Tb}]^-[\mathrm{TBA}]_N^+$ the high temperature life-time of crystal levels is much longer with respect to the transition metal compound, which is of major interest in view of the future applicability of rare-earth SMM in electronic devices.
On the other hand, in undiluted (**1**) NMR experiments allowed to estimate the value $\Delta E \simeq 840$ K, much higher than the one estimated by Ishikawa in the same nominal compound by means of indirect measurements and a spin-phonon coupling constant of about 5000 $\mathrm{Hz/K^3}$.

7.2 $[Pc_2\mathrm{Ln}]^0$ Molecular Magnets

In the neutral $[Pc_2\mathrm{Tb}]^0$ the energy barrier to spin reversal, derived by means of both NMR and μSR, is $\Delta E \simeq 880$ K. Remarkably, the characteristic correlation time for spin fluctuations was found to be almost 2 orders of magnitude larger with respect to diluted compounds for T < 50 K. In fact, in the neutral compound τ_c reaches 100 μs already at 50 K, which represents a record value for a SMM. This suggests that the different structural arrangement around the $Pc_2\mathrm{Tb}$ molecule due to the absence of TBA^+ matrixes leads to an enhancement of the CF symmetry and to a decrease in the quantum fluctuations within the twofold degenerate ground state. Moreover, the unpaired π electron resulting from the one-electron oxidation and resonating between the Pc molecules, yields a compression of the cage around the Tb^{3+} ion, which induces an increase in the CF field with respect to the undiluted compound (**1**). Thus, it appears to be of major relevance, in order to enhance τ_c and to be able to

employ SMM at economically affordable temperatures, to further investigate the effect of the modifications in the SMM coordination on the spin dynamics. On the other hand, in $[Pc_2\text{Tb}]^0$ compound the spin-phonon coupling was found to be $\simeq 3000$ Hz/K^3, yielding a correlation time about one order of magnitude smaller with respect to the diluted compound above 100 K. Remarkably, the estimates of the anisotropy barrier and of the correlation time behaviour with temperature derived by means of AC susceptibility measurements are compatible with those derived by means of microscopic techniques. In fact, it was shown that both AC susceptibility and μSR (NMR) probe a high T activated spin dynamics in neutral $[Pc_2\text{Ln}]^0$ molecular magnets, characterized by quantitatively similar correlation times. Moreover, the estimated energy barrier is much higher with respect to that derived by Ishikawa in the same nominal compound ($\Delta E \simeq 590$ K) [49]. At low temperature both techniques exhibit a flattening of the correlation time which is associated with tunneling processes. Nevertheless, from μSR one estimates correlation times which are one order of magnitude shorter than the ones derived by AC susceptibility measurements. This discrepancy between microscopic and macroscopic techniques indicates that there must be some correlations among Tb^{3+} moments, which cause fluctuations which do not contribute to the uniform macroscopic susceptibility. In addition, in the neutral $[Pc_2\text{Tb}]^0$ the Raman spectra measurements are compatible with the presence of very high energy vibrational modes associated with intramolecular bonds, which therefore should be responsible of spin transition. However, the complexity of such Raman spectra due to the large number of atoms within each Pc_2Tb molecule, also confirmed by specific heat experiments revealing the presence of a large number of optical branches, so far has prevented to establish a precise correspondence between vibrational modes and spin transitions. Moreover, the analysis of specific heat behaviour at low temperature evidenced the low-dimensionality of the crystal lattice , showing the trend $C \simeq T^{1.68}$, typical of quasi-1D systems.
As regard the neutral $[Pc_2\text{Dy}]^0$, the analysis of the static and dynamic uniform susceptibility and of the μSR (NMR) relaxation rates allowed for a better characterization of the CF splitting of the J = 15/2 multiplet and of the spin-phonon couplings driving the activated dynamics in this compound. By means of both DC and AC susceptibility measurements it was possible to estimate the same value of the energy separation between the twofold ground levels and first excited states, which is $\simeq 65$ K. On the other hand, μSR and NMR probe the same high temperature activated trend of the spin fluctuation, corresponding to an energy barrier of about 610 K. It was also demonstrated that in $[Pc_2\text{Dy}]^0$ the spin-phonon coupling constant is not the same for the scattering processes yielding high and low-energy transitions. In fact, the high-energy transition are associated with spin-phonon interaction of the same order of magnitude of neutral Tb-based compound (C$\simeq$ 1780 Hz/K^3), while the low-energy coupling constants are almost negligible. Even in this case, the estimated barrier was found to be much higher than that derived in the anionic form $[Pc_2\text{Dy}]^-[\text{TBA}]^+$

	$\Delta E\ (K)$	$\tau_0\ (ps)$	$C\ (Hz/K^3)$
$[Pc_2Tb]^-TBA^+_{144}$	923 ± 12 (NMR)	4.4 ± 0.2	~290
$[Pc_2Tb]^-TBA^+_{10}$	833 ± 48 (NMR)	8.4 ± 0.4	~206
$[Pc_2Tb]^-TBA^+$	840 ± 50 (NMR)	0.30 ± 0.09	~5600
$[Pc_2Tb]^0$	880 ± 15 (μSR)	0.49 ± 0.13	~3000
	750 ± 35 (χ_{AC})	~1	~2400
$[Pc_2Dy]^0$	610 ± 11 (μSR)	2.0 ± 0.9	~1780
Mn_6O_2	~86	~200	~1310
$Mn_{12}O_{12}$	≤74	≥ 30	~9×10^4

Table 7.1: The table summarizes the most important parameters derived in $[Pc_2Ln]$-based molecular magnets by means of ^{1}H NMR, μSR and AC susceptibility measurements.

in previous works [47].
In Table (7.1) the most significant results presented in this work are resumed, together with those derived for Mn_6O_6 and $Mn_{12}O_{12}$ transition metal molecular magnets. Noteworthy, in all the compounds under investigation the anisotropy barriers to spin reversal are at least one order of magnitude larger than in any other SMM system. This result points out the great advantages of using rare-earth SMMs, which seem to be the most promising candidates to be used in electronic devices.

7.3 $[Pc_2Y]^0 \cdot CH_2Cl_2$

The solvated, neutral $[Pc_2Y]^0 \cdot CH_2Cl_2$ microscopic properties were investigated by means of magnetization and ^1H NMR measurements. As a consequence of the one-electron oxidation of the closed shell system $[Pc_2Y]^-$, the molecules of this material are 1/2-spin π-radicals and the magnetic properties of the compound must be therefore ascribed to the presence of the unpaired electron delocalized around the molecule, as well as to the mono-dimensionality of the crystalline structure. The onset of 1/2-spin antiferromagnetic interactions at low temperatures was proved by means of the analysis of both the static uniform susceptibility and the ^1H NMR paramagnetic shift. Indeed, they were found to follow the Curie-Waiss (CW) law with an estimated Curie constant very close to the value expected for a 1/2-spin system and a CW temperature in the range (-5 K, -7 K). This result is also compatible with the estimate of the exchange frequency ($\omega_{ex} \simeq 8.4 \cdot 10^{11}$ s^{-1}rad) derived from the analysis of the proton spin-lattice relaxation rate in the high temperature limit $k_BT \gg J_{ex}$. The hyperfine coupling constant was found to be strongly isotropic, in agreement with the delocalized character of the unpaired electron around each $[Pc_2Y]^0$ molecule and it is of the order of 180 Gauss. The spin diffusion was qualitatively estimated by a study of the proton NMR relaxation rates as a function of the applied magnetic field. As expected, the $[Pc_2Y]^0 \cdot CH_2Cl_2$ behaves as a quasi one-dimensional system with a low temperature diffusion coefficient of the order of the exchange frequency ($D \simeq 7.5 \cdot 10^{11}$ s^{-1}rad). However, the onset of inter-chain correlations on heating is evidenced by the sharp drop of D above 10 K.

7.4 Future Perspective and Open Questions

Although the discovery of rare-earth molecular magnets certainly represents a step forward in searching materials with ever longer spin correlation times, thanks to the incomparably high magnetic anisotropy of this new class of materials, the use of Pc_2Ln-based SMMs in molecular devices working at reasonable environmental conditions (high temperature, low vacuum, etc...) requires a further improvement in the blocking temperature. This latter can be increased through the control and the chemical modification of the crystal field at the rare-earth ion, which mainly determines the magnetic anisotropy. In addition, further theoretical and experimental investigations are necessary to better understand the relaxation mechanisms responsible for the decoherence processes, in particular identifying the actual Raman vibrational modes driving the magnetization reversal, in order to confirm that the corresponding spin transition definitely occurs through the first excited states rather than any higher ones. On the other hand, since the development of bistable magnetic molecules with improved chemical and physical properties has been successfully reached, the main challenge towards a new limit of miniaturization remains now to address

single molecules, and to study their individual physical properties through direct methods. In fact, if bistable magnetic molecules can be magnetically addressed, their magnetic anisotropy could be used for information storage and information transfer. The possibility to switch a single molecule electronic state under certain environmental conditions and to determine ("write") and control ("read") the electronic state through different magnetic/transport/spectroscopic probes still needs to be demonstrated. On the other hand, the single-molecule addressing requires the technological effort to design the molecules with the right characteristics for controlled organization on solid supports, which is a requirement for the further application into devices. In the last years, several techniques have been implemented for the fixation of functionalized single molecules onto solid supports, designing and controlling the molecule-host interactions through the convenient use of functional groups, in order to retain the molecular bistability. Indeed, the anchoring of functionalized [Pc_2Ln] SMMs onto single walled carbon nanotubes and onto Cu(111) surface has already been achieved [62][52] and the results confirm that the SMM behavior is indeed preserved. This strategy will be hopefully extended to other SMM-host interactions directed to other types of solid supports. The synergy between embedded magnetic nodes into a conducting matrix could give rise to useful interactions between localized electrons and itinerant electrons: the magnetic state of the magnetic nodes could modify the transport properties of the conducting network, yielding a magnetoresistance effect. At the same time, the electric current could serve to read(write)-out the state of the magnetic bits. Since in the case of SMMs the switching at the molecular level is expected to be controlled by an external magnetic field and it would be "read" either by magnetization measurements or by transport measurements, different techniques will be used in the next future to study and control the molecular electronic states, from the nanoSQUID technology for susceptibility measurements to spin sensitive scanning probe techniques, allowing for transport and spectroscopic experiments.

Chapter 8

Appendix

8.1 Chemical and Structural Details

8.1.1 Preparation of $[Pc_2\mathbf{Tb}]^-[\mathbf{TBA}]^+$ (1)

In a round-bottomed flask were mixed dicyanobenzene (32.0 mmol, 4.1 g), terbium acetoacetate (2.0 mmol, 0.64 g) in hexanol (50 mL), DBU (16.0 mmol, 2.4 mL), and acatalytic amount of benzyl-triethylamonium chloride (30 mg, 0.13 mmol). The reaction was performed in a microwave oven using an applied microwave power of 450 W for 10 min, followed by longer irradiation (15 min) at lower energy (300 W). The blue mixture was cooled down to rt and kept in the cold (4 °C) overnight. The dense solution was filtered using a glass frit and the residue collected. In order to remove as much n-hexanol as possible, the precipitate was further washed on frit with portions of cold n-heptane (5 × 50 mL). Then the products $[Pc_2Tb]^-$ (blue) and $[Pc_2Tb]^0$ neutral (green) were extracted from the residue, using a mixture of $MeOH/CH_2Cl_2$ (200 mL, 50 mL, 4 °C), while most of the phthalocyanine ring (violet, very shiny needles) remained in this way on the filter. The solution was evaporated to dryness under reduced pressure which afforded formation of an oily blue-green residue. Addition of CH_2Cl_2 (30 mL) followed by hexane (400 mL) allowed slow formation of a fine, bluish precipitate after 30 min that was collected while the yellow-greenish solution was filtered off. This procedure was repeated three times. Purification of $[Pc_2Tb]^-$ was performed by nitrogen-saturated flash chromatography on an Al_2O_3 (basic) column where at first CH_2Cl_2 was used as eluent to remove remaining yellowish side products followed by CH_2Cl_2/MeOH (2/1, v/v). The product $[Pc_2Tb]^-$ was then eluted by addition of sodium methanoate (NaOMe) using only MeOH as eluting solvent. The blue fraction collected was quickly evaporated to dryness under reduced pressure and kept under nitrogen. Further purification of $[Pc_2Tb]^-$ was carried out by size-exclusion chromatography using Sephadex LH_20 with $MeOH/CH_2Cl_2$ as eluent mixture (1/1, v/v). Residual bluish compounds re-

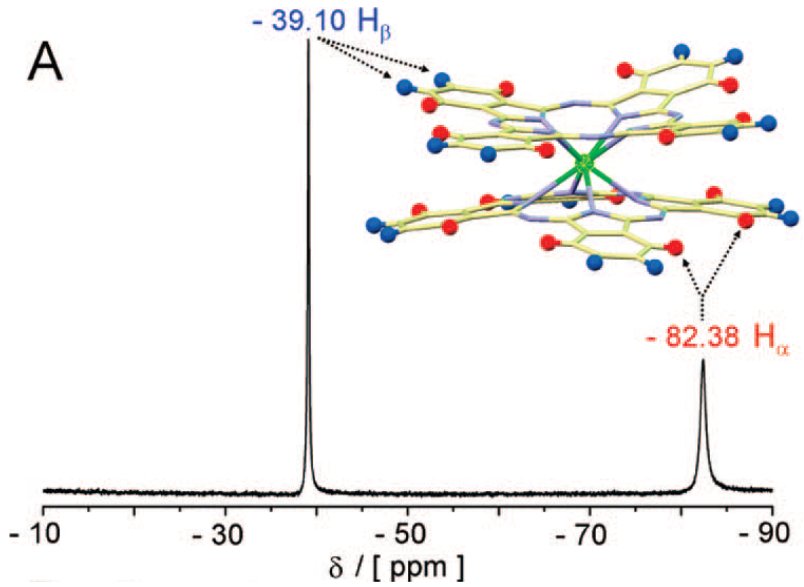

Figure 8.1: ^{1}H NMR spectrum of $[Pc_2Tb]^-[TBA]^+$ (**1**) recorded in CD_3CN showing the chemical shifts for the H_α and H_β protons of the phthalocyanine rings.

mained trapped in the column. The blue solution was quickly evaporated under reduced pressure, affording the negatively charged product in the form of a very hygroscopic dark-blue powder (0.56 g, 0.47 mmol, yield 6%) which still contained one solvent molecule (n-hexanol) and where most probably an acid/water molecule acted as countercation. Tetrabutylammonium bromide (0.47 mmol, 0.153 g) was added to the blue solid $[Pc_2Tb]^-$ together with 50 mL of MeOH; the resulting deep-blue solution was then stirred vigorously under nitrogen for 5 min. Most of the solvent ($\sim$ 45 mL) was removed under vacuum, and cold hexane was added (100 mL). A dark-blue precipitate immediately formed, which was collected and dried in vacuum (0.1 mbar) at rt for one day and then stored under nitrogen (664 mg). The bulk magnetic properties of this sample were measured and found to be analogous to those already described by Ishikawa and co-workers[32].

8.1.2 Spectroscopic Characterization of $[Pc_2Tb]^-[TBA]^+$

The paramagnetic ^{1}H NMR spectrum of $[Pc_2Tb]^-[TBA]^+$ in solution is presented in Fig. (8.1) . The experimentally observed dipolar shifts for R-protons (- 82.38 δ/ppm, H_α) and β-protons (- 39.10 δ/ppm, H_β) of the phthalocyanine cores were well resolved in CD_3CN, in close agreement with previous findings (- 85.4 δ/ppm for H_α, - 40.58 δ/ppm H_β)[47] and such shifts in solution were not effected by further addition (excess) of [TBA]Br, as it occurs in **2** and **3**. The UV/vis/nIR absorption spectrum (MeOH) of $[Pc_2Tb]^-[TBA]^+$ is shown in

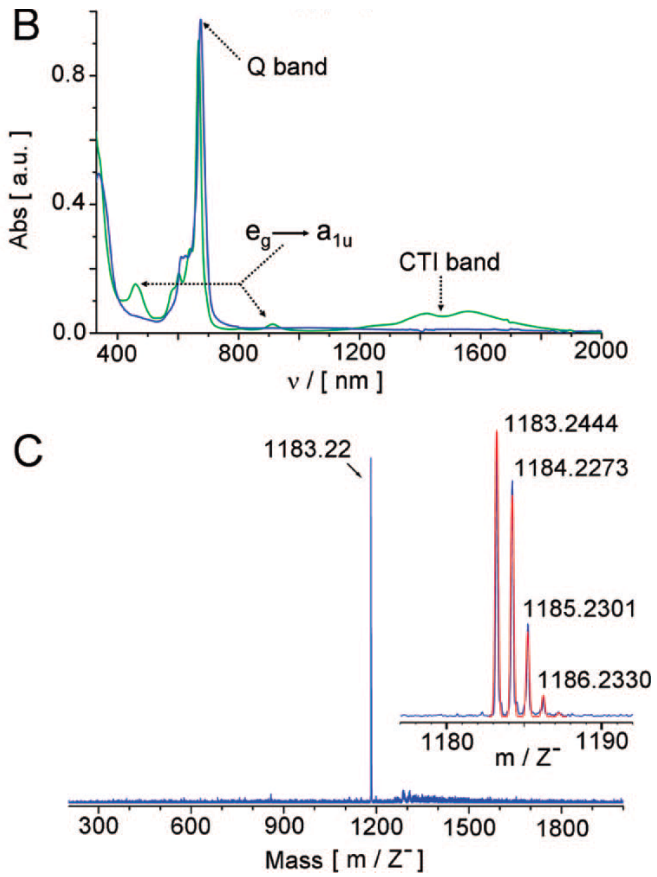

Figure 8.2: (B) UV/vis/nIR (MeOH) of $[Pc_2Tb]^-[TBA]^+$ (**1**) (blue line). The neutral form $[Pc_2Tb]^0$ (green line) is shown for comparison. (C) Maldi-ToF mass spectrum of $[Pc_2Tb]^-[TBA]^+$ (**1**) with the molecular peak of $[Pc_2Tb]^-$ (m/z^-) 1183.22, 100 %, M^-) recorded in the negative polarity mode. The small inset shows the high-resolution Maldi-ToF peak of $[Pc_2Tb]^-$ evidencing the isotopic distribution pattern (blue line) together with its simulation (red line).

Fig. (8.2-B). It exhibits Soret (336 nm) and Q-bands (674 nm) at the expected positions (see Par. 2.2), while the $e_g \longrightarrow a_{1u}$ transitions (460 and 910 nm) and the CTI transitions (charge transfer intervalence band, above 1400 nm) are clearly missing. Those signals (CTI and $e_g \rightarrow a_{1u}$) are known to represent fingerprints of the neutral specie $[Pc_2Tb]^0$, and thus confirm the absence of contamination derived from the neutral $[Pc_2Tb]^0$ form in the $[Pc_2Tb]^-[TBA]^+$ compound[34]. The Maldi-ToF mass spectrum of $[Pc_2Tb]^-[TBA]^+$ (**1**) (Fig. 8.2-C) showed clearly the molecular peak for $[Pc_2Tb]^-$ ($m/z^- = 1183.22$, 100 %, M^-) only when negative polarity mode was applied within the acquisition procedure, while the cationic part $[TBA]^+$ ($m/z^+ = 241.87$, 100 %, M^+) could be detected only in positive polarity, as indication of their respective charges.

8.1.3 Single Crystal X-ray Analysis of $[Pc_2Tb]^-[TBA]^+\times$ 3 $[TBA]^+Br^-\times$ 3 H_2O (4)

Starting from the diluted $[Pc_2Tb]^-[TBA]^+ \times 9$ [TBA]Br sample, the molecular complex **4** crystallized in MeOH, forming blue-violet needles, within few days. In fact, the single-crystal analysis resulted in the composition $[Pc_2Tb]^-[TBA]^+ \times 3$ [TBA]Br $\times 3$ H_2O with the compound crystallizing in the monoclinic space group $P2_1/c$ and four formula units in the unit cell (Fig. 2.1-A). Note that not all excess [TBA]Br molecules were trapped in the crystalline material. The TBAs cation and the $[Pc_2Tb]^-$ anion alternate in stacks along the b-axis. Here, the trough-space metal-to-metal distance is considerably large, d(Tb-Tb)= 22.95-23.24 Å. Along the c-axis, zigzag chains evolve with closer and alternating distances among neighboring Tb^3+ ions (13.08 Å and 12.35 Å). Such arrangement gives short -CH$\cdots$HC- contacts, potentially magnetic, between neighboring Pc molecules (C$\cdots$C contacts between 2.829 Å and 2.774 Å). Because the $[TBA]^+$, Br^-, and solvent molecules preferentially locate themselves in alternate stacks with respect to $[Pc_2Tb]^-$, as also observed in the other crystal structure known for this compound (*Vide infra*)[75]. The addition of large excess of [TBA]Br should destabilize in the powder such -CH$\cdots$HC- contacts witnessed along the crystallographic c-axis hindering the possible magnetic interaction between $[Pc_2Tb]^-$ neighboring molecules by increasing furthermore their segregation inside the matrix. The terbium (III) metal ion, as shown in Fig. (2.1-B), is coordinated by eight phthalocyanine nitrogens with an averaged Tb-N distance of 2.443 Å and adopts a square distorted antiprism as for the coordination polyhedron. The metal-ion displacement from the plane defined by the coordinating isoindole nitrogens N1A-N3A-N5A-N7A is 1.408 Å, and from the other plane defined by N1B-N3B-N5B-N7B is 1.420 Å. The resulting inter-plane distance of 2.828 Å between Pc rings is practically identical to the distance found for the compound $[Pc_2Tb]^-[TBA]^+ \times CH_3OH \times 3/2$ H_2O that exhibits, however, a different composition, crystal system, and also space group (orthorhombic, $Pna2_1$)[75].

8.2 Microcalorimeter for Specific Heat Measurements

The microcalorimeter consists of a small sapphire chip on which a serpentine metallic heater is evaporated. Attached to the chip with 50 μm gold leads is a Cernox temperature sensor Fig. (8.3). The chip is suspended inside the calorimeter copper cell by 20 μm tungsten leads which make electrical connections to the elements and also provide a weak thermal link to the cell. For a given cell temperature, the chip temperature is a function only of the power dissipated in the heater element. Because the thermal link is so weak, small power adjustments cause large temperature changes. Sapphire is an ideal material because it has a very small heat capacity at low temperatures and is an

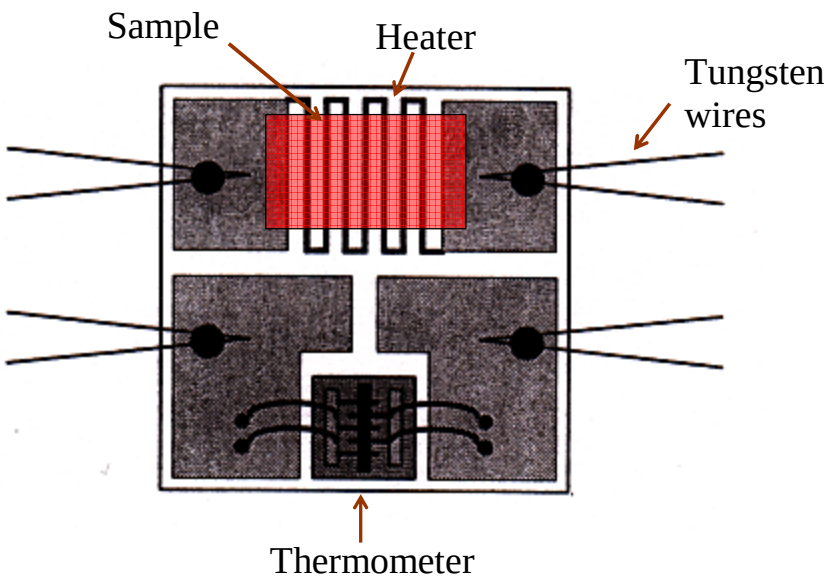

Figure 8.3: Schematic representation of the sapphire chip and the Cernox thermometer.

excellent thermal conductor while being an electrical insulator. The Cernox thermometer is extremely small and adds very little to the addenda. The relatively thick and short gold leads, together with the small size of the Cernox mean that its thermal response is extremely rapid compared with that of the chip relative to the cryostat. Thus the assembly as a whole can be treated as a single thermal unit which will simply be referred as the chip. The tungsten wires will also make a small contribution to the measured heat capacity, but this contribution is found to be effectively independent of the cryostat temperature. The addenda heat capacity is thus a function of chip temperature only. The back surface of the chip can be used for the sample mounting. If the sample is in close contact with the chip, then the measured heat capacity will be that of the chip plus that of the sample. However, since the sample to be measured was a powder, it was wrapped up in a small piece of an aluminum foil, and then bonded to the chip by using a thermally conductive grease. Before measuring the sample, a preliminary measurement of the addenda specific heat was performed and then it was subtracted from the total specific heat. The calorimeter cell in turn was screwed onto the cold stage of a VT insert, with thermally conductive grease used at the interface. The temperature of the end of the leads was thus considered identical to that of the cryostat itself.

8.3 Apparatus for Magnetization Measurements under Pressure

Dc magnetization measurements under pressure were performed by using an easyLab Mcell 10 module, formed by a Mcell 10 pressure cell and a Mpress Mk2 mechanical press. The system allows to perform DC magnetization measurements under high pressure up to 10 kbar. The main components of the pressure cell are the pressure cell body, the lower and upper locking nuts, the anti-extrusion disks, the PTFE cap and the PTFE plug, the ceramics pistons and the ceramics pistons caps (Fig. 8.4). A mounting platform is also supplied in order to facilitate the set-up of the pressure cell (Fig. 8.5). The setting up of the pressure cell is briefly the following. A ceramic piston cap is screwed into position in the bottom of the cell body channel using the lower locking nut. Then, the lower part of the cell is sat in the 8.5 mm hole of the mounting platform and a ceramic piston and an anti-extrusion disk are slid down into the cell's pressure channel. After having sat one PTFE cap in the smaller

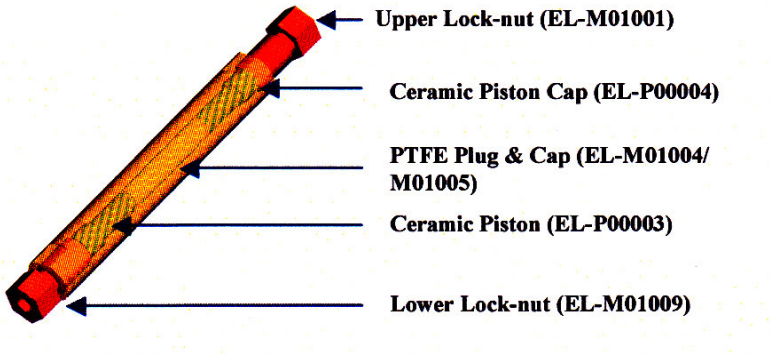

Figure 8.4: 3D modelling of the easyLab Mcell 10.

Figure 8.5: Mcell components and mounting platform.

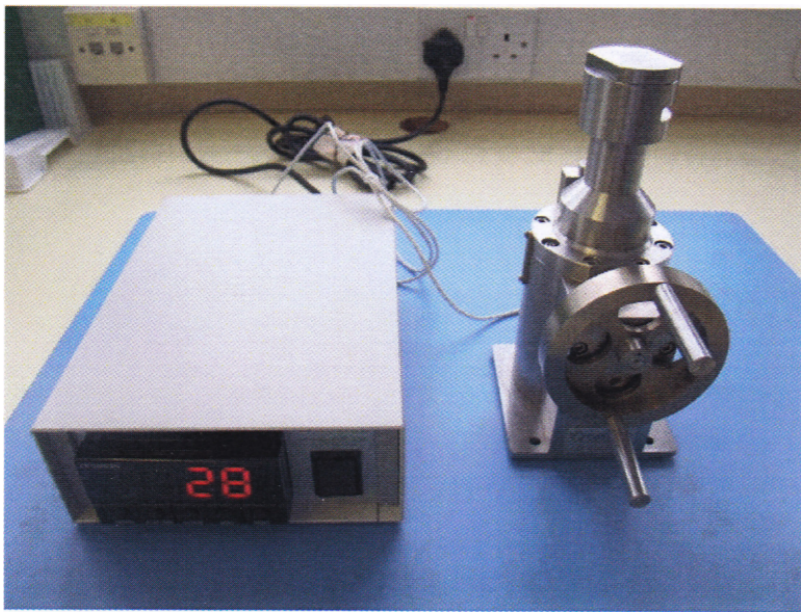

Figure 8.6: Picture of the main components of the Mpress Mk2. The force reader (left) and the press (right).

hole of the mounting platform, the sample can be loaded and the transmitting medium injected into the PTFE cap using a syringe. It is very important to avoid trapped air bubbles inside the cap at this stage. The PTFE cap is closed using a PTFE plug, than the capsule is slid inside the cell's channel with the plug facing towards the top of the cell. An anti-extrusion disk is placed on the top of the PTFE capsule, followed by the second ceramic piston and the ceramic piston cap. The cell is than closed by screwing the upper locknut in place by hand. The Mpress Mk2 is a purely mechanical press capable of generating forces up to $15{\cdot}10^3$ N and is composed of a force reader and a press (Fig. 8.6). The cell must be inserted properly in the bottom of the press. A piston is then inserted through the lower nut and the press closed with the closing lid. The applied force can be increased using the handle of the press. When the target force has been achieved, the lower nut is tightened with a steel spanner through the lateral window of the press. Finally the force on the press can be released, the cell extracted from the press and mounted on MPMS sample rod.

Bibliography

[1] E. Coronado and P. Day, *Chem. Rev.* **104** 5419 (2004).

[2] S. A. Wolf, D. D. Awschalom, R. A. Buhrman, J. M. Daughton, S. von Molnár, M. L. Roukes, A. Y. Chtchelkanova and D. M. Treger, *Science* **294** 1488 (2001).

[3] N. J. Tao, *Nature Nanotech* **1** 173 (2006).

[4] D. Gatteschi, O. Kahn, J. S. Miller and F. Palacio, Eds. *Magnetic Molecular Materials*; NATO ASI Series 198; Kluwer Academic Publishers: Dordrech, (1991).

[5] O. Kahn, *Molecular Magnetism*; Wiley-VCH Inc.: New York, (1993).

[6] J. S. Miller and M. Drillon, Eds. *Magnetism: Molecules to Materials*; Wiley-VCH Verlag.: Weinheim; Vol. I (2001), Vol.II (2001), Vol. III (2002), Vol. IV (2003). Vol. V (2005).

[7] L. Thomas, F. Lionti, R. Ballou, D. Gatteschi, R. Sessoli and B. Barbara *Nature* **383** 145 (1996).

[8] D. Gatteschi and R. Sessoli *Angew. Chem., Int. Ed.* **42** 268 (2003).

[9] J. R. Friedman, M. P. Sarachick, J. Tejada and R. Ziolo *Phys. Rev. Lett.* **76** 3830 (1996).

[10] W. Wernsdorfer and R. Sessoli *Scienze* **284** 133 (1999).

[11] G. Christou, D. Gatteschi, D. N. Hendrichson and R. Sessoli *MRS bull.* **25** 66 (2000).

[12] G. Aromi, S. M. J. Aubin, M. A. Bolcar, G. Christou, H. J. Eppley, K. Folfting, D. N. Hendrickson, J. Huffman, R. C. Squire, H. L. Tsai, S. Wang and M. W. Wemple, *Polyhedron* **17** 3005 (1998).

[13] T. Lis, *Acta Crystallogr.* **B36** 2042 (1980).

[14] R. Sessoli, D. Gatteschi, A. Caneschi and M. A. Novak, *Nature* **365** 141 (1993).

[15] C. Boskovic, M. Pink, J. C. Huffman, D. N. Hendrichson, G. Christou, *J. Am. Chem. Soc.* **123** 9914 (2001).

[16] M. Soler, W. Wernsdorfer, K. Folfting, M. Pink and G. Christou, *J. Am. Chem. Soc.* **126** 2156 (2004).

[17] C. Sangregorio, T. Ohm, C. Paulsen, R. Sessoli and D. Gatteschi *Phys. Rev. Lett.* **78** 4645 (1997).

[18] (a) S. M. J. Aubin, N. R. Dilley, L. Pardi, J. Krzystek, M. W. Wemple, L. C. Brunel, M. B. Maple, G. Christou and D. N. Hendrichson *J. Am. Chem. Soc.* **120** 4991 (1998). (b) S. M. J. Aubin, N. R. Dilley, M. W. Wemple, M. B. Maple, G. Christou and D. N. Hendrichson *J. Am. Chem. Soc.* **120** 839 (1998).

[19] H. Andres, R. Blaser, H. U. Gudel, G. Aromi, G. Christou, H. Buttner and B. Ruffle *J. Am. Chem. Soc.* **122** 12469 (2000).

[20] (a) E. J. Schelter, F. Karadas, C. Avendano, A. V. Prosvirin, W. Wernsdorfer and K. R. J. Dunbar *J. Am. Chem. Soc.* **129** 8139 (2007). (b) A. Muller, F. Peters, M. T. Pope and D. Gatteschi, *Chem. Rev.* **98** 239 (1998).

[21] D. Gatteschi, R. Sessoli and J. Villain, *Molecular Nanomagnets* Oxford University Press; New York (2006).

[22] W. Wernsdorfer, N. Aliaga-Alcade, D. N. Hendrichson and G. Christou *Nature* **416** 406 (2002).

[23] R. Tiron, W. Wernsdorfer, D. Foguet-Albiol, N. Aliaga-Alcade and G. Christou *Phys. Rev. Lett.* **91** 227203 (2003).

[24] L. Bogani and W. Wernsdorfer, *Nat. Mater.* **7** 179 (2008).

[25] D. P. DiVincenzo, *Science* **270** 255 (1995).

[26] (a) M. Leuenberg and D. Loss, *Nature* **410** 789 (2001). (b) M. Affronte, F. Troiani, A. Ghirri, A. Ghirri, A. Candini, M. Evangelisti, V. Corradini, P. Santini, G. Amoretti, G. Tuna and R. E. P. Winpenny *J. Phys. D: Appl. Phys.* **40** 2999 (2007). (c) W. Wernsdorfer, *Nat. Mater.* **6** 174 (2007).

[27] R. Sessoli and A. Cornia, *Chem. Commun.* 725 (2000).

[28] G. Aromi, J. P. Claude, M. J. Knapp, J. Huffman, D. N. Hendrickson and G. Christou, *J. Am. Chem. Soc.* **120** 2977 (1998).

[29] C. J. Milios, A. Vinslava, W. Wernsdorfer, S. Moggach, S. Parsons, S. P. Perlepes, G. Christou and E. K. J Brechin *J. Am. Chem. Soc.* **129** 2754 (2007).

[30] N. E. Chakov, S. C. Lee, A. G. Harter, P. L. Kuhns, A. P. Reyes, S. O. Hill, N. S. Dalal, W. Wernsdorfer, K. Abboud and G. Christou, *J. Am. Chem. Soc.* **128** 6975 (2006).

[31] N. Ishikawa, M. Sugita, T. Ishikawa, S. Koshihara and Y. Kaizu, *J. Am. Chem. Soc.* **125** 8694 (2003).

[32] N. Ishikawa, M. Sugita, T. Ishikawa, S. Koshihara and Y. Kaizu, *J. Phys. Chem. B* **108** 11265 (2004).

[33] N. Ishikawa, M. Sugita and W. Wernsdorfer *J. Am. Chem. Soc.* **127** 3650 (2005).

[34] (a) I. S. Kirinp, P. N. Moskalev and Y. A. Makashev *Russ. J. Inorg. Chem.* **10** 1065 (1965). (b) I. S. Kirinp, P. N. Moskalev and Y. A. Makashev *Russ J. Inorg. Chem.* **12** 369 (1967). (c) I. S. Kirinp, Y. L. Shelekhi and P. N. Moskalev *Sov. Phys. Solid State (Engl. Transl.)* **9** 1461 (1967).

[35] A. Decian, M. Moussavi, J. Fischer and R. Weiss, *Inorg. Chem.* **24**, 3162 (1985).

[36] K. L. Trojan, W. E. Hatfield, K. D. Kepler and M. L. J. Kirk, *J. Appl. Phys.* **69**, 6007 (1991).

[37] K. L. Trojan, J. L. Kendall, K. D. Kepler and W. E. Hatfield, *Inorg. Chem. Acta* **198**, 795 (1992).

[38] (a) R. Giraud, W. Wernsdorfer, A. Tkachuk, D. Mailly and B. Barbara *Phys. Rev. Lett.* **87** 057203 (2001). (b) R. Giraud, A. Tkachuk, D. Mailly and B. Barbara *Phys. Rev. Lett.* **91** 257204 (2003).

[39] M. J. Graf, A. Lascialfari, F. Borsa, A. M. Tkachuk and B. Barbara *Phys. Rev. B* **73** 024403 (2006).

[40] P. E. Hansen, T. Johansson and R. Nevald, *Phys. Rev. B* **12** 5315 (1975).

[41] D. H. Reich, B. Ellman, J. Yang, T. F. Rosenbaum, G. Aeppli and D. P. Belanger, *Phys. Rev. B* **42** 4631 (1990).

[42] W. Wu, B. Ellman, T. F. Rosenbaum, G. Aeppli, and D. H. Reich, *Phys. Rev. Lett.* **67** 2076 (1991).

[43] S. Ghosh, R. Parthasarathay, T. F. Rosenbaum and G. Aeppli, *Science* **296** 2195 (2002).

[44] G. Mennenga, L. J. de Jongh and W. J. Huiskamp, *J. Magn. Magn. Mater.* **44** 59 (1984).

[45] N. Ishikawa, M. Sugita and W. Wernsdorfer *Angew. Chem. Int. Ed.* **44** 2931 (2005).

[46] N. Ishikawa, *Polyhedron* **26** 2147 (2005).

[47] N. Ishikawa, M. Sugita, T. Okubo, N. Tanaka, I. Tomochika and Y. Kaizu, *Inorg. Chem.* **42** 2440 (2003).

[48] F. Branzoli, P. Carretta, M. Filibian, G. Zoppellaro, M. J. Graf, J. R. Galan-Mascaros, O. Fuhr, S. Brink and M. Ruben, *J. Am. Chem. Soc.* **131** 4387 (2009).

[49] N. Ishikawa, M. Sugita, N. Tanaka, T. Ishikawa, S. Koshihara and Y. Kaizu, *Inorg. Chem.* **43** 5498 (2004).

[50] S. Takamatsu, T. Ishikawa, S. Koshihara and N. Ishikawa, *Inorg. Chem.* **46** 7250 (2007).

[51] N. Ishikawa, Y. Mizuno, S. Takamatsu, T. Ishikawa and S. Koshihara, *Inorg. Chem.* **47** 10217 (2008).

[52] L. Vitali, S. Fabris, A. Mosca Conte, S. Brink, M. Ruben, S. Baroni and K. Kern, *Nano Lett.* **8** 3364 (2008).

[53] E. Osorio, T. Bjornholm, J. M. Lehn, M. Ruben and H. S. J. van der Zant, *Phys. Condens. Matter.* **20** 374121 (2008).

[54] M. Ruben, A. Landa, E. Lortscher, H. Riel, M. Mayor, H. Gorls, H. B. Weber, A. Arnold and V. Evers, *Small* **12** 2229 (2008).

[55] G. H. Kim and T. S. Kim, *Phys. Rev. Lett.* **92** 137203 (2004).

[56] P. Wahl, P. Simon, L. Diekhöner, V. S. Stepanyuk, P. Bruno, M. A. Schneider, K. Kern and T. S. Kim, *Phys. Rev. Lett.* **98** 056601 (2007).

[57] H. Park, A. K. L. Kim, A. P. Alivisatos, J. Park and P. L. McEuen, *Appl. Phys. Rev.* **75** 301 (1999).

[58] S. Sanvito and A. R. Rocha, *J. Comput. Theor. Nanosc.* **3** 624 (2006).

[59] A. N. Pasupathy *et al.*, *Scienze* **306** 86 (2004).

[60] L. E. Hueso, J. M. Pruneda, V. Ferrari, G. Burnelli, J. P. Valde´s-Herrera, B. D. Simons, P. B. Littlewood, E. Artacho, A. Fert and N. D. Mathur, *Nature* **445** 410 (2007).

[61] C. Timm and F. Elste, *Phys. Rev. B* **73** 235304 (2006).

[62] S. Kyatskaya,J. R. Galán Mascarós, L. Bogani, F. Hennrich, M. Kappes, W. Wernsdorfer and M. Ruben, *J. Am. Chem. Soc.* **131** 15143 (2009).

[63] E. Coronado and J. R. Galán Mascarós, *J. Mater. Chem.* **15** 66 (2005).

[64] J. M. Williams, J. R. Ferraro, R. J. Thorn, K. D. Carlson, U. Geiser, H. H. Wang, A. M. Kini and M. H. Whangbo, in *Organic Superconductors (Including Fullerenes): Synthesis, Structure, Properties and Theory*, R. N. Grimes, ed., Prentice-Hall Englewoods Cliffs, NJ (1992).

[65] E. Coronado, L. R. Falvello, J. R. Galán Mascarós, C. Gimenez-Saiz, C. J. Gómez-García, V. N. Laukhin, A. Perez-Benitez, C. Rovira and J. Veciana *Adv. Mater* **9** 984 (1997).

[66] H. Kobayashi, H. Tomita, T. Naito, A. Kobayashi, F. Sakai, T. Watanabe and P. Cassoux, *J. Am. Chem. Soc.* **118** 368 (1996).

[67] O. Cepas, R. H. McKenzie and J. Merino, *Phys. Rev. B*, **65** 502 (2002).

[68] E. Coronado, J. R. Galán-Mascarós, C. J. Gómez-García and V. Laukhin, *Nature* **408** 447 (2000).

[69] M. Clemente-Leon, E. Coronado, P. Delhaes, C. J. Gomez-Garcia and C. Mingotaud, *Adv. Mater* **13** 574 (2001).

[70] B. Cage, S. E. Russek, R. Shoemaker, A. J. Barker, C. Stoldt, V. Ramachandaran and N. S. Dalal, *Polyhedron* **26** 2413 (2007).

[71] R. B. Clarkson, *Top. Curr. Chem.* **221** 202 (2002).

[72] R. M. Henkelman, G. J. Stanisz and S. J. Graham, *NMR Biomed.* **14** 57 (2001).

[73] S. Viswanathan, Z. Kovacs, K. N. Green, S. J. Ratnakar and A. D. Sherry, *Chem. Rev.* **110** 2960 (2010).

[74] M. Moussavi, A. De Cian, J. Fischer and R. Weiss, *Inorg. Chem.* **27** 1287 (1988).

[75] C. Loosli, S.-X. Liu, A. Neels, G. Labat and S. Z. Decurtins, *Kristallogr.* **221** 135 (2006).

[76] C. Harnoode, K. Takamura, H. Kubota, K. Sho, K. Fujisawa, F. Kitamura, T. Ohsaka and K. Tokuda, *Electrochemistry* **67** 832 (1999).

[77] N. Koike, H. Uekusa, Y. Ohashi, C. Harnoode, F. Kitamura, T. Ohsaka and K. Tokuda, *ibid.* **35**, 5798 (1996)

[78] K. Kasuga, M. Tsutsui, R. C. Petterson, K. Tatsumi, N. Van Opdenbosch, G. Pepe and E. F. Meyer, *J. Am. Chem. Soc.* **102**, 4835 (1980).

[79] K. Katoh, Y. Yoshida, M. Yamashita, H. Miyasaka, B. K. Breedlove, T. Kajiwara, S. Takaishi, N. Ishikawa, H. Isshiki, Y. F. Zhang, T. Komeda, M. Yamagishi and J. Takeya, *J. Am. Chem. Soc.* **131** 9967 (2009).

[80] (a) N. Ishikawa, O. Ohno, Y. Kaizu and H. Kobayashi, *J. Phys. Chem.* **96** 8832 (1992); (b) N. Ishikawa, O. Ohno and Y. Kaizu, *J. Phys. Chem.* **97** 1004 (1993); (c) N. Ishikawa and Y. Kaizu, *J. Porphyr. Phthalocya.* **3** 514 (1999); (d) N. Ishikawa, *J. Porphyr. Phthalocya.* **5** 87 (2001).

[81] R. Rousseau, R. Aroca and M.L. Rodriguez-Mendez *J. Molec. Struct.*, **356** 49 (1995).

[82] S. Takamatsu and T. Ishikawa, *Polyhedron* **26** 1859 (2007).

[83] E. Orti, J.L. Bredas and C. Clarisse, *J. Chem. Phys.*, **92** 1228 (1990).

[84] H. Meier, *Organic Semiconductors*, Verlag Chemie: Berlin (1974).

[85] J. Simon, J. J. Andre and A. Skoulios, *Nouv. J. Chim.* **10** 295 (1986).

[86] G. C. S. Collins and D. J. Schiffrin, *J. Electroanal. Chem.* **139** 335 (1982).

[87] J. Simon, F. Tournilhac and J. Andrè, *Nouv. J. Chim.* **11** 383 (1987).

[88] P. Turek, P. Petit, J.-J. Andrè,J. Simon, R. Even, B. Boudjema, G. Guillaud and M. Maitrot, *J. Am. Chem. Soc.* **109** 5122 (1987).

[89] G. Guillaud, J. Simon and J. P. Germain, *Coord. Chem. Rev.* **178-180** 1433 (1998).

[90] M. Filibian, P. Carretta, M. C. Mozzati, P. Ghigna, G. Zoppellaro and M. Ruben, *Phys. Rev. Lett.* **100** 117601 (2008).

[91] (a) J. Gomez-Segura, I. Diez-Perez, N. Ishikawa, M. Nakano, J. Veciana and D. Ruiz-Molina, *Chem. Commun.* 2866 (2006); (b) T. Ye, T. Takami, R. Wang, J. Jiang and P. S. Weiss, *J. Am. Chem. Soc.* **128** 10984 (2006).

[92] C. Ehli, G. M. Aminur Rahman, N. Jux, D. Balbinot, D. M. Guldi, F. Paolucci, M. Marcaccio, D. Paolucci, M. Melle-Franco, F. Zerbetto, S. Campidelli and M. Prato, *J. Am. Chem. Soc.* **128** 11222 (2006).

[93] N. Ishikawa, I. Tomochika and Y. Kaizu, *J. Phys. Chem.* **106** 9543 (2002).

[94] A. Abragam and B. Bleaney, *Electron Paramagnetic Resonance*, Clarendon Press: Oxford (1970).

[95] K. W. H. Stevens, *Proc. Phys. Soc., London, Sect. A* **65** 209 (1952).

[96] C. P. Poole, H. A. Farach, *Handbook of Electron Spin Resonance*; AIP Press: New York (1993).

[97] W. Heitler and E. Teller, *Proc. Roy. Soc. A* **155** 629 (1936).

[98] M. Fierz, *Physica* **5** 433 (1938).

[99] R. de L. Kronig, *Physica* **6** 33 (1939).

[100] (a) J. H. Van Vleck, *J. Chem. Phys.* **7** 72 (1939); (b) J. H. Van Vleck, *Phys. Rev.* **57** 426 (1940); (c) J. H. Van Vleck, *Phys. Rev.* **59** 724 (1941); (d) J. H. Van Vleck, *Phys. Rev.* **59** 730 (1941).

[101] (a) C. B. P. Finn, R. Orbach and W. P. Wolf, *Proc. Phys. Soc.* **77** 261 (1961); (b) A. H. Cooke, C. B. P. Finn and R. Orbach, *Bull. Ampere* **9** 111 (1961); (c) R. Orbach, *Proc. R. Soc. London, Ser. A* **264** 458 (1961).

[102] J. Jiang, K. Kasuga and D.P. Arnold, in: H.S. Nalwa (Ed.), *Supramolecular Photo-sensitive and Electroactive Materials*, Academic Press, New York (2001), p. 113 (Chapter 2).

[103] L.A. Lapkina, Y. Gorbunova, S.E. Nefedov and A.V. Tsivadze, *Russ. Chem. Bull.* **52** 1 (2003).

[104] W. Su, M. Bao and J. Jiang, *Vib. Spectrosc.* **39** 186 (2005).

[105] X. Sun, L. Rintoul, Y. Bian, D.P. Arnold, R. Wang and J. Jiang, *J. Raman Spectrosc.* **34** 306 (2003).

[106] J. Jiang, U. Cornelisson, D.P. Arnold, X. Sun and H. Homborg, *Polyhedron* **20** 557 (2001).

[107] N. W. Ashccroft and N. D. Mermin *Solid State Physics* Thomson Learning Inc., Cornell University (1976).

[108] M. Affronte, J.C. Lasjaunias, A. Cornia and A. Caneschi, *Phys. Rev. B* **60** 1161 (1999).

[109] H. Yang, J. C. Lasjaunias and P. Monceau, *Journal of Physics: Condensed Matter* **11** 5083 (1999).

[110] S. Sachdev and K. Damle *Phys. Rev. Lett.* **78** 943 (1997).

[111] (a) G. Soda, D. Jerome, M. Weger, J. Alizon, J. Gallice, H. Robert, J.M. Fabre and L. Giral, *J. Phys. France* **38** 931 (1977); (b) L. J. Azevedo, J. E. Schirber and J. C. Scott, *Phys. Rev. Lett.* **48** 826 (1982)

[112] G. Grosso and G. Pastori Parravicini, *Solid State Physics*, Cambridge University Press (Academic Press), Cambridge (2000).

[113] J. L. Paillaud, M. Drillon, A. De Cian, J. Fisher, R. Weiss and G. Villeneuve *Phys. Rev. Lett.* **67** 244 (1991).

[114] M. Drillon and R. Georges *Phys. Rev. B* **24** 1278 (1981).

[115] A. Schenck, *Muon Spin Rotation: Principles and Applications in Solid State Physics* Hilger, Bristol (1986).

[116] A. Lascialfari, Z. H. Jang, F. Borsa, P. Carretta and D. Gatteschi, *Phys. Rev. Lett.* **81** 3773 (1998).

[117] C. Kittel, *Introduzione alla fisica dello stato solido*, John Wiley et Sons, New York, P.509 (1966).

[118] C. P Slichter, *Principles of Magnetic Resonance*, Springer-Verlag Berlin Heidelberg (1978).

[119] A. Abragam *Principles of Nuclear Magnetism*, Clarendon Press: Oxford (1961).

[120] F.Bloch, *Phys. Rev.* **70** 460 (1946).

[121] T. Moriya, *Prog. Theor. Phys.* **16** 23 (1956).

[122] A. Rigamonti, P. Carretta, *Studi NMR-NQR di superconduttori ad alta T_c e di antiferromagneti loro precursori*, Istituto Lombardo XXIX 183-310, (**1994**).

[123] A. Rigamonti, F. Borsa and P. Carretta, *Rep. Prog. Phys.* **61**, 1367 (1998).

[124] R. L. Garwin, L. M. Lederman and M. Weinrich, *Phys. Rev.* **105** 1415 (1957).

[125] S.J.Blundell, *Contemporary Physics* **40**, 175, (1999).

[126] Hayano *et al.*, *Phys. Rev. B* **20** 850 (1979).

[127] R. Kubo and T. Toyabe in *Magnetic Resonance and Relaxation*, ed. Blinc, R., North-Holland, Amsterdam (1967).

[128] F. Tedoldi, A. Campana and P.Carretta, *Eur. Phys. J. B* **19** 319 (2001).

[129] P. Petit and P. Spegt *J. Phys. France* **51** 1645 (1990).

[130] H. J Shultz, *Phys. Rev. B* **34** 6372 (1986).

[131] M. Takigawa, O. A. Starykh, A. W. Sandvik and R. R. P. Singh, *Phys. Rev. B* **56** 13 681 (1997).

[132] S. Sachdev, *Phys. Rev. B* **50** 13 006 (1994).

[133] F. Devreux, J. P. Boucher and M. Nechtschein *J. Phys. France* **35** 271 (1974).

List of publications

1. F. Branzoli, P. Carretta, M. Filibian, G. Zoppellaro, M. J. Graf, J. R. Gálan-Mascarós , O. Fhur, S. Brink and M. Ruben, *J. Am. Chem. Soc.* **131** 4387 (2009).

2. F. Branzoli, M. Filibian, P. Carretta, S. Klyatskaya and M. Ruben, *Phys. Rev. B* **79** 220404 (2009).

3. F. Branzoli, P. Carretta, M. Filibian, M. J. Graf, S. Klyatskaya, M. Ruben, F. Coneri and P. Dhakal, *Phys. Rev. B* **79** 134401 (2010).

4. F. Branzoli, P. Carretta, M. Filibian, S. Klyatskaya and M. Ruben, submitted to *Phys. Rev. B*.

Acknowledgements

I would like to thank Prof. Pietro Carretta and Dr. Marta Filibian for their teachings and suggestions which have accompanied me throughout these years of research at University of Pavia. I also thank very much Prof. Michael J. Graf, Prof. Alessandro Lascialfari and Prof. Maurizio Corti for all the help and useful discussions, Dr. Mario Ruben and Dr. Svetlana Klyatskaya for the important collaboration, Sergio Aldrovandi and Marco Moscardini for the technical assistance and Prof. Amit Keren for having accepted to be the referee of this thesis. Special thanks to my colleagues and friends Ettore Bernardi, Lorenzo Bordonali, Susanna Costanza, Michele Dall' Arno, Marco Grandi, Manuel Mariani, Andrea Negri, Nico Papinutto, Giacomo Prando and Samuele Sanna.